AEROELASTIC MECHANICS OF THIN FILM MEMBRANES IN PROXIMITY LITHOGRAPHY

A Thesis Presented
by
Dylan Burns
to
The Faculty of the Graduate College
of
The University of Vermont

In Partial Fulfillment of the Requirements for the Degree of Master Science Specializing in Mechanical Engineering

February 2006

Accepted by the Faculty of the Graduate College, The University of Vermont, in partial fulfillment of the requirements for the degree of Master of Science, Specializing in Mechanical Engineering.

Thesis Examination Committee:

_____ Advisor
Dr. Huston, PhD

_____
Dr. Beliveau, PhD

_____ Chairperson
Dr. Varhue, PhD

_____
Frances E, Carr, PhD

Date: December 15, 2005

Abstract

This research addresses the aeroelastic mechanics of thin film membrane masks during proximity (X-ray) lithography. This ultra-high precision manufacturing process uses an X-ray source to expose resist on silicon substrates in patterns carried by a thin membrane mask that is held near to the substrate. The mask is positioned relative to the substrate wafer with a stepper tool. Positioning and alignment maneuvers cause aerodynamic loads that may give rise to unwanted deformations in the mask. The deformations in the mask feedback to alter the aerodynamic loads to produce aeroelastic effects.

Testing was done both experimentally and theoretically. The experimental testing was performed using a custom built aeroelasticity test rig, which allowed for various means of positioning and moving of the mask relative to a fixed flat surface in a manner that mimics many of the positioning maneuvers used in a production stepper. These tests were also simulated in FEMLAB using a theoretical model based on principles of hydrodynamic lubrication coupled with membrane mechanics. The models predicted the aeroelastic behavior of the thin film membranes for various gaps, wedge angles, and velocities. The experimental results agree favorably with the numerical models in both qualitative and quantitative aspects.

These situations simulated the stepping process that occurs during the during proximity (X-ray) lithography. In the application of proximity lithography, it would be greatly beneficial to be able to model these experiments in FEMLAB first before actually performing them. This would allow for the ideal settings to be determined for the manufacturing process, so as to optimize production rates by stepping at gap, and to examine the efficacy of aeroelastic control devices and mesa mask geometries.

Acknowledgements

I would like to thank Dr. Huston for all of his help and support, not only with my thesis but through out all of my years here at UVM. His knowledge and guidance has been an enormous benefit for me both academically and with life in general. I would also like to thank JMAR Systems inc. for their support on this project through Navair contract #N00421-02-D-3189. I would like to thank Dr. Varhue and Dr. Beliveau for being on my committee.

Table of Contents

Acknowledgements ii

List of Tables vi

List of Figures vii

CHAPTER 1: INTRODUCTION 1

CHAPTER 2: AEROELASTICITY SYSTEM 6

2.1 Background 6

2.2 Aeroelastic Mechanics 7

2.3 Theoretical Model 10

CHAPTER 3: NUMERICAL CALCULATION 13

3.1 FEMLAB 13

3.2 Modeling Equations 13

3.2.1 FEMLAB Model Verification Studies 14

3.2.2 Rectangular Geometry 14

3.2.3 Hand Calculations 14

3.2.4 FEMLAB Rectangle 17

3.2.3 Rectangular Tests / Results 21

3.2.4 Circular Geometry 25

3.2.5 Circular Tests / Results 27

CHAPTER 4: EXPERIMENTAL TEST BEDS 30

4.1 Rig Setup 30

4.2 Mylar Film 35
4.2.1 Procedure for Mylar Film 36
4.2.2 Tension Measurement Rig 40
4.3 Mask Positioning 42
4.4 Optical Displacement Measuring System 48
CHAPTER 5: EXPERIMENTS AND RESULTS 51
5.1 Bulge Tests 51
5.2 Typical Results 55
5.3 Tests 58
5.3.1 Velocity 58
5.3.2 Wedge Angle 59
5.3.3 Shape of Deflected Membrane 62
5.3.4 Gap 64
5.3.5 Infinitely Long 65
CHAPTER 6: DISCUSSION AND CONCLUSION 70
6.1 Conclusion 70
6.2 Limitations 72
6.3 Possible Future Research Directions 73
APPENDIX 74
A.1 74
A.2 Matlab Code 81
A.3 Excel Data 86
APPENDIX B 96

B.1 Tension Equation Derivation 96

B.2 Reynolds Number Calculation 102

B.3 Knudsen Number Calculation 104

B.4 MathCAD Calculations 107

REFERENCES 112

List of Tables

Table 1: Constants for infinitely long rectangle equations. 18

Table 2: Constants for position of the mask relative to the granite block 27

Table 3: Tension values for given pressure, and measured deflections..... 51

Table 4: Deflection and pressure calculations derived from FEMLAB 52

List of Figures

Figure 1: Exposure schematic 2

Figure 2: Cross section of a typical proximity lithography process 4

Figure 3: Mylar film stretched over ring..... 5

Figure 4: Geometry of gap closing maneuver..... 11

Figure 5: Geometry of a lateral stepping at gap with a converging wedge angle..... 12

Figure 6: Variables for the film in reference to the granite block. 16

Figure 7: FEMLAB 2-D solution for elongated rectangle..... 23

Figure 8: FEMLAB 3-D solution..... 24

Figure 9: FEMLAB model of the Mylar mask 26

Figure 10: Three-dimensional deflection graph for circular geometry membrane.... 29

Figure 11: Two-dimensional deflection graph for circular geometry..... 29

Figure 12: Top view of the aeroelasticity rig..... 31

Figure 13: Front and side views of aeroelasticity rig..... 32

Figure 14: Entire aeroelastisity rig setup 33

Figure 15: Silicon carbide mask mounted in silicon wafer..... 34

Figure 16: Mylar film, 2 microns thick..... 35

Figure 17: Setup of the optical displacement measurement sensor. 37

Figure 18: MATLAB GUI for calculating the wedge angle and mean gap..... 39

Figure 19: Pressure system setup..... 41

Figure 20: The optical displacement measurement sensor over the mylar film 42

Figure 21: Modified kinematic mount and dial indicators..... 43

Figure 22: Optical displacement measurement system..... 44

Figure 23: Translation positioning stage..... 45

Figure 24: Motion of granite Block 47

Figure 25: IR timing gates. 48

Figure 26: DATAQ DI-710 screw terminal access..... 49

Figure 27: Optical displacement measurement sensor perpendicular to Mylar film . 50

Figure 28: Pressure vs. deflection graph for experimental data..... 53

Figure 29: Pressure vs. deflection graph for FEMLAB data 54

Figure 30: Screen shot of computer taking measurements 55

Figure 31: Typical deflection vs. time graph for the Mylar film 57

Figure 32: Membrane deflection vs. velocity for constant wedge angle and gap..... 58

Figure 33: Time histories for deflection as the velocity. 60

Figure 34: Wedge angle vs. deflection 61

Figure 35: Position measurement across the membrane. 62

Figure 36: Deflection vs. position..... 63

Figure 37: Deflection vs. gap for a constant wedge angle..... 64

Figure 38: Geometry of elongated rectangle 65

Figure 39: Rectangular membrane, ten to one geometry. 66

Figure 40: Optical displacement sensor over the rectangle membrane. 68

Figure 41: Deflection vs. position data for the rectangular membrane..... 69

Figure 42: Deflection vs. velocity for FEMLAB, and experimental data. 71

Figure 43: Position vs. Velocity for FEMLAB, hand calculations and experimental data. 72

Chapter 1: Introduction

This thesis examines techniques to minimize aeroelastic effects on thin membrane window masks that move in close proximity to flat wafers. These membrane masks and wafers are used in X-ray and other proximity lithography technologies.

Rapidly attaining and maintaining precise mask to wafer positioning and alignment is essential to the technical and economic success of proximity lithography [19]. The dimensions and flexibility of these masks are such that they may be adversely affected by aerodynamic forces that arise during the positioning of the mask relative to a wafer. It is important to know how stepping maneuvers, both laterally and in closing the gap, will affect the mask. Critical gaps, velocities, wedge angles and specialized aerodynamic devices (such as through wafer perforations) that can be utilized without damaging the mask need to be determined. [22]

Perhaps the leading driver behind proximity lithography development is the continued development of x-ray lithography processes. The basic concept of proximity lithography appears in Figure 1.

Energy is transmitted through a window in the generator and is collected, collimated and directed through the mask onto the wafer. The membrane mask is typically made of silicon carbide, silicon nitride and diamond variants are occasionally used. Heavy metal absorbers are placed in the mask to carry the desired

image pattern. The mask is loaded into a stepper where wafers get aligned either field by field or globally for full field exposures. Each exposure requires advancing the wafer to a calculated gap based upon desired image results.

Recent advances in X-ray lithography have lead to the production of point-source stepper systems. JMAR has developed a system that uses a laser plasma to produce 1nm wavelength X-rays. These X-rays are called soft X-rays and have the appropriate transmission and absorption characteristics required for proximity X-ray lithography applications. This technology only has been developed to form the NanoPulsar™ II lithography system that is based on the Collimated Plasma Lithography (CPL™) technology. The laser plasma point source is designed to allow collimators to efficiently capture a large solid angle of spherically emitted X-rays, enabling fine line lithography with modest X-ray power levels. [32]

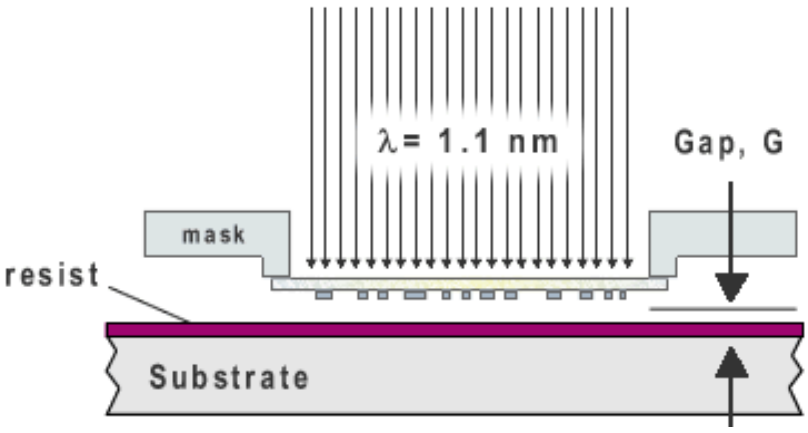

Figure 1: Exposure schematic (http://www.jmar.com/2004/prod_cpltech.shtml)

When the membrane mask is moving in close proximity to the wafer it causes the fluid in the gap (usually air or helium) to also move. As the mask moves the fluid in the gap can create a pressure on the membrane. This pressure depends on the speed of the wafer, the size on the gap, the wedge angle of the mask relative to the wafer and the fluid properties. The fluid pressure will cause the mask to deform, which affects the fluid pressure [2]. If the fluid in the gap behaves as a Newtonian fluid, then it is possible to use basic lubrication theory in the form of Reynolds equation to model the fluid mechanics.

The thesis addresses several of the main areas of membrane mask aeroelasticity. First is the development of a mechanical model of thin membrane aeroelastic mechanics. Next is a computer simulation of the aeroelastic mechanics. Then an experimental test rig that realistically simulates the aeroelastic phenomena in an exposure tool is designed, built and used. Finally, possible strategies for minimizing adverse aeroelastic effects are identified.

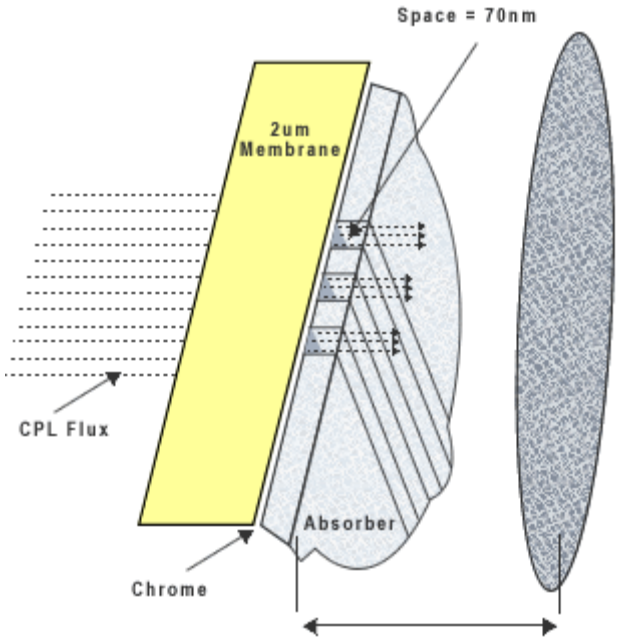

Figure 2: Cross section of a typical proximity lithography process (Collimated Plasma Lithography). (http://www.jmar.com/2004/prod_cpltech.shtml)

In order to simulate this process in the lab an aeroelasticity rig was built, using a stationary membrane and a moving granite block. In the experimental tests, a Mylar film membrane was used in place of a production-grade silicon carbide membrane mask. Figure 3 shows Mylar film stretched over a circular ring mount.

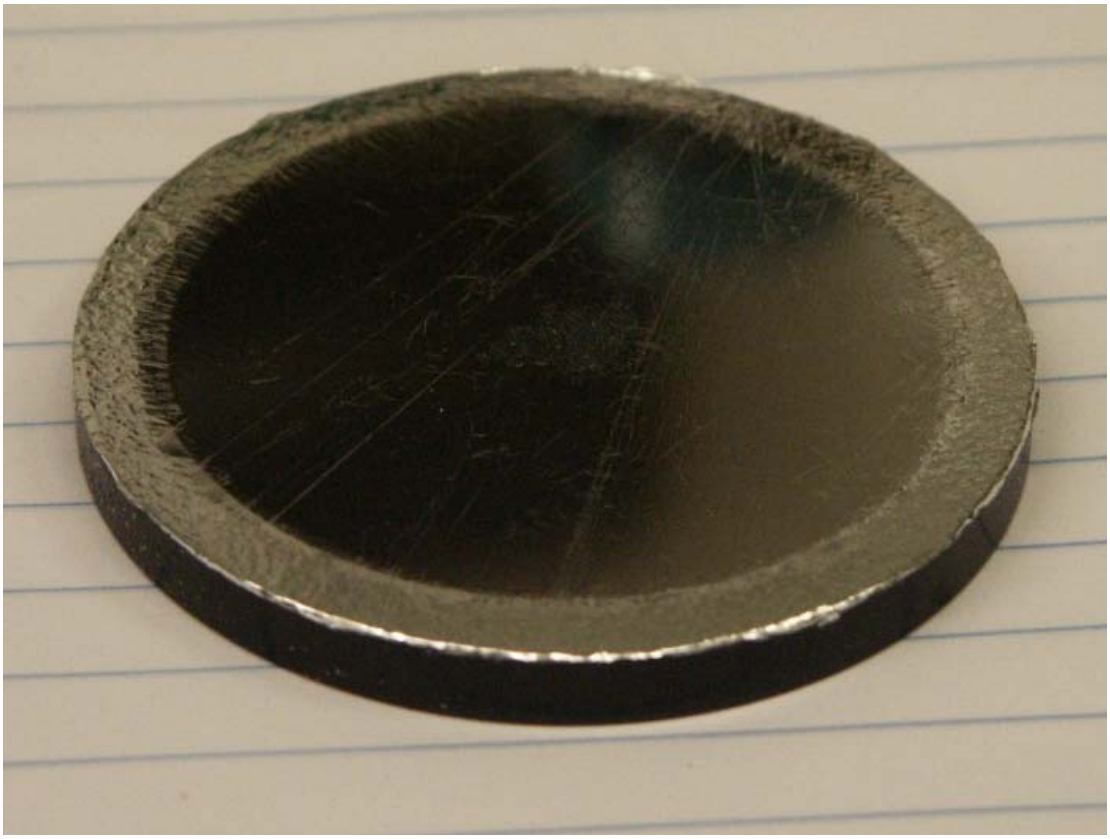

Figure 3: Mylar film membrane mask surrogate stretched over ring

Chapter 2: Aeroelasticity System

2.1 Background

The membrane mask is an important part of the x-ray lithography process. The mask combines the pattern and optical systems. The basic mask structure depends on the optical properties of x-rays. The transparent part, the carrier, must be transparent enough to allow for fast exposures, and yet be able to withstand handling and radiation damage. The mask consists of an absorber layered on top of a membrane (substrate) which is opac to x-rays. In general, the membrane will be of the order of 1 to 2 μm thick. Currently used mask membranes are fabricated with silicon, silicon nitride, or silicon carbide. Prototype masks of diamond have also been produced. Gold, or tungsten or titanium are used as absorbers. Absorbers block x-rays from going through the mask. The membrane is mounted on a 3" or 4" silicon wafer which is bonded to a rigid ring (e.g. Pyrex) Mask. Various techniques are used to mount a thin, uniform membrane on a structurally rigid holding frame. The pattern is applied on the membrane, and the mask is mounted on the exposure and processing tools using the frame. [16]

Proximity lithography requires placing the membrane mask into close proximity with the exposure wafer prior to exposure with radiation, such as x-rays. In

a production environment, concerns arise as to whether rapid proximity positioning will cause deleterious aeroelastic loads on the membrane.

The term aeroelasticity deals with the study of the mutual interaction between aerodynamic forces and elastic forces acting on a structure. A structure immersed in a moving fluid flow field is subjected to surface pressures induced by that flow. If the pressures cause the structure to deform significantly, it changes the boundary conditions of the flow and the resulting fluid pressures. These changes in the fluid loads can cause feedback instabilities. An example of this is panel flutter; in which a high-speed passage of air along the panel causes sustained oscillation [8]. Aeroelastic mechanics can be analyzed by coupling the fluid mechanics effects with the elastic effects. This can be accomplished by matching the pressure and the displacement terms at the fluid-structure interface. [11]

2.2 Aeroelastic Mechanics

When modeling membrane aeroelastic mechanics there are several reasonable assumptions that simplify the analysis: (i) The membrane remains reasonably flat without wrinkling; (ii) Air is *incompressible*; (iii) The inhomogeneous absorber pattern affects the local mechanics of the mask, but at the macro scale of the entire mask, the absorber pattern produces homogeneous effects that are an average with the mechanics of the silicon carbide base; (iv) The membranes can deform in both in-plane and out-of-plane directions. The mechanics of the in-plane and out-of-plane

forces are largely uncoupled; (v) In-plane deformations can be adequately described by 2-D plane stress models; (vi) The out-of-plane deformations can be described by membrane mechanics [15]. The long span-to-thickness dimension ratio allows for ignoring plate-like bending effects. If the membrane has a high initial pre-stress (as is the case with silicon carbide) then a linear membrane model can be used with the differential equation. (1) (See appendix B for details)

$$T\nabla^2 w(x,y) = -p(x,y) \qquad \textbf{(1)}$$

Where w(x, y) is the out-of-plane deflection, p(x,y) is the pressure differential across the membrane and T is the pre-stress tension. This equation is based on several assumptions: 1. There are initial pre-stresses (T) on the membrane; 2.There are no appreciable bending effects; 3. The geometric stiffening due to tension is linear i.e. $T \approx T + \partial T$, where ∂T is equal to the change in tension due to deflection; 4.The membrane material behaves as a linear elastic solid. [12]

For a circular membrane that is clamped with zero displacement on the circumference boundary, equation 1 can be solved in cylindrical coordinates. (2)

$$w = \frac{P}{4T}(R^2 - r^2) \qquad \textbf{(2)}$$

Where R is the total radius of the membrane, and r is the radial distance from the center of the membrane. (This equation is derived by Den Hartog, [12] the derivation is shown in Appendix B.1)

The geometry of the gap between the mask and the wafer exerts a significant influence on the fluid mechanics. The horizontal span of the gap ranges from 50 to 300 mm, with a nominal thickness of between 5 and 100 μm. With these gap geometries, relative movements between boundaries give rise to hydrodynamic fluid motions and forces the two main maneuvers of concern with hydrodynamic fluid mechanics are; gap closing, and lateral stepping at gap, Figure 4 and Figure 5. For these geometries and maneuvers, the viscous forces dominate over the inertia forces (low Reynolds number flow). Typical Reynolds numbers range from 363 to 727 (See Appendix B-2 for calculations)

Due to the small gap distance there has been concern that classical fluid mechanics may not apply, and micro-fluid mechanics effects may need to be considered. After a check on of the Knudsen number, it was confirmed that classical fluid mechanics applies for most cases, with the possible exception of using low vacuum levels with a helium ambient and very small gaps (5 μm). Typical Knudsen numbers range from 0.0012 to 0.0005. For a small gap of 5 microns, the Knudsen number becomes 0.0124. [16] (See Appendix B-3 for calculations)

In the gap closing maneuver, as the mask is moved in closing the gap between itself and the wafer, the air in the gap is squeezed out through the boundaries at the

perimeter. This causes the membrane to bulge out-of-plane until the excess air in the gap has escaped. In many respects this is comparable to the mechanics encountered in squeeze film damping [7]. Although gap closing aeroelastic effects are an issue of concern, they are not considered in this thesis. The focus of this thesis is on the aeroelastic mechanics of lateral stepping.

2.3 Theoretical Model

Horizontal movement of the wafer relative to the mask, or lateral stepping, is in many respects very similar to the hydrodynamic lubrication of bearings. The pressure that develops on the membrane is described by Reynolds' lubrication equation.

There are several important and reasonable assumptions needed to derive the full Reynolds equation (3). These assumptions are: 1.There are no field forces acting on the fluid, such as gravity. Therefore, body forces can be neglected; 2. The pressure is constant through the thickness of the film; 3. Surface velocities do not vary in direction, due to the fact that the curvature of the surface is large in comparison to the film thickness; 4. There is no slip at the boundaries. The velocity of the fluid layer adjacent to the boundary is the same as that of the boundary; 5. The stress is proportional to the rate of shear, i.e. the fluid is Newtonian; 6. The viscosity is constant through the film thickness; 7. The inertia of the fluid is neglected; 8. The flow is laminar; 9. The stepping velocity U is constant [2]. The stepping maneuvers

encountered during production contain acceleration and deceleration components. Since the aeroelastic mechanics are dominated by vicious and not internal forces, the assumption of constant stepping velocities is reasonable.

$$\frac{\partial}{\partial x}\left(h^3\frac{\partial p}{\partial x}\right)+\frac{\partial}{\partial y}\left(h^3\frac{\partial p}{\partial y}\right)=\eta\left(6U\frac{dh}{dx}\right) \quad \textbf{(3)}$$

Where x is an in-plane coordinate in the direction of the stepping motion. y is an in-plane coordinate transverse to the direction of stepping. h(x, y) is the gap. p(x, y) is the differential pressure across the membrane. η is the dynamic viscosity. And U is the stepping velocity.

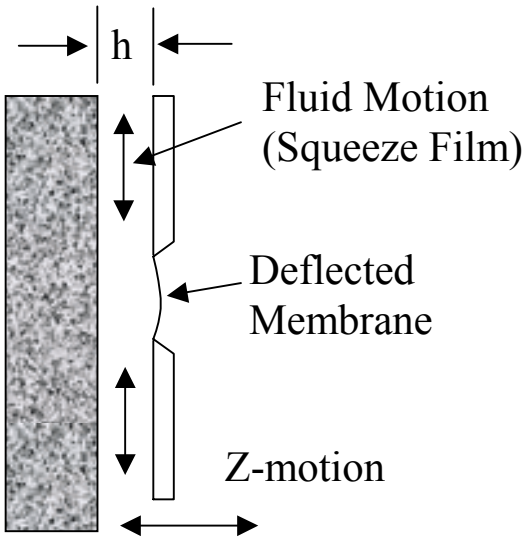

Figure 4: Geometry of gap closing maneuver.

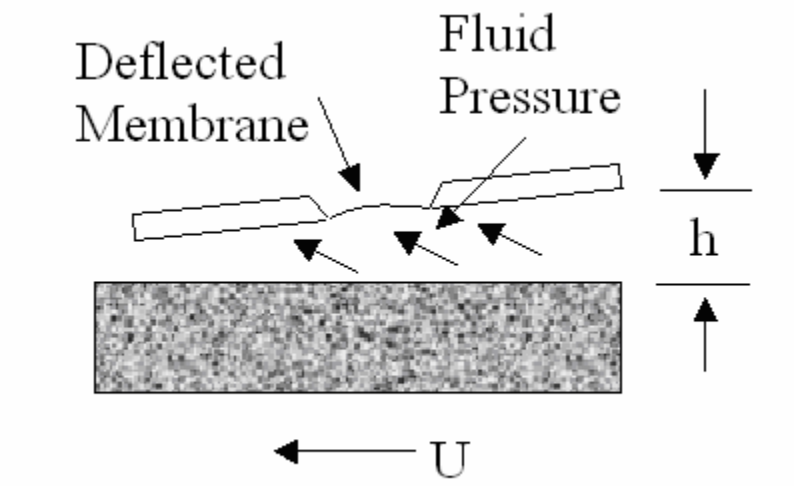

Figure 5: Geometry of a lateral stepping at gap maneuver with a converging wedge angle. (In-plane forces on the membrane may be important, but are not included in this model.)

There are several behavioral patterns, of the pressure, resulting from the horizontal stepping movement, U. The max pressure is proportional to: (1) The inverse cube of the gap dimension, h; (2) the wafer diameter; (3) the wedge angle, $\alpha = dh/dx$; (4) the stepping speed, U. [15]

Chapter 3: Numerical Calculation

3.1 FEMLAB

The majority of the aeroelastic numerical calculations were performed using FEMLAB. FEMLAB is a powerful interactive environment for problem solving that performs equation-based multi-physics modeling. Aeroelasticity being a coupled elastic and aerodynamic phenomenon is potentially a natural fit for the multi-physics capabilities of FEMLAB. The FEMLAB software allows the user to draw geometric shapes and apply boundary conditions and related differential equations.

3.2 Modeling Equations

Aeroelastic simulations of lateral stepping were modeled for two basic geometries. 1. The main geometry being the circular ring. This was used for the bulk of the testing. 2. The equations were also modeled for a rectangular geometry with dimensions of a ten to one ratio. This was done to simulate an infinitely long geometry, with simpler one dimensional mechanics.

3.2.1 FEMLAB Model Verification Studies

Several sets of calculations were performed using FEMLAB. The first calculations were designed to verify that the FEMLAB model was working correctly.

3.2.2 Rectangular Geometry

In an effort to verify that the FEMLAB model was working correctly, a rectangle with a 10:1 ratio width in the cross-flow was examined. This effectively converted the membrane aeroelastic mechanics into a 1-D problem. The shape with correct dimensions (10 cm by 1cm.) was drawn and the boundary conditions were set. The pressure and deflection were assumed to be zero at the boundaries. The elastic mechanics equation was created using Poisson's equation, and the Reynolds equation was created using the heat equation.

3.2.3 Hand Calculations

Hand calculations were performed on a 10:1 rectangle in order to verify the results from FEMLAB. An iterative method was used. The first step was to assume a deformed shape for the membrane. Next the hydro dynamic pressure due to stepping was calculated with Reynolds equation. The calculated pressure was applied to the membrane to obtain an updated membrane deflection.

The Reynolds equation is rewritten in one dimension, with the assumption that gradients in the y-direction are negligible.

$$\frac{d}{dx}(h^3 \frac{dp}{dx}) = 6U\eta \frac{dh}{dx} \quad \textbf{(4)}$$

Assume a deformed membrane shape, $h = h_e$

Therefore equation (4) becomes;

$$\frac{d}{dx}(h_e^{\,3} \frac{dp}{dx}) = 6U\eta \frac{dh}{dx} \quad \textbf{(5)}$$

Where h_0 is give by equation (6).

$$h_e = h_0 + \frac{dh}{dx} x \quad \textbf{(6)}$$

Where h_0 is the height of the angled membrane in relation to the granite block at position x1, and $\frac{dh}{dx}$ is the wedge angle in radians.

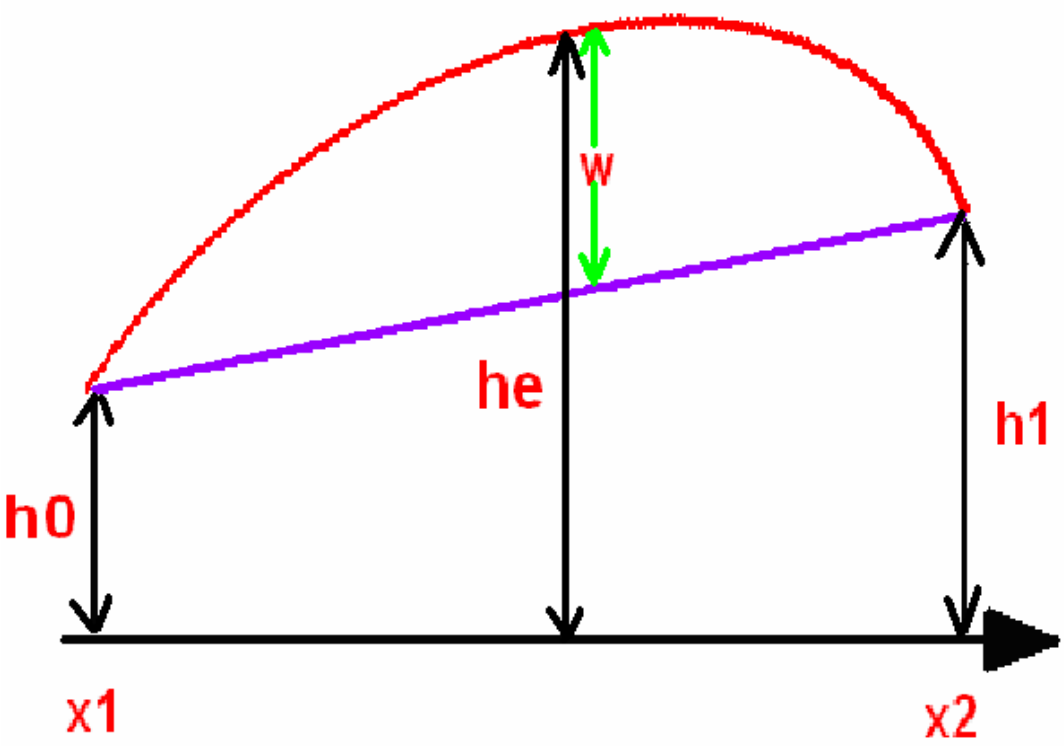

Figure 6: Variables for the film in reference to the granite block.

Figure 6 shows the constants used in the hand calculations. h_0, h_1, x_1, x_2 are all known constants.

Substituting into equation 6 in for h_e, h_e^3 becomes;

$$h_e^3 = h_0^3 + 3h_0^2 \frac{dh}{dx} x + 3h_0 (\frac{dh}{dx})^2 x^2 + (\frac{dh}{dx})^3 x^3 \quad \textbf{(7)}$$

When substituted into equation (5) this yields;

$$\frac{d}{dx}((h_0^3 + 3h_0^2 \frac{dh}{dx} x + 3h_0 (\frac{dh}{dx})^2 x^2 + (\frac{dh}{dx})^3 x^3) * \frac{dp}{dx}) = 6U\eta \frac{dh}{dx} \quad \textbf{(8)}$$

Equation (8) is then solved for p(x). Once p(x) is found it can be used in the membrane equation (9).

$$\frac{d^2w}{dx^2} = \frac{-p(x)}{T} \tag{9}$$

This is a 2nd order ODE that is solved for w(x) using MathCAD. (See Appendix B.4) Knowing h_e from equation (6) and w from equation (9), h can then be found using the relationship in equation (10).

$$h_{e2} = h_e + w(x) \tag{10}$$

The value of h obtained from equation (7) is then put in place of our original assumption and input into equation (4), and the entire process is repeated until h_e converges, $(h_{e(n+1)} = h_{e(n)})$.

3.2.4 FEMLAB Rectangle

FEMLAB was used for the same 10 x 1 triangle solved for in the hand calculations. The constants used in the equations for the infinitely long rectangle are shown in Table 1.

Table 1: Constants used in the coupled Reynolds and elastic mechanics equations of the infinitely long rectangle.

U	0.20 m/sec		Velocity of moving granite block
nu	1.80E-05		Viscosity of air
h1	2.29E-04 m		Large distance from block
h0	1.52 E-04 m		Small distance from block
k	h1/h0-1		
B	0.01 m		Length in direction of motion
H	B/k		
hco	h0*k/B		
talpha	h0/H		

The membrane mechanics equation (11) and Reynolds lubrication equation (12) couple to produce a description of the aeroelastic deformation during lateral stepping at gap. These coupled field equations were simulated on FEMLAB.

$$p = -T\nabla^2 w \qquad \textbf{(11)}$$

$$\frac{\partial}{\partial x}\left(h^3\frac{\partial p}{\partial x}\right)+\frac{\partial}{\partial y}\left(h^3\frac{\partial p}{\partial y}\right)=6U\eta\frac{dh}{dx} \quad \textbf{(12)}$$

The initial calculations used a pseudo-coupling technique where the pressure was initially calculated using Reynolds equation and the pressure was then applied to the membrane equation to calculate deflections. Pseudo coupling is an approximate technique that works well if the membrane deflection is small. If the membrane deflection becomes significant compared to the gap size, then pseudo coupling becomes inaccurate and full coupling needs to be considered. An advanced feature of the FEMLAB software is that it enables direct calculation of coupled field equations. Full coupled membrane-Reynolds equations were successfully implemented and are shown below. The finite element simulations confirmed the general concepts developed from mechanical principles.

To create the elastic mechanics equation (11) in FEMLAB, Poisson's equation was used. (13)

$$-\nabla(c\nabla w)=f \quad \textbf{(13)}$$

Where w is the dependent variable (deflection of the membrane)

c = T = tension per unit length (a known constant value) = constant

And f = p(x,y) (A value from Reynolds equation, pressure)

To create the Reynolds equation (13) the heat equation was used, which has the generic FEMLAB form (14).

$$d_a p' - \nabla(c\nabla p) = f \quad \textbf{(14)}$$

Where p is the pressure from equation 6, d_a = 0, c = h^3 (height of the film as a function of position). And $f = \frac{dh}{dx}$ (partial derivative of the c term with respect to x)

The partial derivative of h with respect to x is defined as.

$$\frac{\partial h}{\partial x} = \text{talpha+w} \quad \textbf{(15)}$$

So written in terms of the constants Reynolds equation is transformed

$$-\nabla(h^3\nabla p) = (6*U*niu)*(talpha + w) \quad \textbf{(16)}$$

Using the constants for the pressure, tension equation the original equation is rewritten.

$$-\nabla((36)\nabla w) = p \qquad \textbf{(17)}$$

Therefore with respect to the heat equation in FEMLAB, c= (h)^3, and f is the right hand-side of (16). (A constant times the partial derivative of the c value with respect to x)

Typical results are shown below. The nominal wedge gap runs from 30 to 20 μm across the membrane. The gap was filled with air at 1 atm. The lateral stepping speed was 0.2 m/s. The membrane was 2 μm thick Mylar with a pretension of 4.5 (kg/m)

3.2.3 Rectangular Tests / Results

Values for the gap, wedge angle and velocity were input into FEMLAB so as to closely match those of the experiment in the aeroelasticity rig. The block velocity

was set at a constant velocity of 0.2 m/sec. The distances of h0 and h1 were set to various values that defined the wedge angle and gap.

FEMLAB solved these equations and produced a two-dimensional (Figure 7) and a three dimensional (Figure 8) graphical output, a typical result from these calculations was that as the wedge angle increased, the deflection also increases and the position of the maximum deflection shifts toward h0. Also as the gap decreased, the maximum deflection increased. As the velocity increased it caused the maximum deflection to increase and caused the position of maximum deflection to shift toward the leading edge of the membrane. Even though this equation was modeled in two dimensions, it is shown that at the center of the rectangle the model is acting as a one dimensional problem, with the x-dimension being critical and the y-direction gradients being negligible.

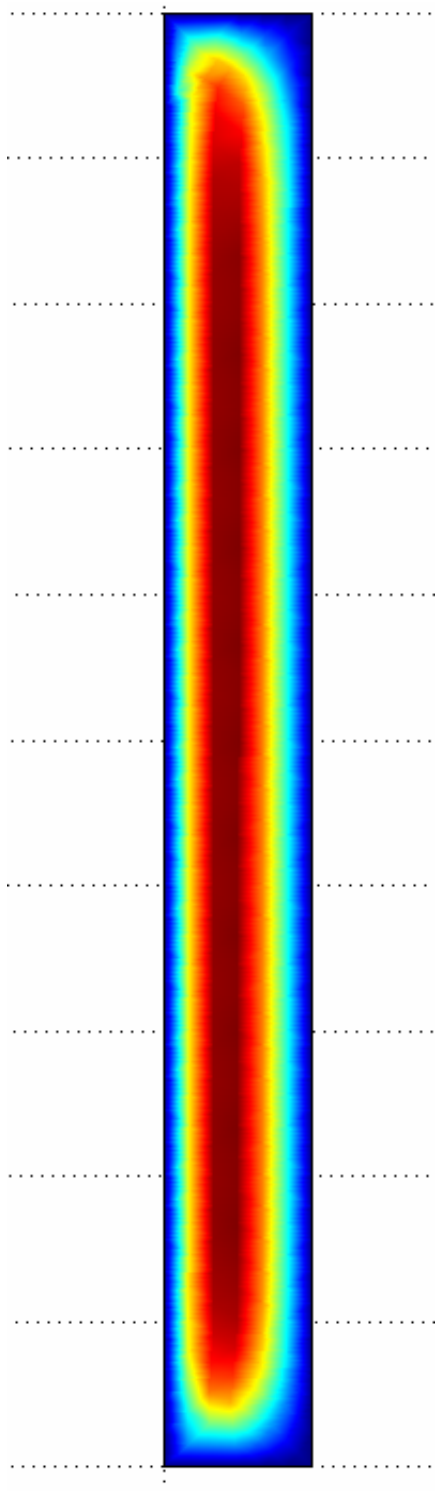

Figure 7: FEMLAB 2-D solution for elongated rectangle

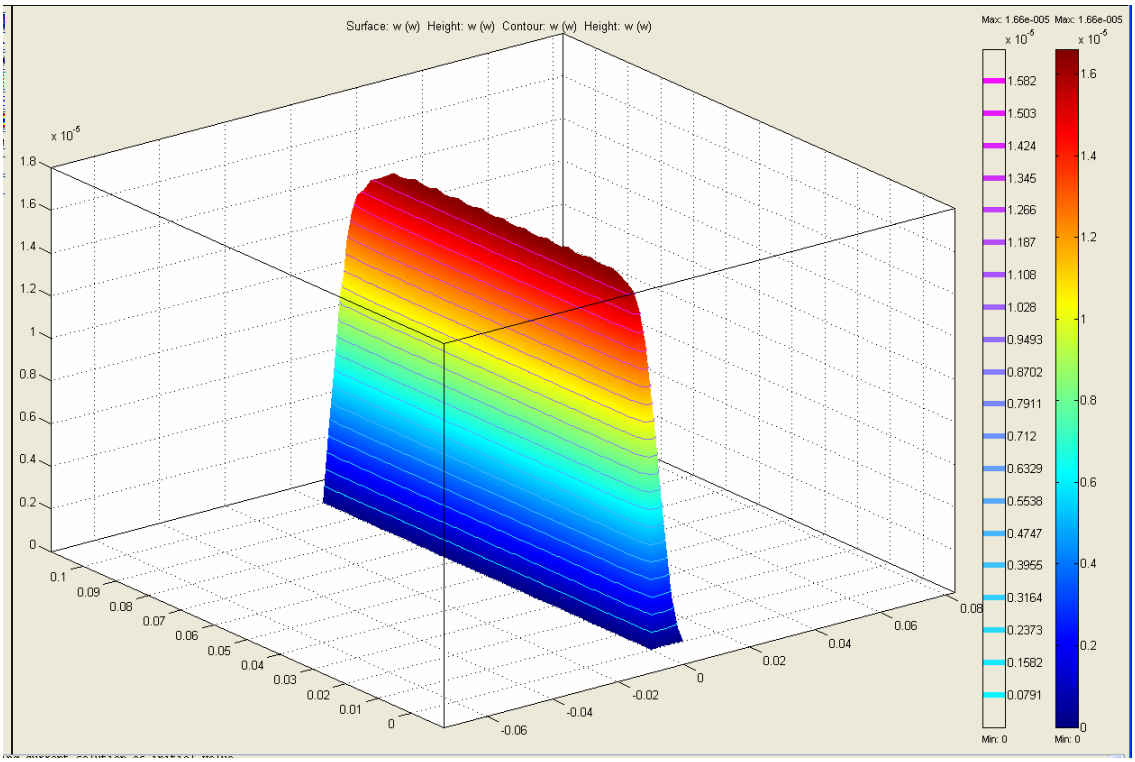

Figure 8: FEMLAB 3-D solution

3.2.4 Circular Geometry

Calculations were performed for a circular geometry as well. The elastic mechanics equation was created using Poisson's equation, and the Reynolds equation was created using the heat equation format from FEMLAB. The same methods were used as before for the Rectangular geometry.

The constants used in the equations for the circular geometry are the same as the rectangular geometry, but with different values for the geometry and position of the membrane. (Table 2)

Shown in Figure 9 are the constants used in this model.

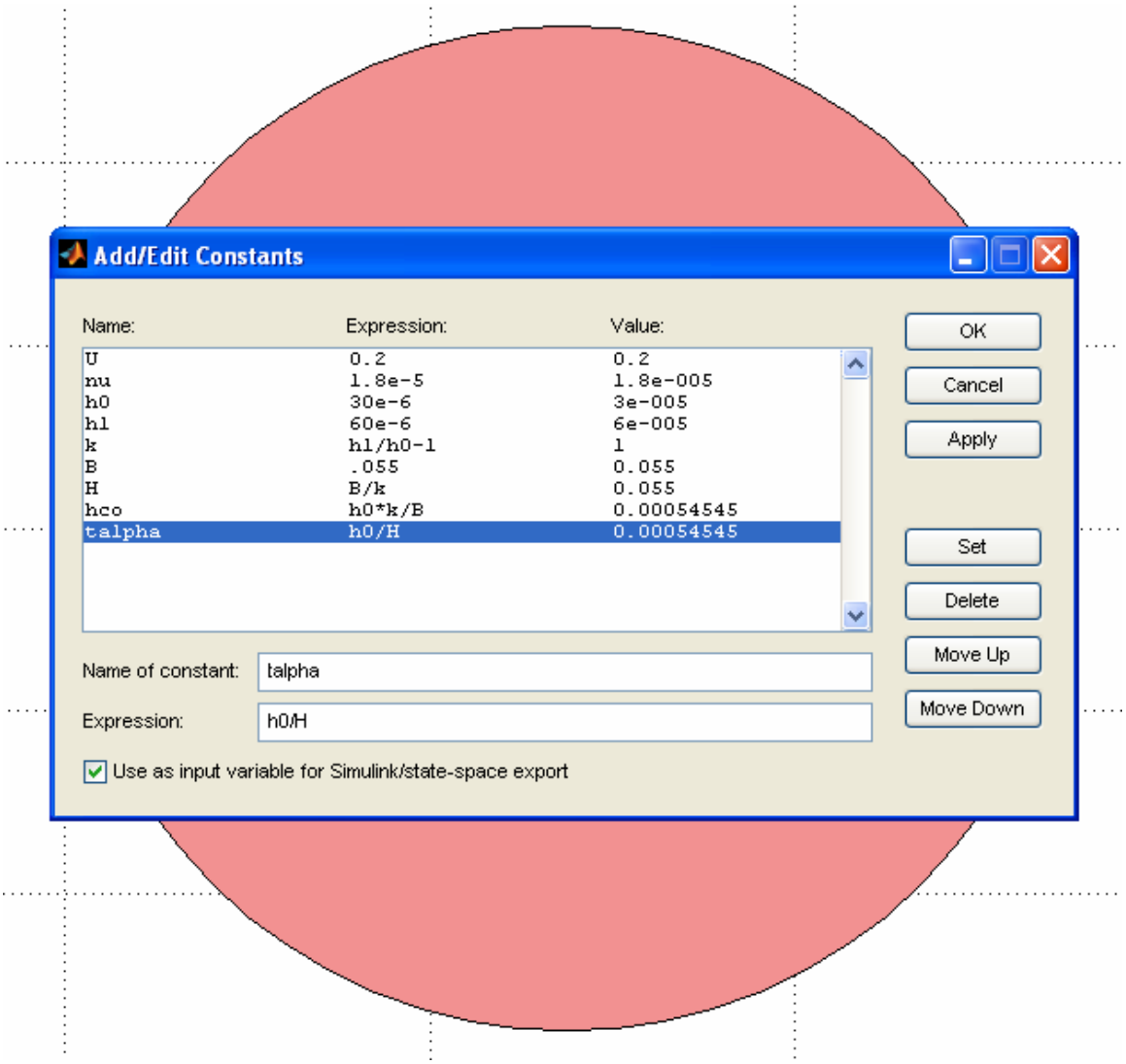

Figure 9: FEMLAB model of the Mylar mask with the constants used in the equations (These constants are explained in Figure 2.)

Table 2: Input constants used in the coupled Reynolds and elastic mechanics equations that represent the position of the mask relative to the granite block

U	0.20 m/sec		Velocity of moving granite block
nu	1.80E-05		Viscosity of air
B	5.53E-02 m		Diameter of mask membrane
h1	2.29E-04 m		Large distance from block
h0	1.52E-04 m		Small distance from block
H	B/k		
hco	h0*k/B		
talpha	h0/H		

3.2.5 Circular Tests / Results

Calculations were then done for the circular geometries. In the first set of calculations for the circular geometry the gap was held constant while the angle was varied. This configuration was repeated for different velocities. In the next set of

calculations, the angle was held constant and the gap was varied, this was also repeated for different velocities.

For the first set of calculations it was found that as the angle of the mask was increased with a constant gap and velocity the max deflection increased as well. Also as the angle was increased, the position of maximum deflection on the surface of the mask was shifted toward the lower side.

For the second set of calculations, it was found that as the gap gets smaller and the wedge angle and velocity remain constant, the deflection gets larger. It was also found that as the velocity increases, the deflection increases. Typical results are shown in Figure 10 and Figure 11.

For both of these sets of calculations, the deflection versus angle and velocity relations were linear over a limited range. There is a critical angle, gap and velocity that will cause the deflection relations to deviate from linearity. Also when all three variables are changed at the same time the affect on the deflection is much more difficult to predict without the aid of FEMLAB.

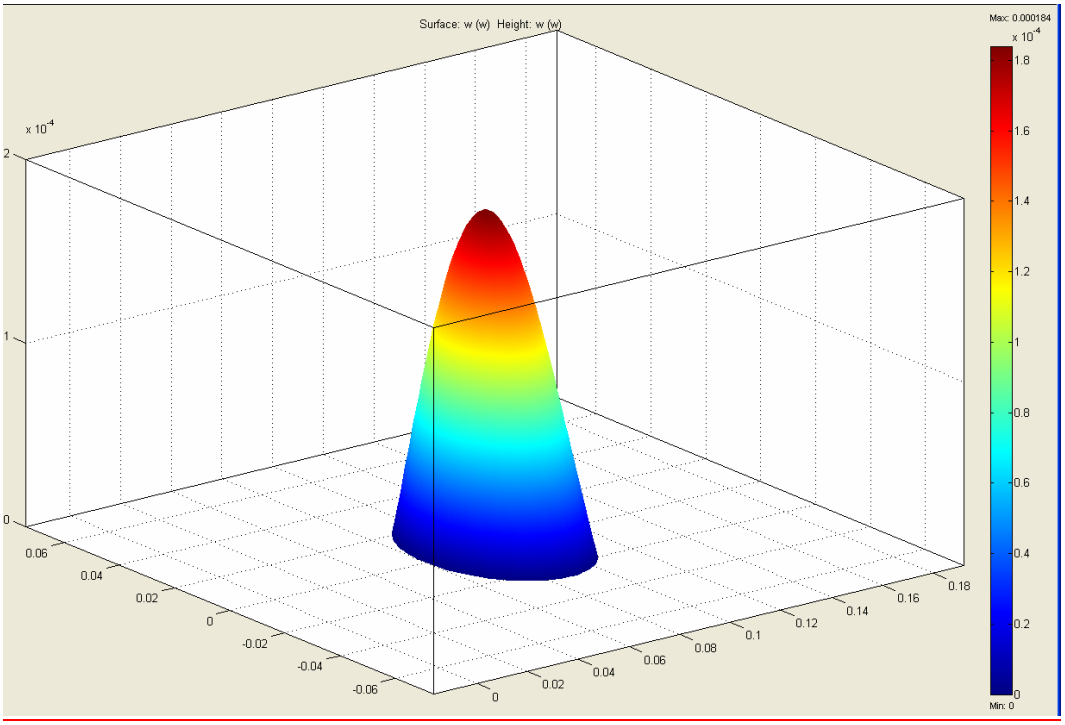

Figure 10: Three-dimensional deflection graph for circular geometry membrane

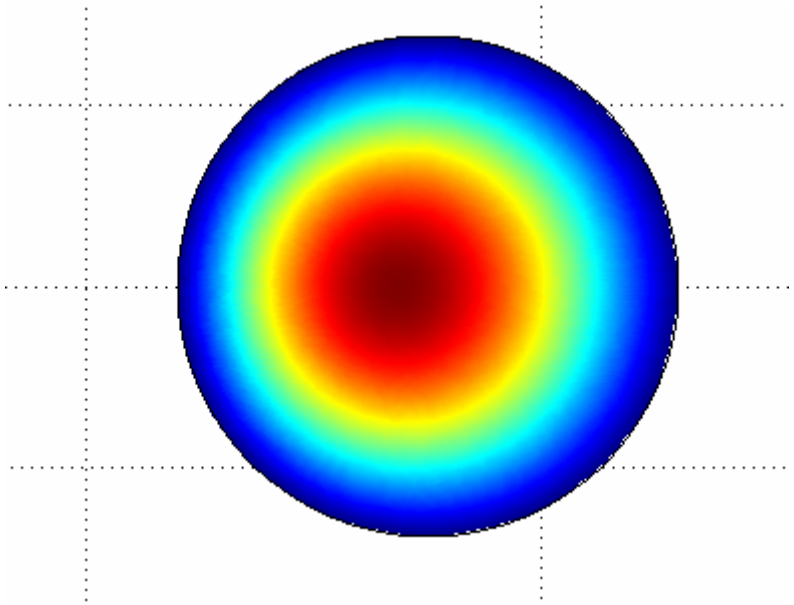

Figure 11: Two-dimensional deflection graph for circular geometry

Chapter 4: Experimental Test Beds

4.1 Rig Setup

An experimental test rig was built to validate the physical and mathematical models of thin membrane aeroelastic mechanics. To this end a test rig was built to simulate the lateral stepping maneuvers with thin film membrane masks used in the x-ray lithography system developed by JMAR systems inc. (S. Burlington, VT). The initial prototype of this test rig was built by Sonja Holzl [11]. The test rig was subsequently modified and upgraded as part of this thesis. The basic lateral stepping maneuver begins with the wafer being held in close proximity to the membrane mask with a gap of nominally 5 to 100 microns. The membrane mask is placed on rigid mounts. The wafer then moves quickly in a direction lateral to the stationary membrane mask while maintaining the same close proximity gap.

In an effort to build a test rig that captures the essential mechanical features of lateral stepping while eliminating other complications in a production stepper a system was designed and build that used a polished flat granite block sliding on air bearings to simulate the stepping wafer.

Shown in Figure 12 is the test set up of the thin film and the granite slab. The granite slab rides on air-bearings, moving back and forth, causing the film to deflect. The objective of this study is the aeroelastic affects of the gap (5-100 microns), wedge angle, and velocity of the block. The objective of the non contact sensor is to

measure the gap between the thin film (flat, un-deflected position) and the polished flat impala (black) granite block. The idea is to mount the sensors on the plate surrounding the thin film. The sensors are positioned to aim directly at the granite slab. Ultimately it is desired to use 3 sensors to replace the 3 dial indicators shown in the figures.

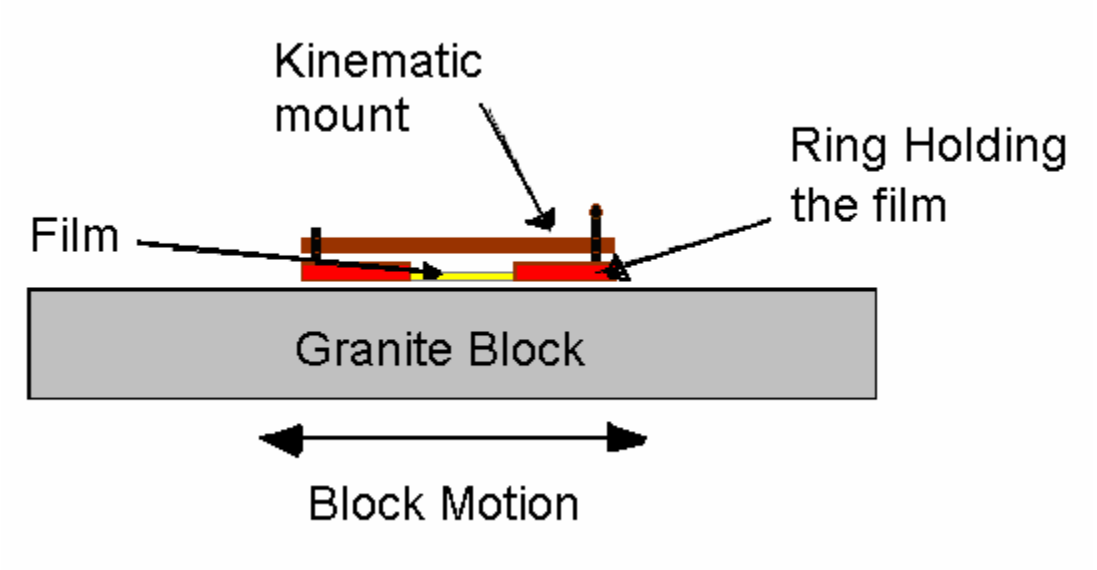

Figure 12: Top view of the aeroelasticity rig. The gap between the granite block and film is positioned between 3 and 200 microns.

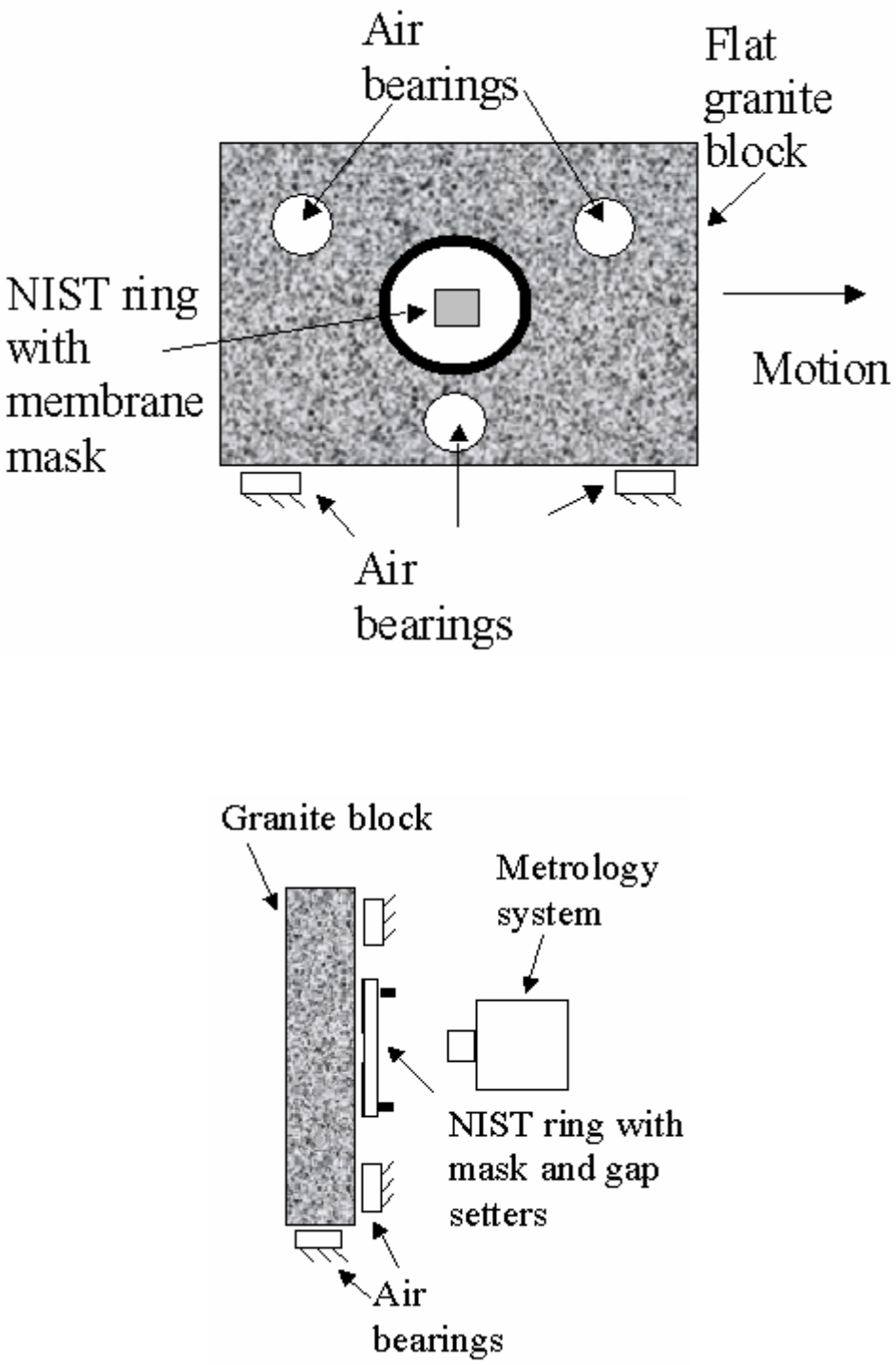

Figure 13: Front and side views of aeroelasticity rig.

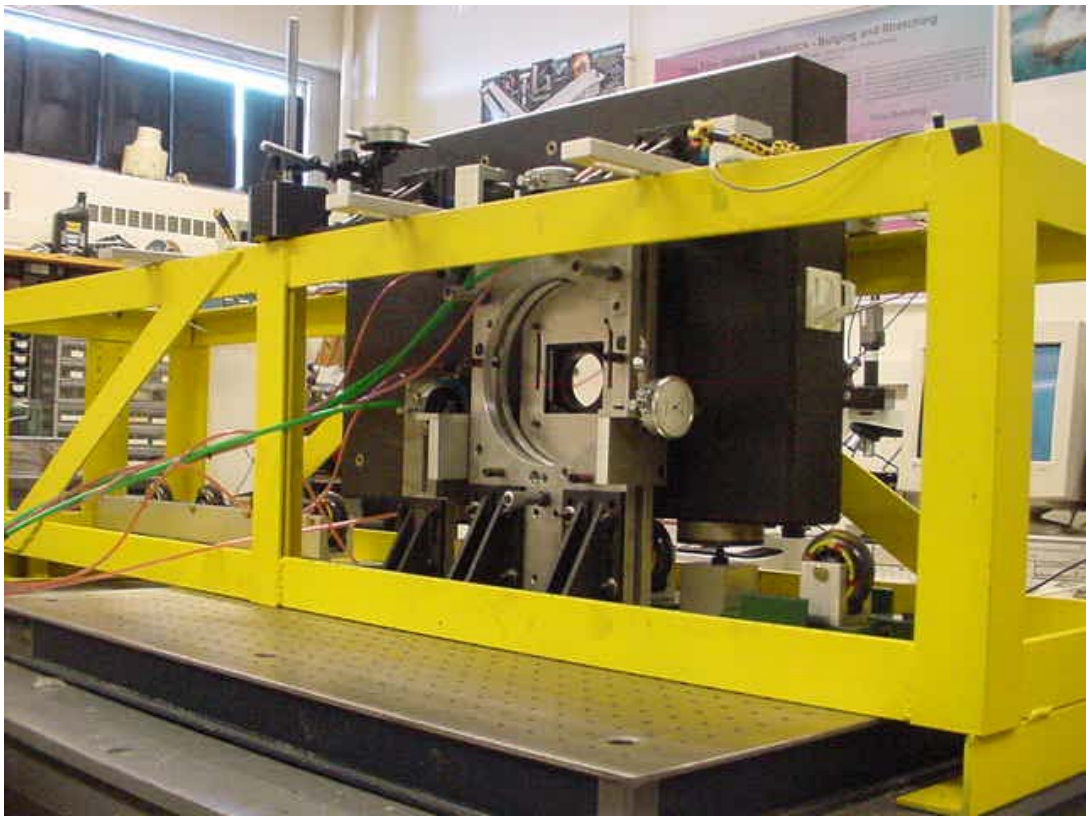

Figure 14: Aeroelastisity rig setup with mask metrology system removed.

Since the supply of silicon carbide membranes was very limited, the tests reported in this thesis used a round Mylar membrane, Figure 14. The use of Mylar was to show that this test set up could be used to find the aeroelastic properties of a silicon carbide mask that is used by JMAR in their x-ray lithography process. Future testing using a silicon carbide membrane is anticipated (1 micron thick), Figure 15.

Figure 15: Silicon carbide mask mounted in silicon wafer.

4.2 Mylar Film

The Mylar membrane was handmade by a process in which a piece of aluminum-coated Mylar was glued to a slightly beveled anodized aluminum ring and then heat shrunk to form a tight and smooth membrane (Figure 16).

Figure 16: Mylar film, 2 microns thick.

Mylar is a biaxially-oriented polyethylene terephthalate (BOPET) polyester film, developed by DuPont Teijin Films.

In manufacture, a film of molten PET is cast on a roll and subsequently stretched in and orthogonal to the direction of travel. One of its sides is microscopically smooth, while the other side contains microscopic asperities, which promote adhesion of coatings and printing media. Mylar can be aluminized, allowing a reflection of up to 99% of light and radiant heat. Like aluminum foil, aluminized Mylar has a shiny reflective side and a dull side.

4.2.1 Procedure for Mylar Film

In this stage of the experiment the first thing that was done was to create a new pellicle using the ring of the old blown pellicle. In order to do this the old film and adhesive was removed from the ring using acetone. The ring was then prepared with a very thin layer of M-Bond AE-10 bond epoxy. Next a sheet of 2 micron thick aluminized Mylar was stretched across a hole in the center of a flat metal plate, and the ring with the epoxy was placed face down on top of it. A small weight was then placed on top of the ring and the entire setup was placed under a heat-lamp overnight. The idea behind using the heat lamp was to first cure the core M-Bond AE- 10 bond epoxy and then once the adhesive had set, to also use the heat to help stretch the Mylar taught on the ring. After a night under the lamp, the ring pellicle was removed and the excess Mylar was trimmed off using a razor blade.

The Mylar pellicle was then mounted in the stand parallel to the granite slab. In order to make sure that the pellicle was completely parallel, the stand was moved

up flush against the granite slab so that the 3 balls on the face of the stand were touching the slab. Then the set screw at the top of the stand was loosened and the pellicle was placed inside so that it too was flush against the granite slab. Then the pellicle was tightened in spot with the set screw and the dial indicators were set to zero. After the parallel zero point had been established, the pellicle and stand were backed off to a flat parallel gap of 60 microns. This was done by turning the micrometers until the reading on all 3 dial gauges was at exactly 60 microns. Next, the optical displacement measurement sensor was set up, Figure 17.

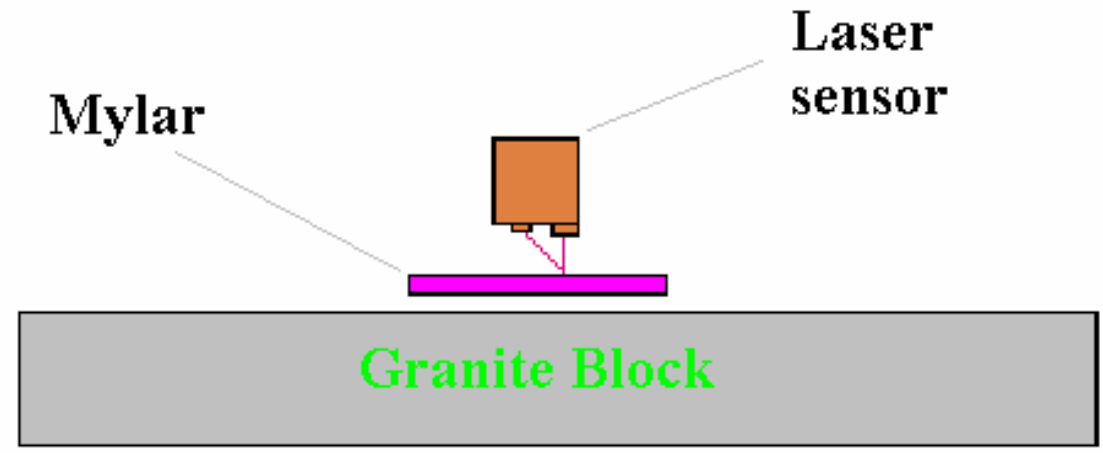

Figure 17: Setup of the optical displacement measurement sensor.

Once the gap was set and sensor was zeroed, the dial gauges were backed off, and the slab was set into motion at a constant velocity. This was accomplished by placing an elastic cord on either end of the granite slab, the slab was pulled back a set distance and released.

The deflection of the film was measured using the DAQ program that the displacement sensor was connected to.

Next the pellicle was set at various angles for a constant mean gap. These gaps and angle were established by setting the micrometers to certain distanced displayed on the dial indicators. These distances necessary to achieve the desired Mean gaps and angles were found using a Graphical User Interface (GUI) program written in MATLAB shown in Figure 18. This was done for various wedge angles set at several different constant mean gaps. For each of these, the block was again set into motion at a constant velocity, and the deflection of the Mylar film was recorded.

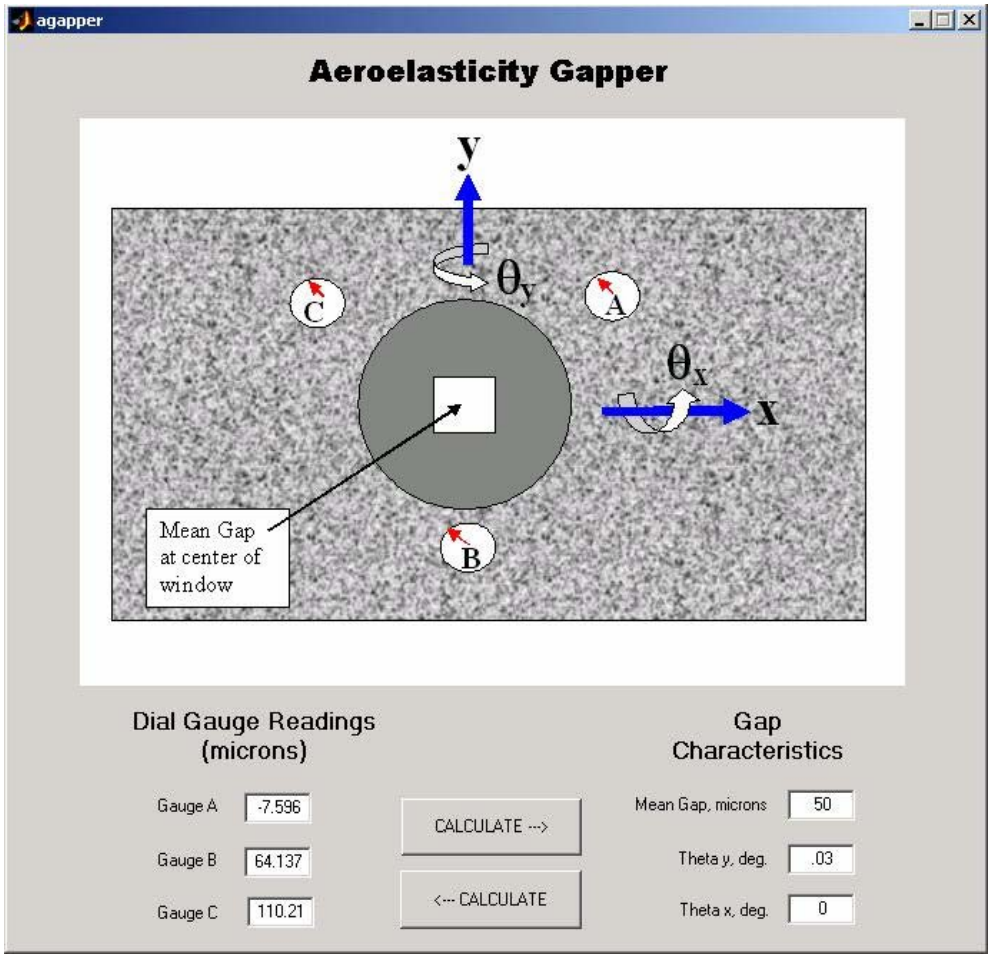

Figure 18: MATLAB GUI for calculating the wedge angle and mean gap from the dial gauges.

4.2.2 Tension Measurement Rig

The tension in the Mylar membrane is needed as an input for mathematical models of the aeroelastic mechanics. Therefore a system was built to measure the tension in the membrane by an indirect method that related differential pressure across the membrane to out of plane membrane deflection. In order to do this a pressure deflection measurement system was set up. An MKS power supply (type 246) was hooked up to an MKS mass-flo controller. Coming into one side of the mass-flo controller was compressed nitrogen from a tank. The power supply and mass-flo controller regulated the flow of nitrogen exiting the controller. After which the nitrogen gas was split into 2 paths. One path lead to the pressure transducer and digital read out. (MKS, Baratron pressure transducer, MKS PDR-D-1). The other path leads to flat stage with a hole over which the mask would be positioned. The mask was sealed to the stage with vacuum grease. Due to the two-way split in the tubing, whatever pressure was imposed on the Mylar film, the same amount of pressure would be sent to the pressure transducer and displayer on the read out in torr. (Figure 19)

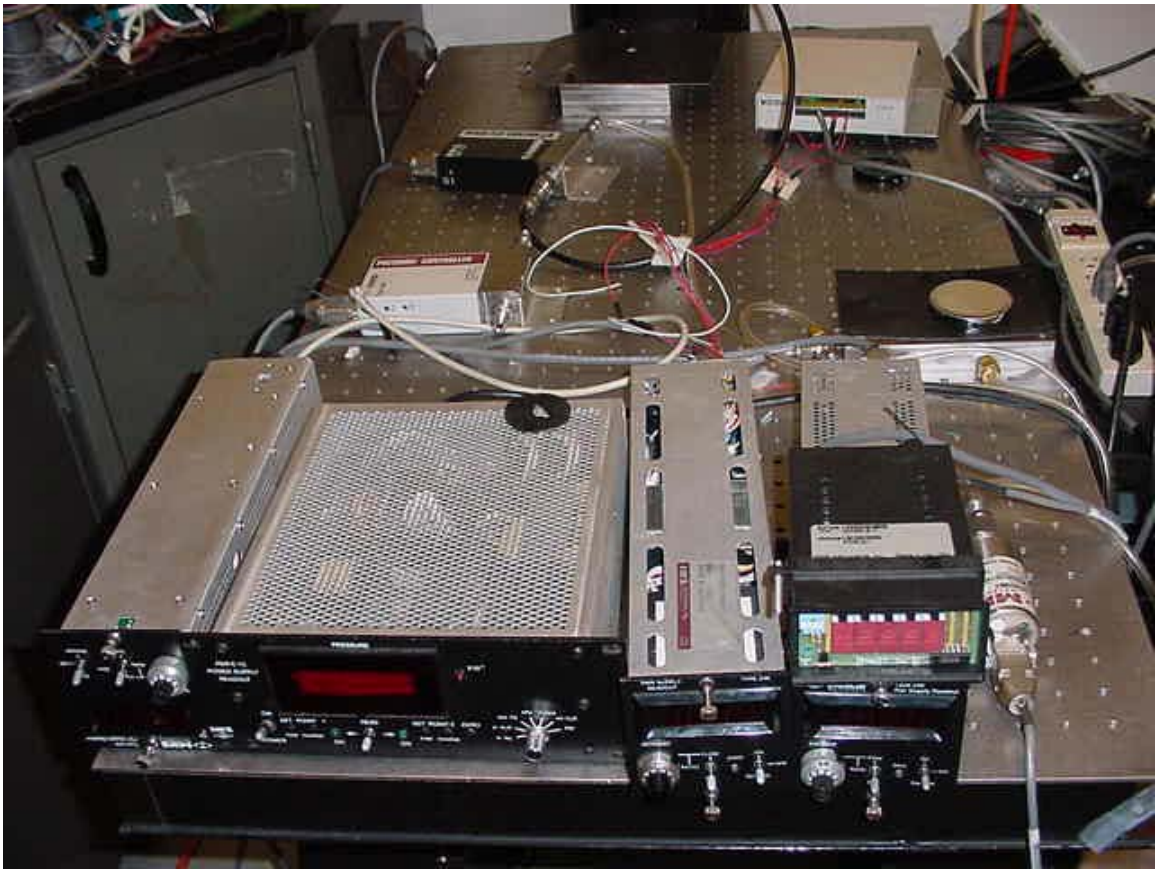

Figure 19: Pressure system setup.

The calibrated optical measuring sensor was positioned above the pressurized Mylar film. Various pressures from 0 to 1.0 torr were applied on the Mylar film. For each of these pressures the deflation was recorded using the optical measurement sensor. (Figure 20)

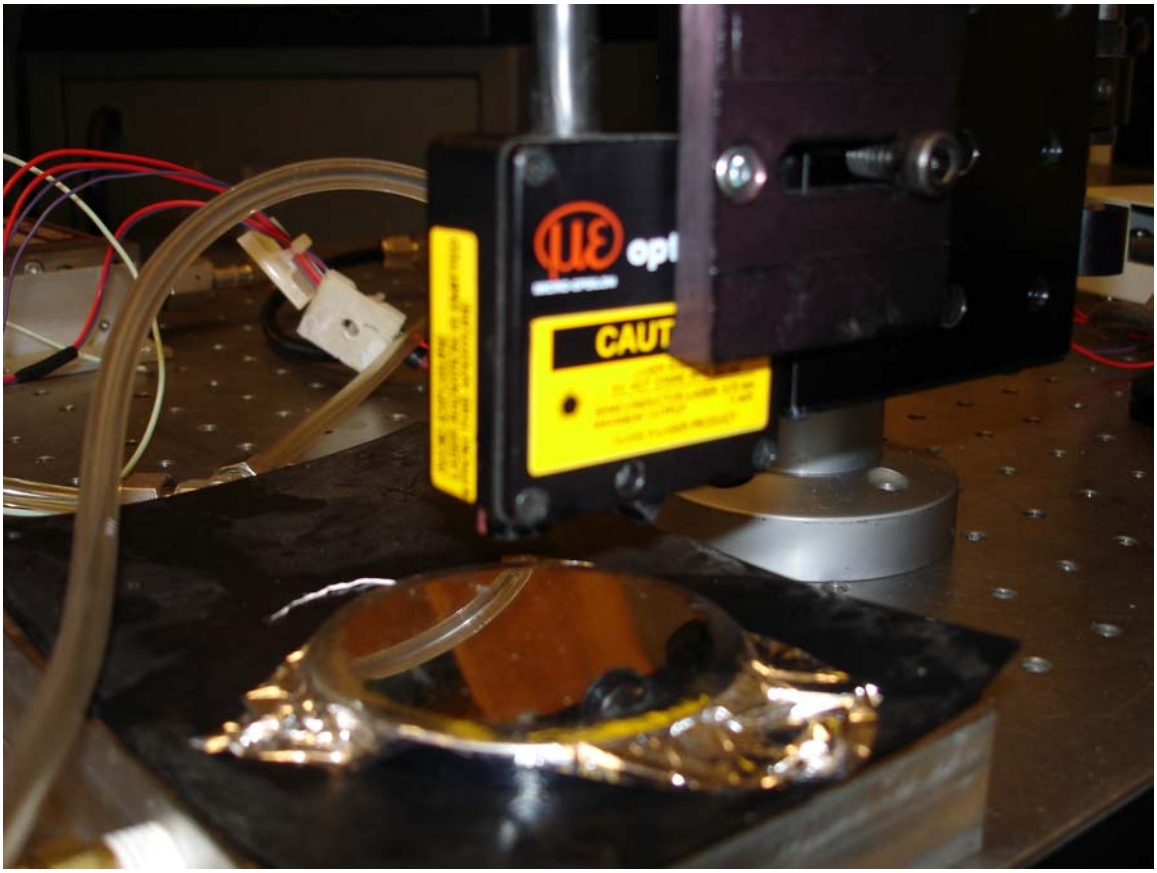

Figure 20: The optical displacement measurement sensor positioned over the mylar film with a known pressure applied to it.

4.3 Mask Positioning

The Mylar film mask was then mounted in the aeroelasticity rig so that it was parallel to the floating granite block Figure 21. An optical measuring sensor, Figure 22, was positioned perpendicular to the Mylar film.

An optoelectric system measured the movement of both the sliding block and membrane. Custom-built infrared timing gates measured the speed of the moving granite block.

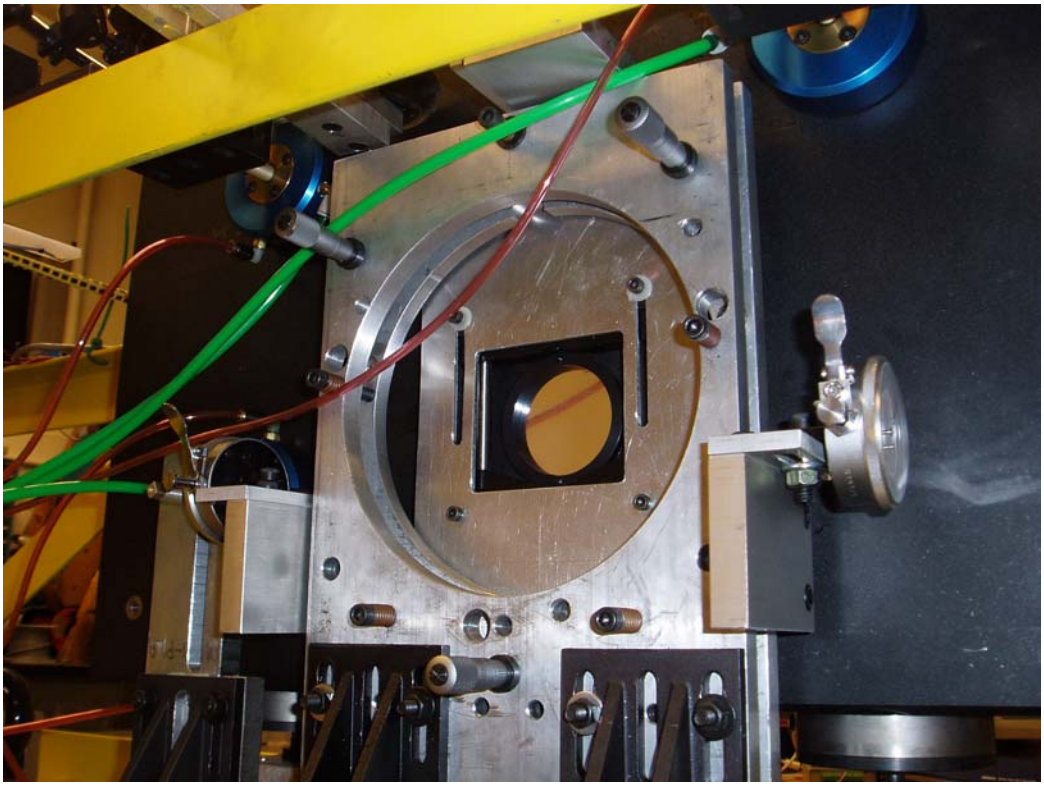

Figure 21: Modified kinematic mount and dial indicators

A laser Micro-Epsilon optoNCDT 1605 displacement sensor measured the deflection of the Mylar film. This sensor is positioned perpendicular to the surface of the film on a translation stage. The stage allows the operator to obtain deflection measurements at various positions across the Mylar film, Figure 23. All of the data

were digitized with a 16-bit resolution in the time domain at a rate of 100 samples per second with a DATAQ DI- 710.

Figure 22: Optical displacement measurement system

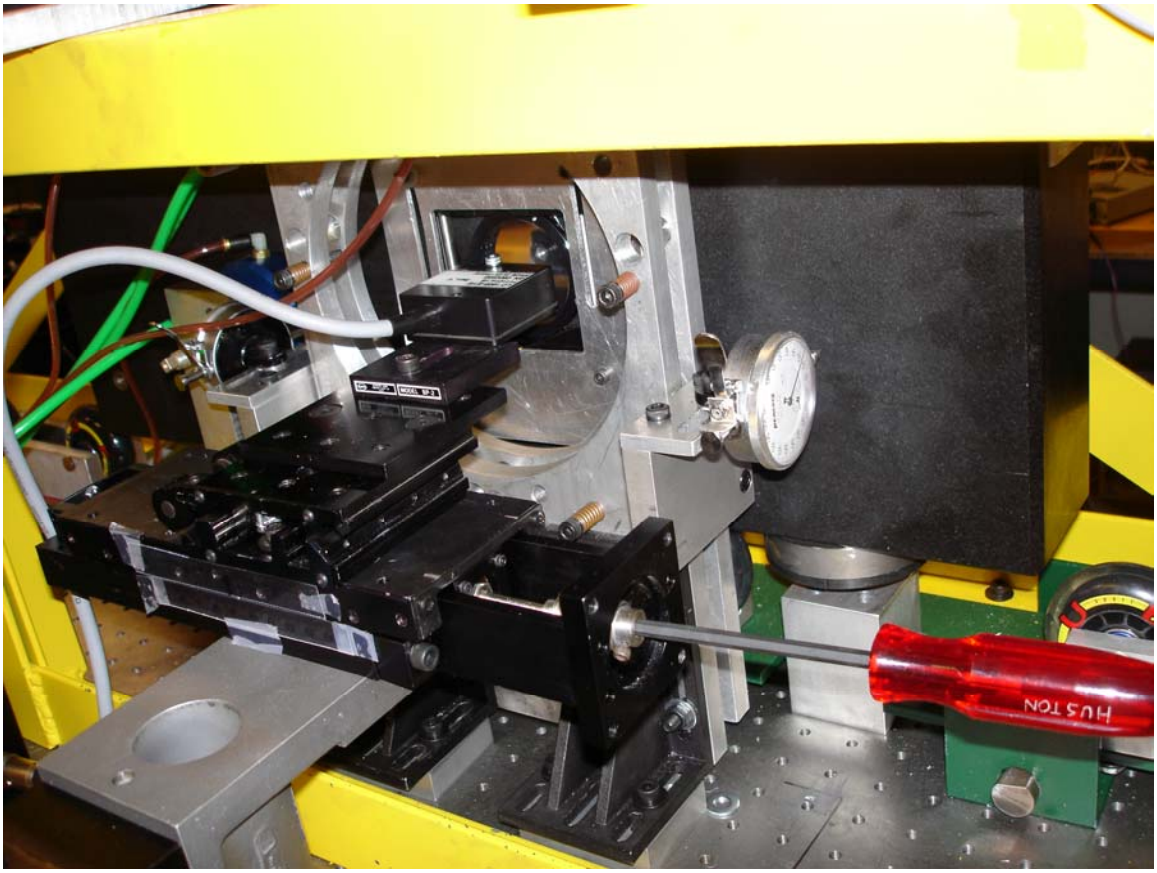

Figure 23: Translation positioning stage that moves the non-contacting optical displacement sensor across the surface of the Mylar film.

A polished flat granite block with dimensions 0.63m x .04m x 0.07m and weight of 54 kg was used to simulate the lateral stepping action of a wafer. In order to produce a pure translational motion five degrees of freedom were constrained by five air bearings. Preloading is necessary for an air bearing to produce a smooth motion. Two of the air bearings were of a push only type and were placed underneath the block so that gravity provided the preload. The remaining three were New-Way

model # .39479 with vacuum preloaded capability. These air bearings were placed on the side of the block. The block has elastic bungee bands on either end. Initially the block is pulled back a set distance, opposing the elastic band, and set into an oscillating motion, Figure 24. The velocity of the block is essentially constant due to the frictionless surface provided by the air bearings. At either end of the blocks path there is an infrared gating system (Figure 25), each time the block crosses between the gates at either end, the signal between then is broken. These gates measure the precise time that the block crosses in front of them. Knowing the exact distance between the gates at either end, the velocity can be calculated very accurately. Filtered infrared phototransistors were selected to eliminate any interference from the laser or ambient lighting, and low power IR emitters were selected to eliminate any potential for the timing gates to interfere with each other. The emitters and detectors use high strength neodymium magnets to allow rigid yet flexible mounting to the frame of the apparatus. This arrangement accommodated changes in aspects such as the elastic bands used and the length of the motion of the block. Through this method the velocity of the moving block is determined.

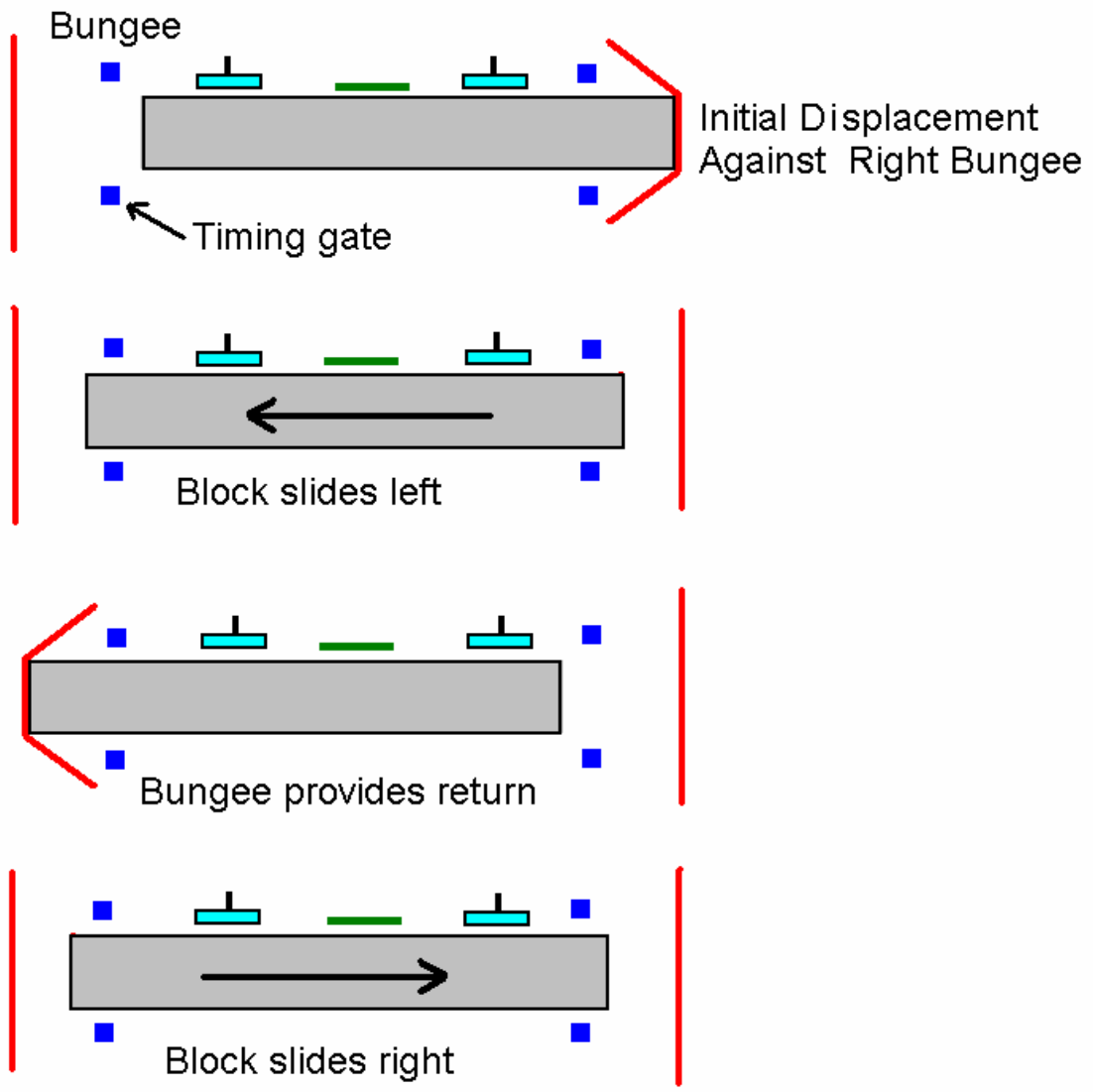

Figure 24: Motion of Granite Block

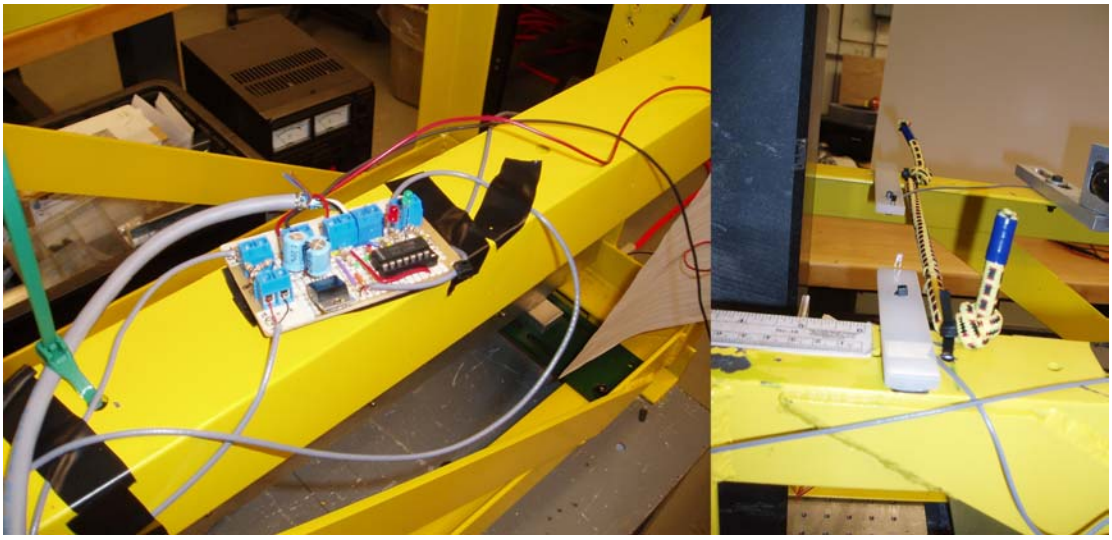

Figure 25: IR timing gates. Left portion shows control electronics and signal conditioning, right portion shows magnetically mounted IR emitter and photo-detector.

4.4 Optical Displacement Measuring System

The out-of-plane deflection of the membrane was measured with a Micro Epsilon optoNCDT 1605. This system was hooked up to a 24 V power supply and calibrated. The calibration was done using a micrometer and a dial gauge. The sensor was positioned over a flat steel polished steel plate, at various distances within its operating range of 0.5mm to 200mm.

For each of these distances a voltage output were recorded. This was done through the DATAQ D1-710 Screw terminal access Figure 26. The DATAQ was connected to the computer via USB. Through this calibration technique it was found that 1-micron displacement was equivalent to .005125 Volts.

Figure 26: DATAQ DI-710 screw terminal access

The optoNCDT 1605 optical measuring sensor, Figure 27, was positioned perpendicular to the Mylar film and hooked up through the DATAQ in the same time domain as the timing gates, which are used to measure the speed of the moving granite block

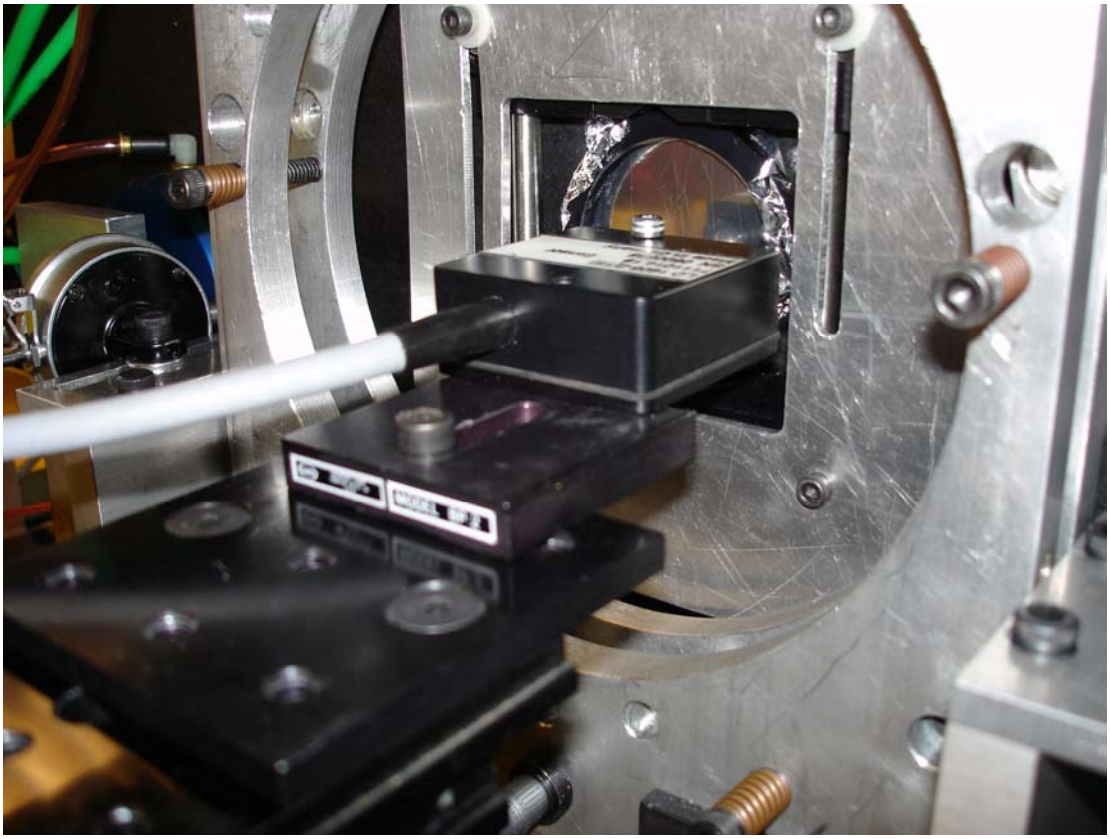

Figure 27: Optical displacement measurement sensor on mount perpendicular to Mylar film surface

The optical measuring sensor records the deflection at set positions of the Mylar film mask for various gaps, velocities and wedge angles. It was assumed that the membrane deflections were caused by pressure created on the mask as predicted by Reynolds hydrodynamic lubrication theory.

Chapter 5: Experiments and Results

5.1 Bulge Tests

Tension in the membrane was determined from a differential pressure versus out of plane bulge test. The test setup is described in Chapter Four.

Solving the elastic equation, equation (1) for tension produces a simplified version, equation (2). $w = \frac{P}{4T}(R^2 - r^2)$ (See appendix B.1 for this derivation)

This equation was solved for the known pressures and deflections obtained from the optical displacement measurement sensor. the results are calculated and displayed in Table 3.

Table 3: Tension values for given pressure, and measured deflections

Pressure (kgf/m^2)	volts (volts)	difference (volts)	deflection (meters)	radius (m)	Tension (kgf/m)
0	4.47	0	0	0.0275	
1.36	4.08	0.38	7.58E-05	0.0275	3.39
2.72	3.82	0.65	12.59E-05	0.0275	4.08
4.08	3.61	0.86	16.89E-05	0.0275	4.56
5.44	3.28	1.19	23.31E-05	0.0275	4.41
6.79	2.93	1.55	30.16E-05	0.0275	4.26
8.16	2.78	1.69	33.02E-05	0.0275	4.67
9.52	2.60	1.86	36.41E-05	0.0275	4.94
10.88	2.31	2.17	42.31E-05	0.0275	4.86
12.24	2.15	2.32	45.27E-05	0.0275	5.11
13.60	1.99	2.48	48.49E-05	0.0275	5.30

Using FEMLAB, these results for pressure and tension were substituted in and deflections were obtained and are shown in Table 4.

Table 4: Deflection and pressure calculations derived from FEMLAB

pressure (kgf/m^2)	deflection (meters)
1.36	7.58E-05
2.72	12.59E-05
4.08	16.90E-05
5.44	23.30E-05
6.79	30.20E-05
8.16	33.00E-05
9.52	36.40E-05
10.88	42.30E-05
12.24	45.20E-05
13.60	48.50E-05

These results for the FEMLAB data are almost identical to the results obtained for the experimental set up.

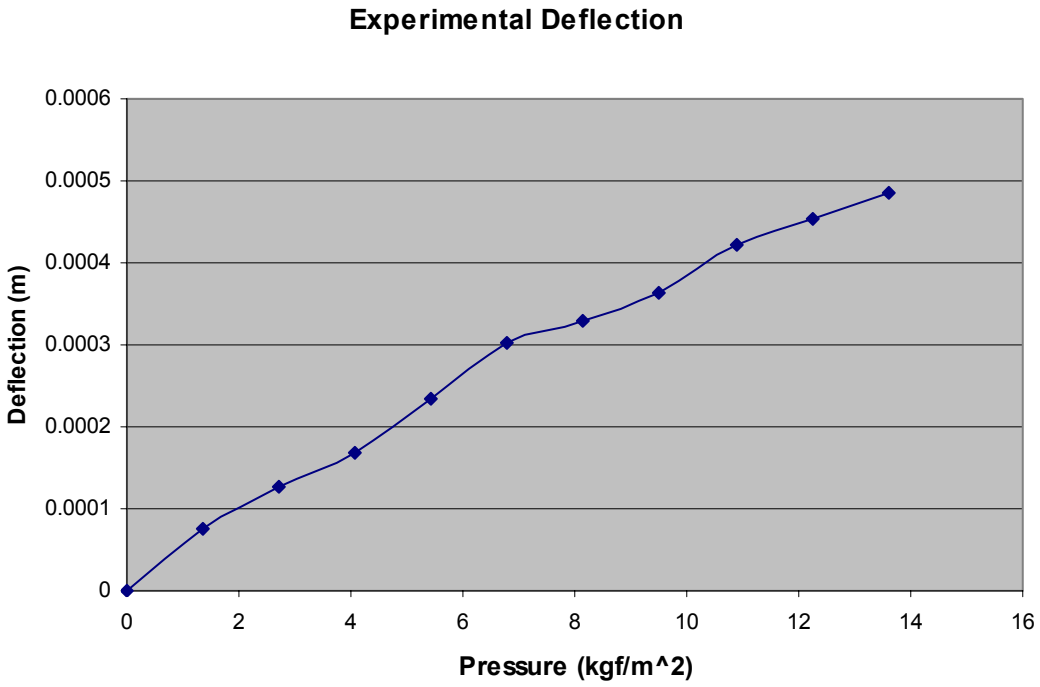

Figure 28: Deflection vs. pressure graph for experimental data

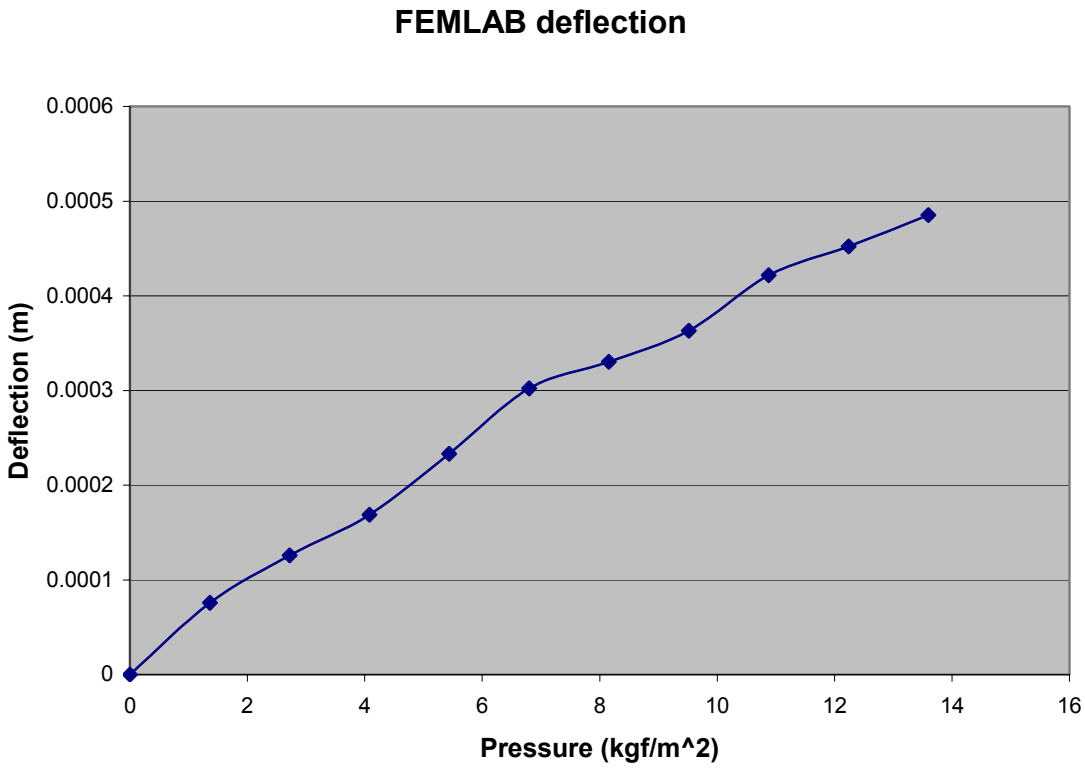

Figure 29: Deflection vs. pressure graph for FEMLAB data

This suggests that the FEMLAB model accurately represents the real life experiment. This suggests that it will be reasonable to couple the pressure equation with Reynolds equation using FEMLAB to get theoretical results for the aeroelasticity rig.

5.2 Typical Results

All of the data from the different tests were captured and initially analyzed using the WINDAQ software on the DATAQ data acquisition system. The data was displayed as change in voltage over a period of time. The output of the timing system is shown in Figure 30.

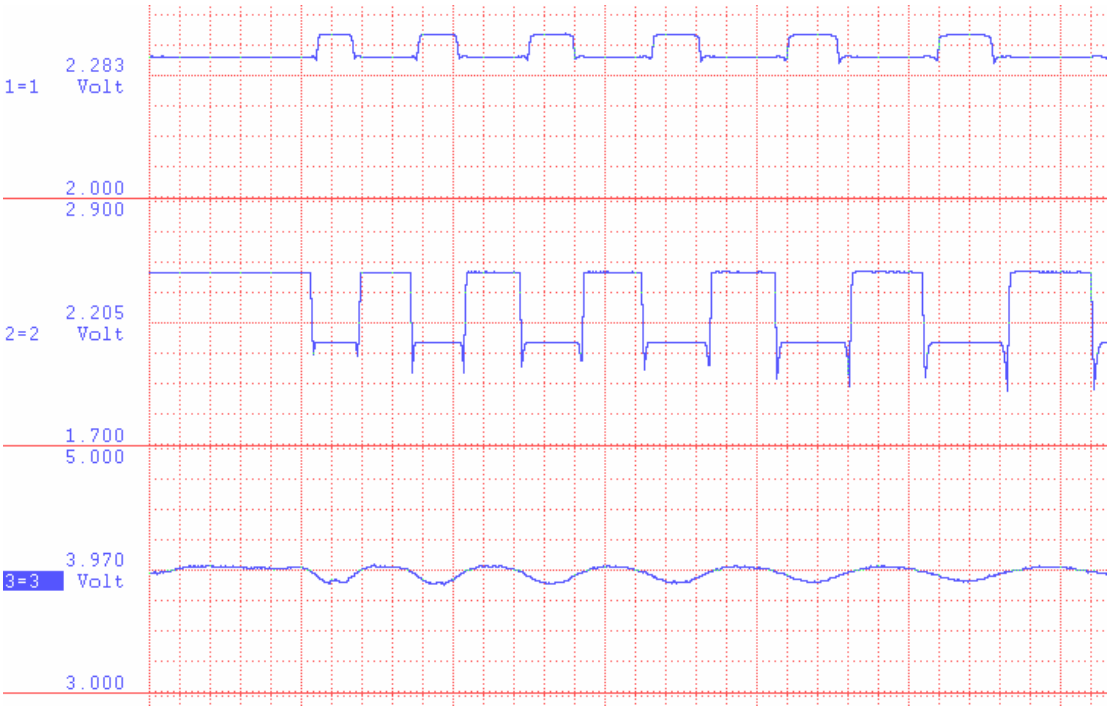

Figure 30: Screen shot of computer taking measurements. The top two channels of the program shows the IR timing pulses, with measurements between the drop in channel 1 and the rise in channel 2 denoting the time it takes for the block to move from one timing gate to the next. The bottom channel 3 is a voltage change from the optical displacement sensor. Software allows for direct measurement of the vertical and horizontal lines.

The optical sensor records the deflection at set positions of the Mylar film mask for various gaps, velocities and wedge angles. These deflections are assumed to be due to the pressure created on the mask. This pressure is calculated with basic lubrication theory using 2D Reynolds equation.

The block starts out moving to the left with a speed of 20 cm/sec. The causes the film to bulge out, represented as the first trough on the graph, Then as the block moves back to the right, the film is sucked in, represented by the first peak on the graph. The trend continues with time, the velocity decreases in the following trend; 20, 15, 12, 10 cm/sec for each consecutive set of peaks and troughs.

These measurements are obtained in the form of a time history through the DATAQ, where the voltage change is equivalent to the deflection. After applying a scale factor, a typical deflection time history appears in Figure 31.

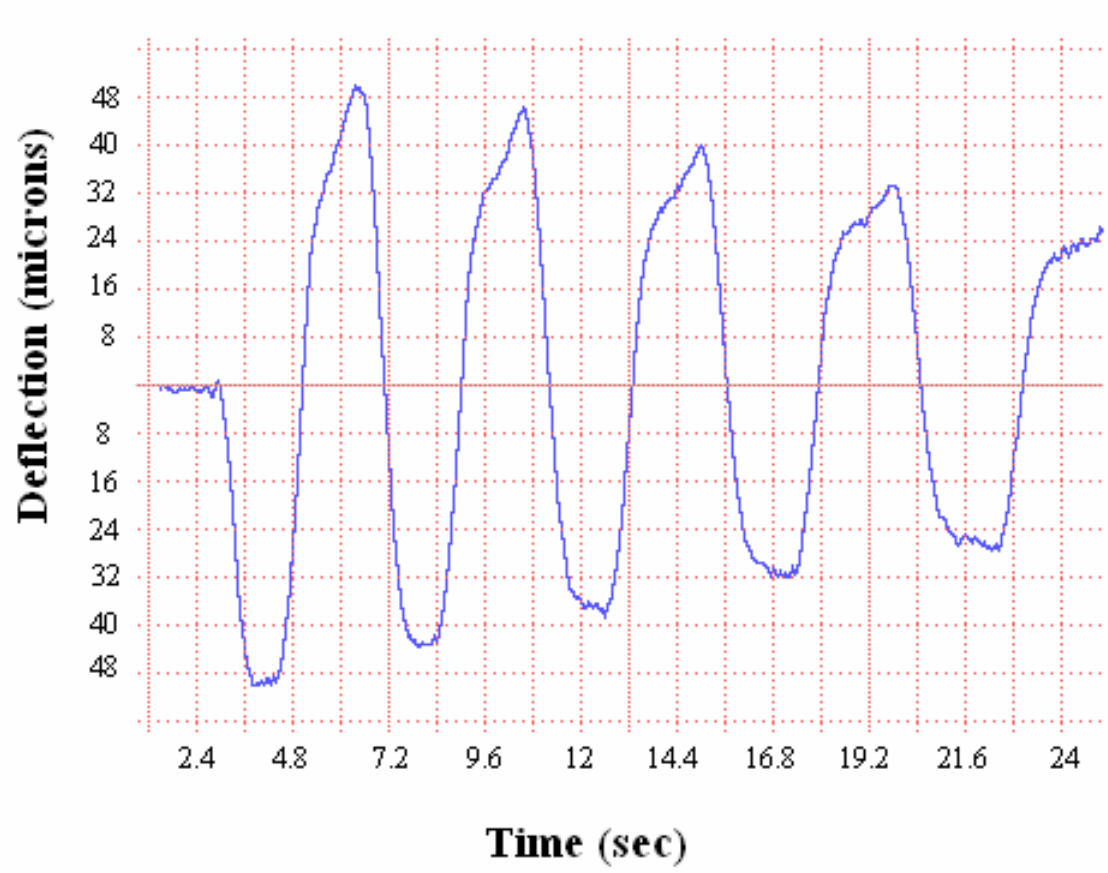

Figure 31: Typical deflection vs. time graph for the Mylar film with a small wedge angle.

5.3 Tests

5.3.1 Velocity

The velocity of the block with respect to the mask is assumed to have an effect on the deflection of the membrane. In this portion of the experimental testing, the gap and wedge angle were held constant and the velocity was varied. The wedge angle was set to 0.119 degrees with a gap of 114 microns. The mask out-of-plane deflection was recorded as the velocity was set at 20, 15, 12, 10 cm/sec respectively. As the velocity decreased, the deflection of the membrane did so as well.

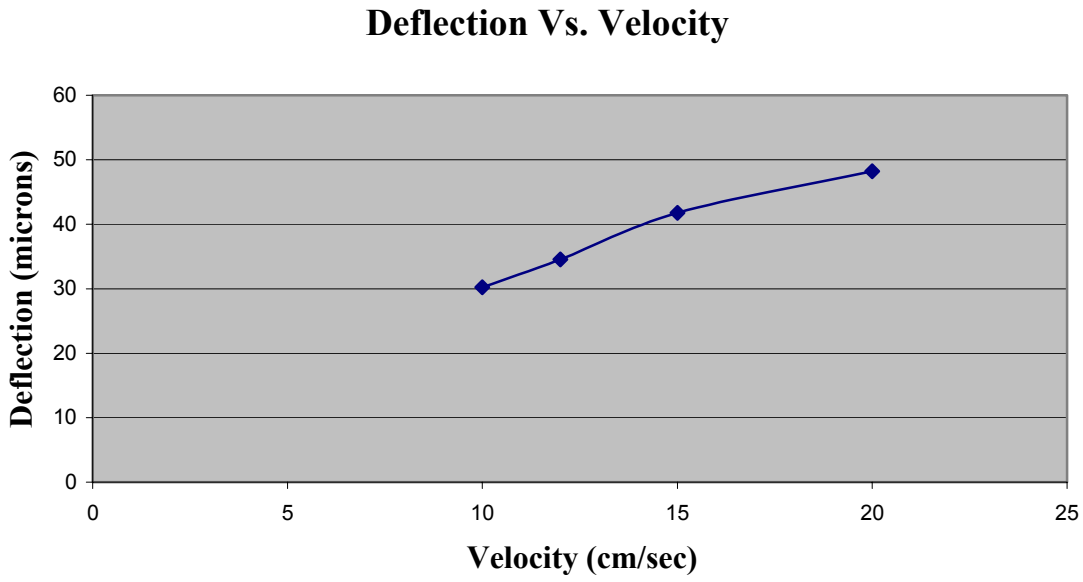

Figure 32: Membrane deflection vs. velocity for constant wedge angle and gap.

5.3.2 Wedge Angle

A key theoretical prediction is that wedge angle has a strong effect on membrane deflection while stepping at gap. A wedge angle of zero degrees is predicted to produce zero deflection. It is also predicted that as the wedge angle increases for a constant gap and speed, the deflection will also increase. Negative wedge angles should produce negative deflections.

Shown below in Figure 33 are the time histories of deflection versus time for varying wedge angles with a constant and gap of 114 microns. Figure 34 shows typical wedge angle versus deflection data.

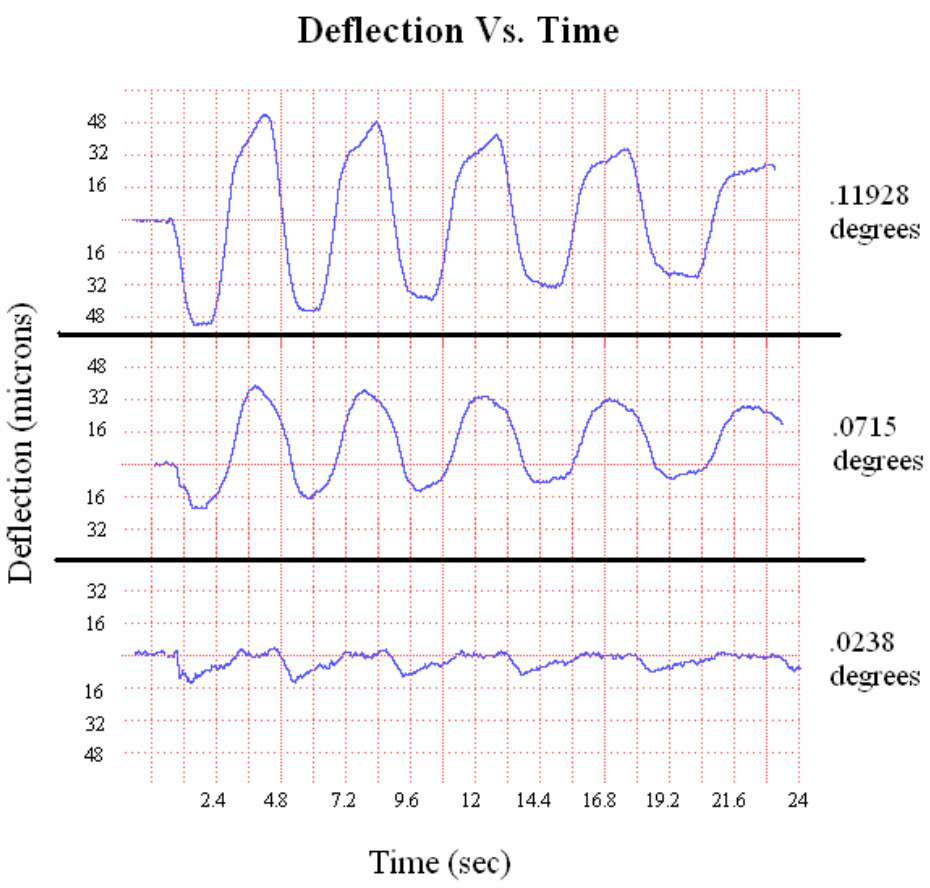

Figure 33: Time histories for deflection as the velocity is decreasing from left to right.

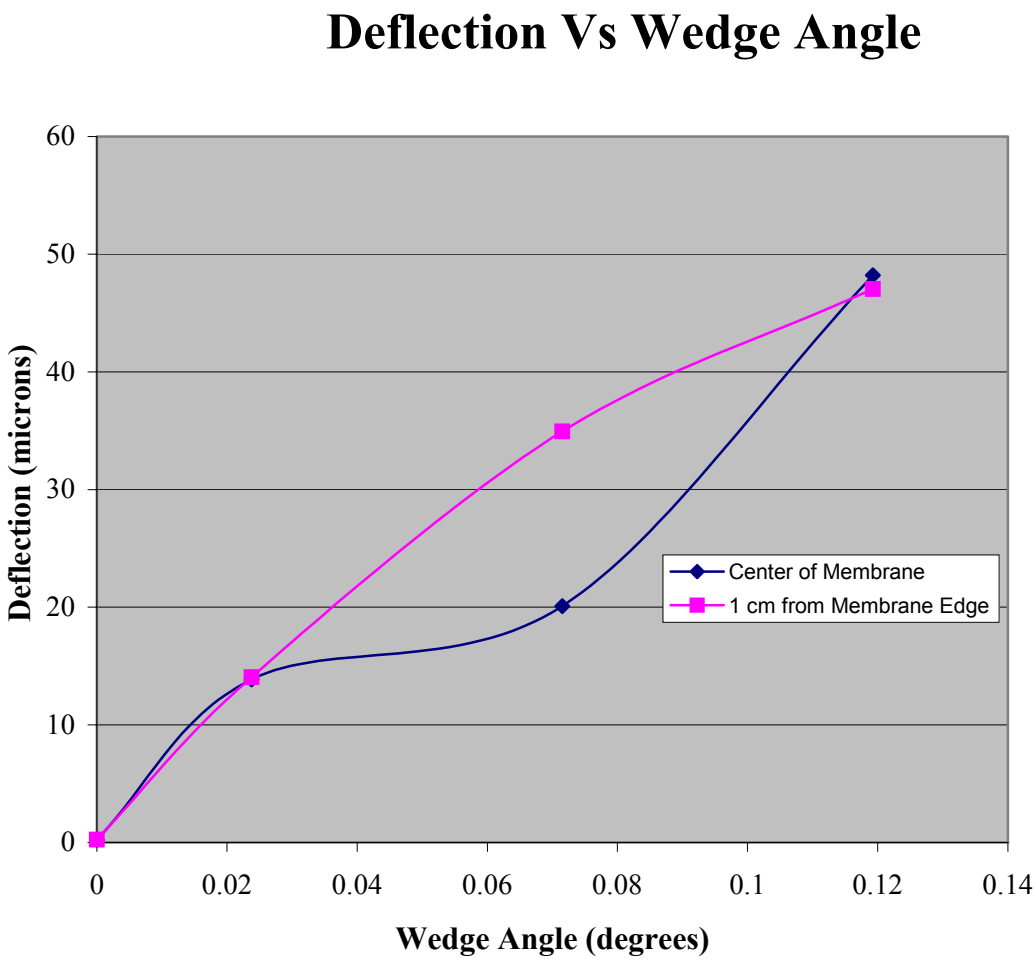

Figure 34: Deflection vs. wedge angle

5.3.3 Shape of Deflected Membrane

The shape of the deflected membrane is predicted to be asymmetric with a larger deflection on the leading edge side. Measurements were taken across the membrane at multiple points in an effort to estimate the deflected shaped of the membrane.

Comparing the max deflections of the Mylar film at various positions, at the same velocity, wedge angle and gap will show that the mid-span deflection is asymmetric. The position across the membrane is shown in Figure 35.

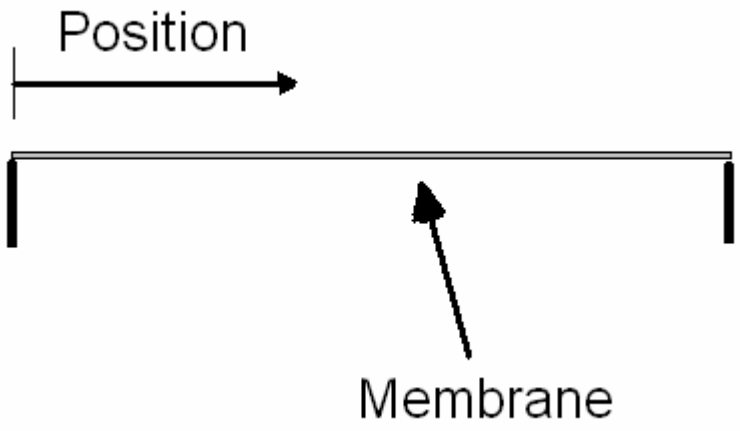

Figure 35: Position measurement across the membrane.

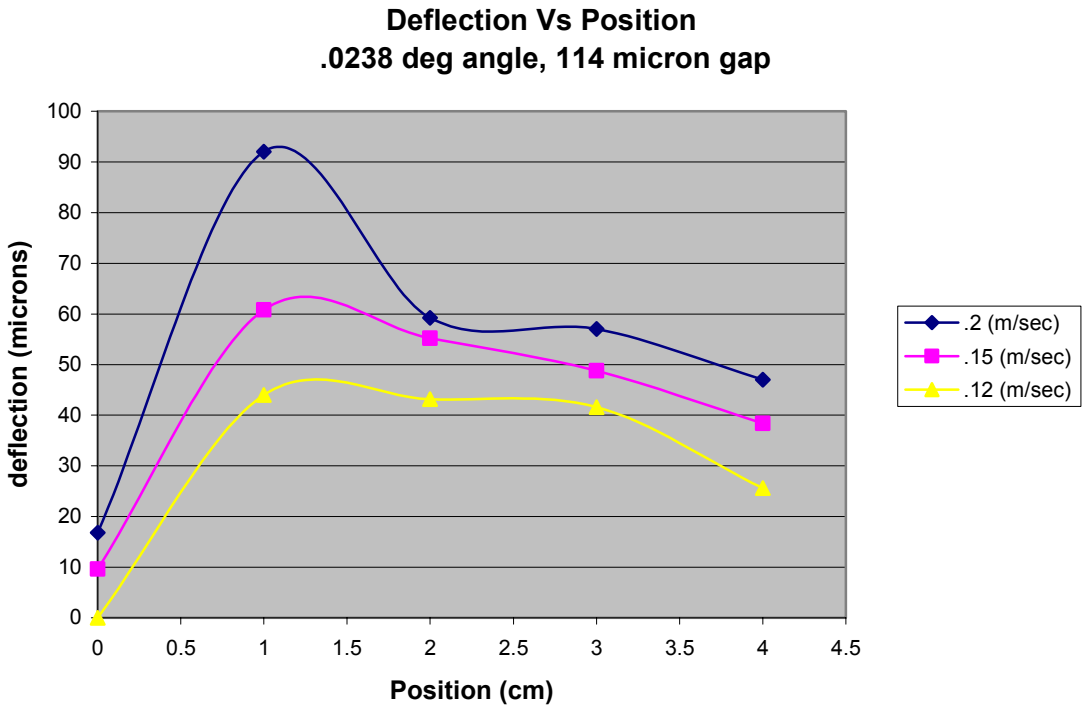

Figure 36: Deflection vs. Position

Shown in Figure 36 is the relationship between the position of the measurement sensor on the Mylar, relative to the center and the deflection of the membrane. The angle is kept constant at .0238 degrees; the gap is kept constant at 114 microns. The speed was also held constant at 20, 15, and 12 cm/sec.

As the wedge angle of the film is increased, while maintaining a constant velocity and gap it will cause more pressure to be applied to certain positions of the film, thus increasing the max deflection of the film.

5.3.4 Gap

For a constant wedge angle the deflection is predicted to vary with the gap distance. As the gap decreases, the deflection should increase, in a nonlinear fashion, which is roughly an inverse cubic relation

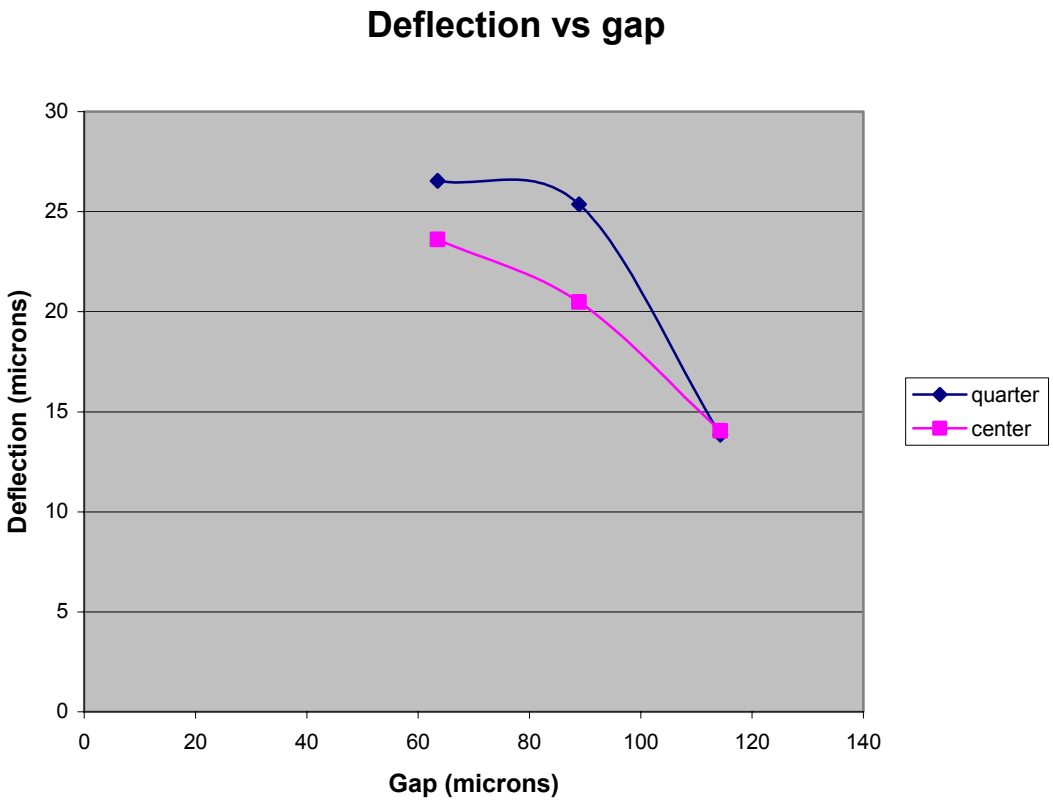

Figure 37: Deflection vs. gap for a constant wedge angle

Figure 37 summarizes the results from a series of experiments. The wedge angle was set to a constant 0.0238 degrees and the gap was varied from 63.5, 88.9 and

114.3. The velocity was held constant at 20 cm/sec. The data labeled "center" was measured at the center of the membrane. The data labeled "Quarter" was measured 1cm off from the center of the membrane.

5.3.5 Infinitely Long

In this portion of the experiment a long thin rectangular Mylar mask is tested. The mask has a span (L) normal to the direction of motion that is ten times the chord length (B) that is in the direction of motion. Figure 38 shows the geometry. Figure 39 is a picture of the elongated membrane.

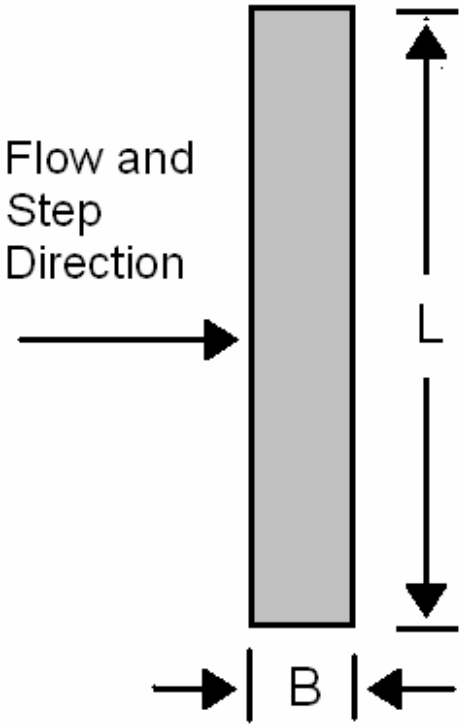

Figure 38: Geometry of elongated rectangle

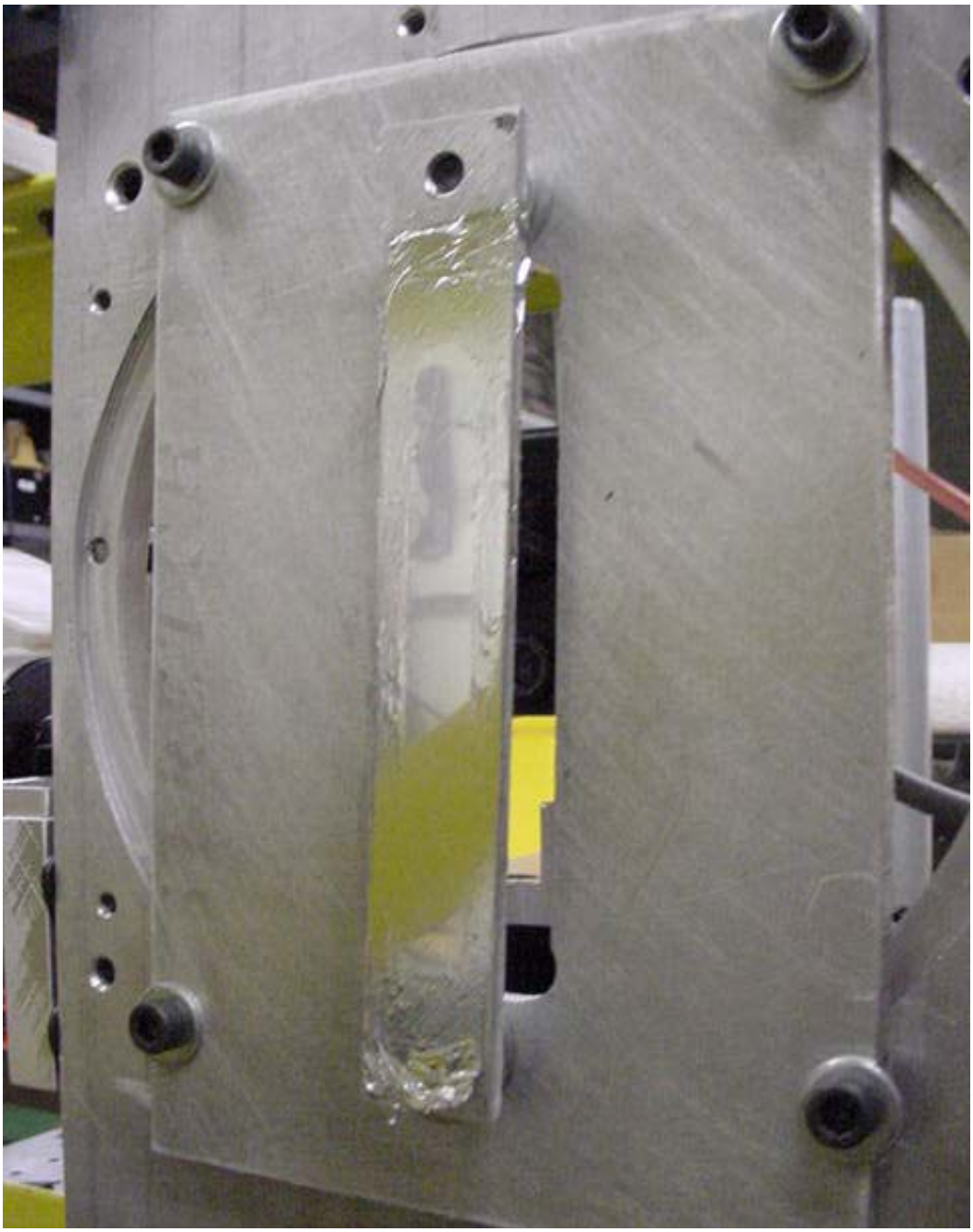

Figure 39: Rectangular membrane, ten to one geometry.

The idea behind this test was to simulate an infinitely long membrane with 1-D mechanics. The first term of Reynolds equation, equation (6) considers the pressure in the x direction, which is the direction of motion of the granite block. The second term considers the pressure variation in the y direction, which is normal to the direction of motion. When dealing with this infinitely long geometry, gradients with respect to the y-direction vanish and Reynolds equation simplifies to a 1-D form. Equation (18)

$$\frac{d}{dx}(h^3 \frac{dp}{dx}) = 6U\eta \frac{dh}{dx} \quad \textbf{(18)}$$

After one integration this then becomes equation (19), where C is a constant of integration.

$$h^3 \frac{dp}{dx} = 6U\eta h + C \quad \textbf{(19)}$$

It is known that $\frac{dp}{dx}$ is equal to zero at some point. It is assumed that this occurs at a single point and corresponds to a maximum (or minimum) pressure. When this occurs we find that C = $-6U\eta\bar{h}$, where $\bar{h}$ is the thickness of the film. Using this constant of integration equation (19) can be rearranged to form equation (20).

$$\frac{dp}{dx} = 6U\eta \frac{h - \bar{h}}{h^3} \quad \textbf{(20)}$$

The gap, velocity and wedge angle were held constant, as the deflection was measured at different positions in the x direction across the entire width of the Mylar mask at the center position of the length. Figure 40 is a picture of the optical sensor positioned for the rectangular geometry.

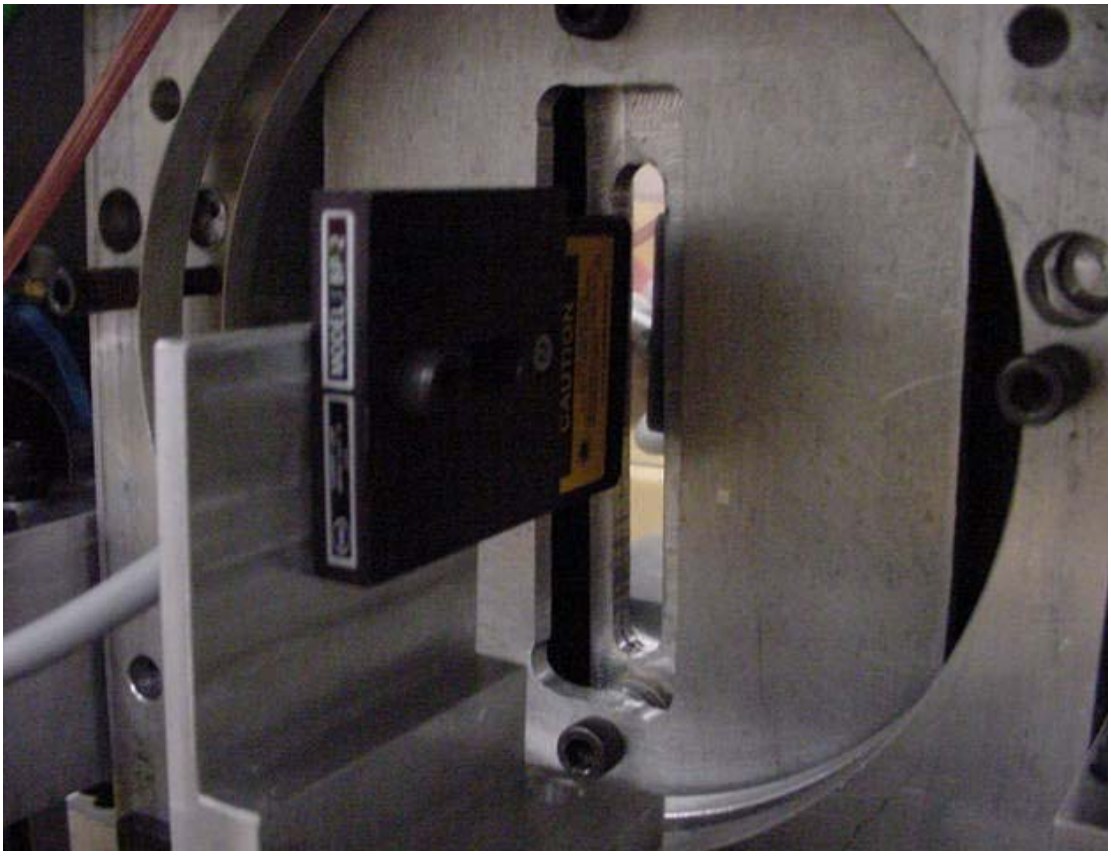

Figure 40: Optical displacement sensor positioned at the center of the rectangle membrane. The sensor is stage mounted to move horizontally to obtain deflection measurements at various positions across the surface in the x direction

The optical displacement measurement system was moved linearly in the x-direction across the width of the rectangular membrane on a mechanical stage. For each of these positions the out-of-plane deflection was measured and recorded. The deflection vs. position graph is shown below in Figure 41.

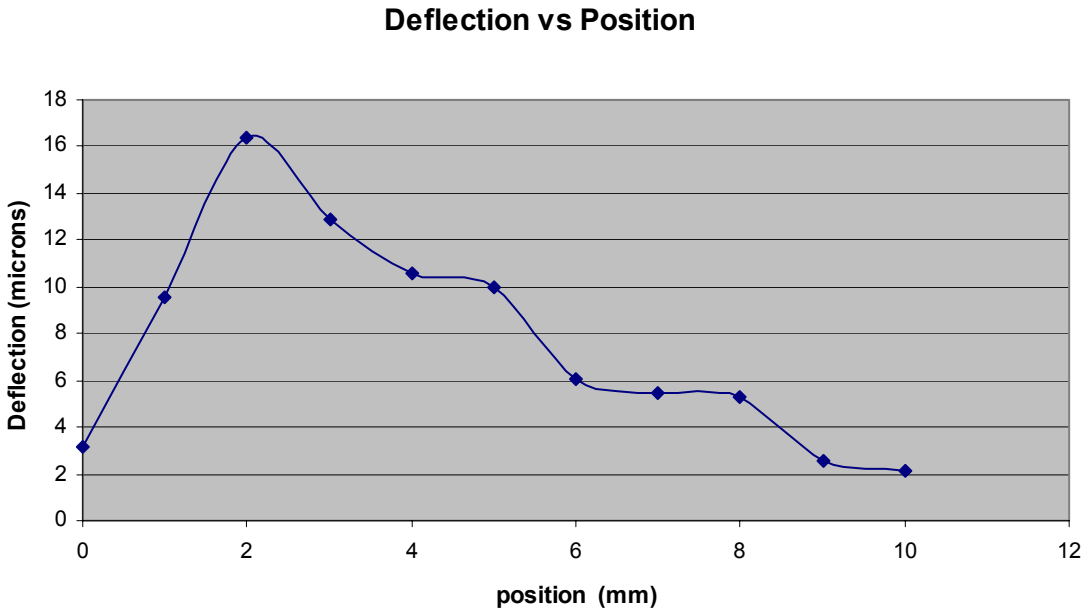

Figure 41: Deflection vs. position data for the rectangular membrane.

The maximum deflection is shifted to the left of the mask, i.e. the leading edge, in the direction of the moving granite block. This is also the edge of the mask that is angled in closer to the block.

Chapter 6: Discussion and Conclusion

6.1 Conclusion

The main goal behind this research was to study the aeroelastic mechanics of thin film membranes by experimental tests and then to simulate these tests by creating a theoretical model in FEMLAB. Once these models were created they could be used to predict the behavior of the thin film membranes for various gaps, wedge angles, and velocities.

In the application of proximity lithography it would be greatly beneficial to be able to model these experiments in FEMLAB first before actually performing them. This would allow for the ideal settings to be determined for the manufacturing process.

After comparing the experimental results to the FEMLAB Results, it can be shown that FEMLAB will be a very useful tool in predicting the behavior of thin film membranes in real life situations.

Based on user input values for the gap distance of the mask wafer relative to the wafer, the maximum deflection can be calculated. Also the location of this maximum deflection can also be predicted.

Shown in Figure 42 are the FEMLAB values of deflection for various velocities, and the experimental data for the deflection at the same velocities.

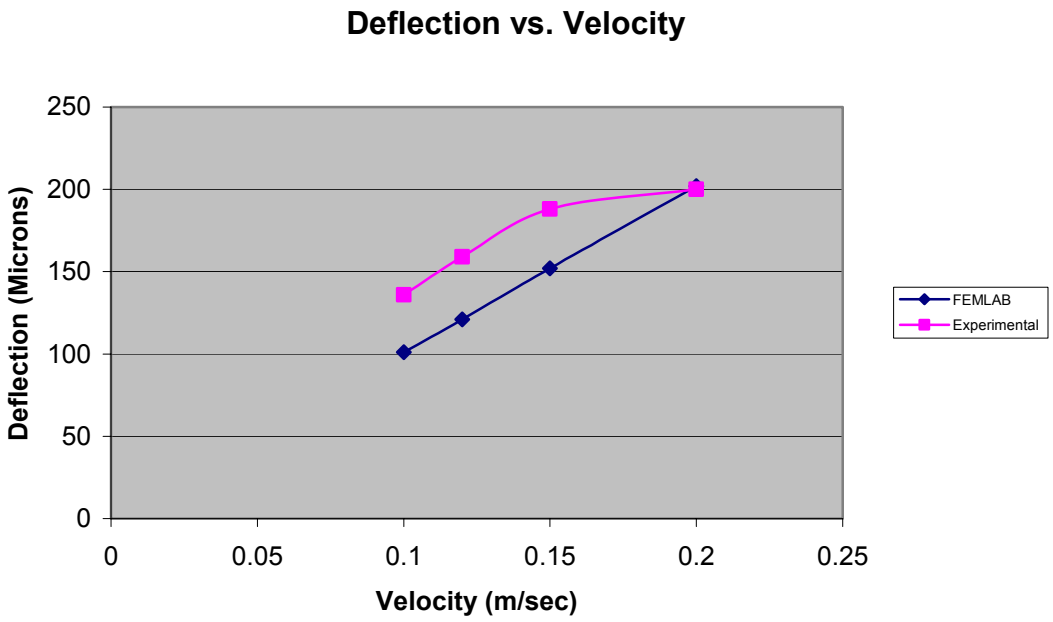

Figure 42: Deflection vs. Velocity for FEMLAB, and experimental data.

Shown in Figure 43 is the FEMLAB, experimental and hand calculations for the deflection of the membrane, w(x) at various positions across the infinitely long (10:1) rectangular geometry.

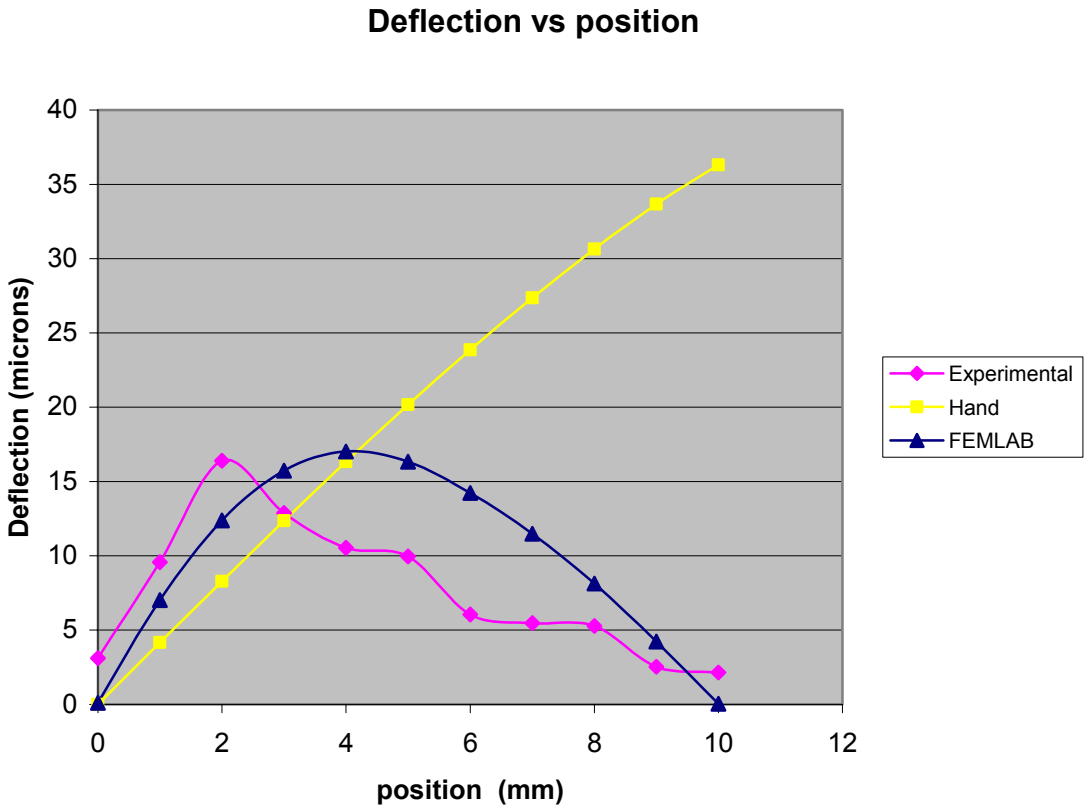

Figure 43: Position vs. Velocity for FEMLAB, hand calculations and experimental data.

6.2 Limitations

From all of the data gathered from FEMLAB and data from the aeroelasticity rig it is shown that the FEMLAB model accurately predicts the outcome of the experimental test. It appears that the largest source of inaccuracy at this point is the positioning of the mask relative to the granite block. Currently the placement of the mask is only as accurate as the dial gauges, which is nominally 1 μm, but is probably larger due to hysteresis and mounting effects.

6.3 Possible Future Research Directions

A next step in this research would be to get three more of the optical displacement sensors to replace the three dial gauges for gap metrology. This would allow for much more accurate positioning of the mask relative to the granite block and more precise measurements of the gap and wedge angles

Once the new measurement sensors are in place, the next step would be to repeat the testing for an actual mask. First a new model would need to be created using FEMLAB. Various wedge angles, velocities, and positioning would be input into the program for each new test, to get the predicted deflection and pressure. Then for each of the FEMLAB simulations, experimental tests will be preformed using the aeroelasticity rig with the same wedge angles, velocities and positioning.

Appendices

A.1 Reynolds Equation

Dimension: circle (radius .0275 m)

Boundary condition: fixed

Reynolds Equation: $$\frac{\partial}{\partial x}\left((h)^3\frac{\partial p}{\partial x}\right)+\frac{\partial}{\partial y}\left((h)^3\frac{\partial p}{\partial y}\right)=6U\eta\frac{d(h)}{dx}$$

FEMLAB Constants for circular geometry

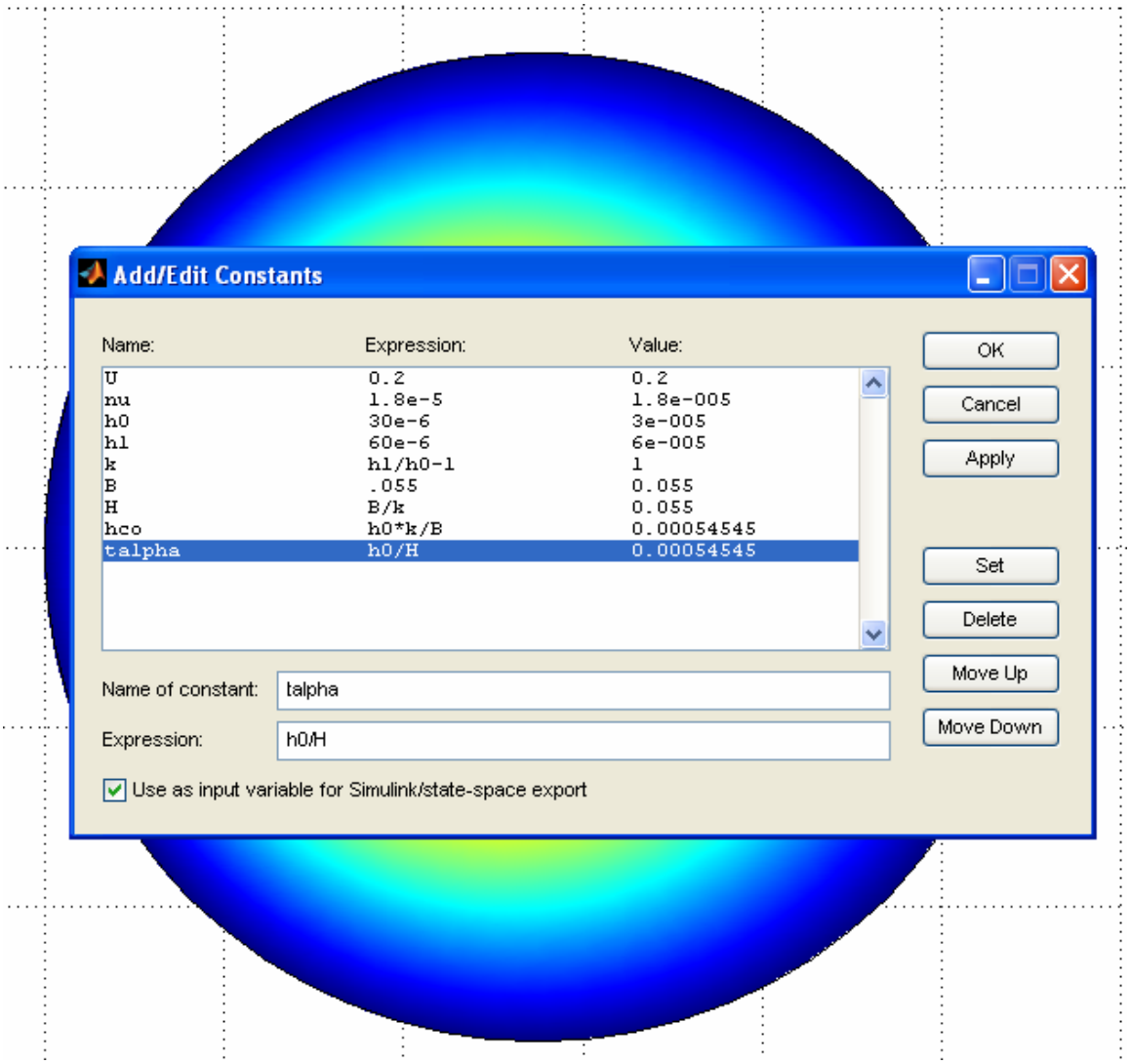

Subdomain settings for Reynolds equation for circular geometry in FEMLAB

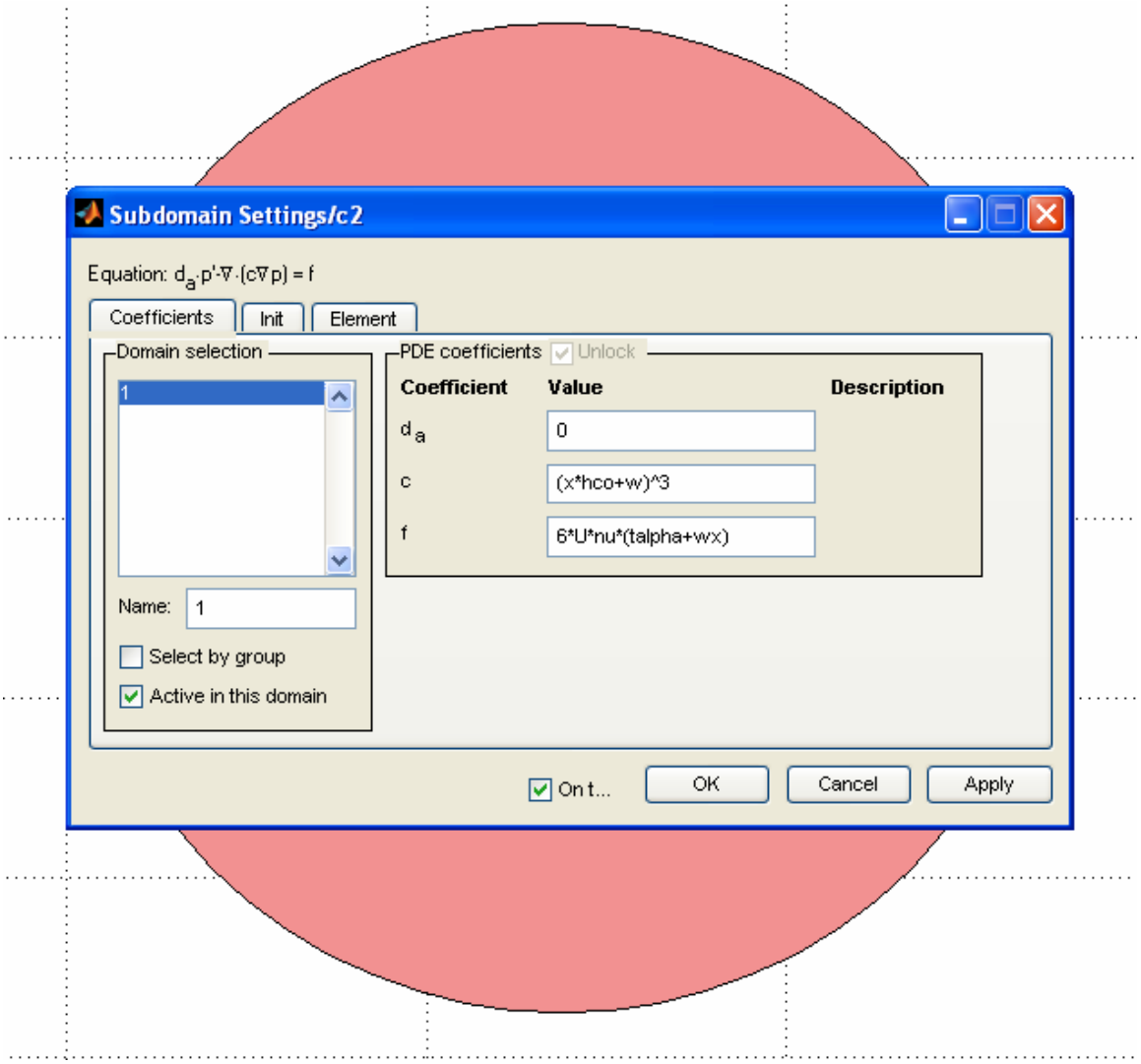

Meshed:

Mesh of the circular geometry

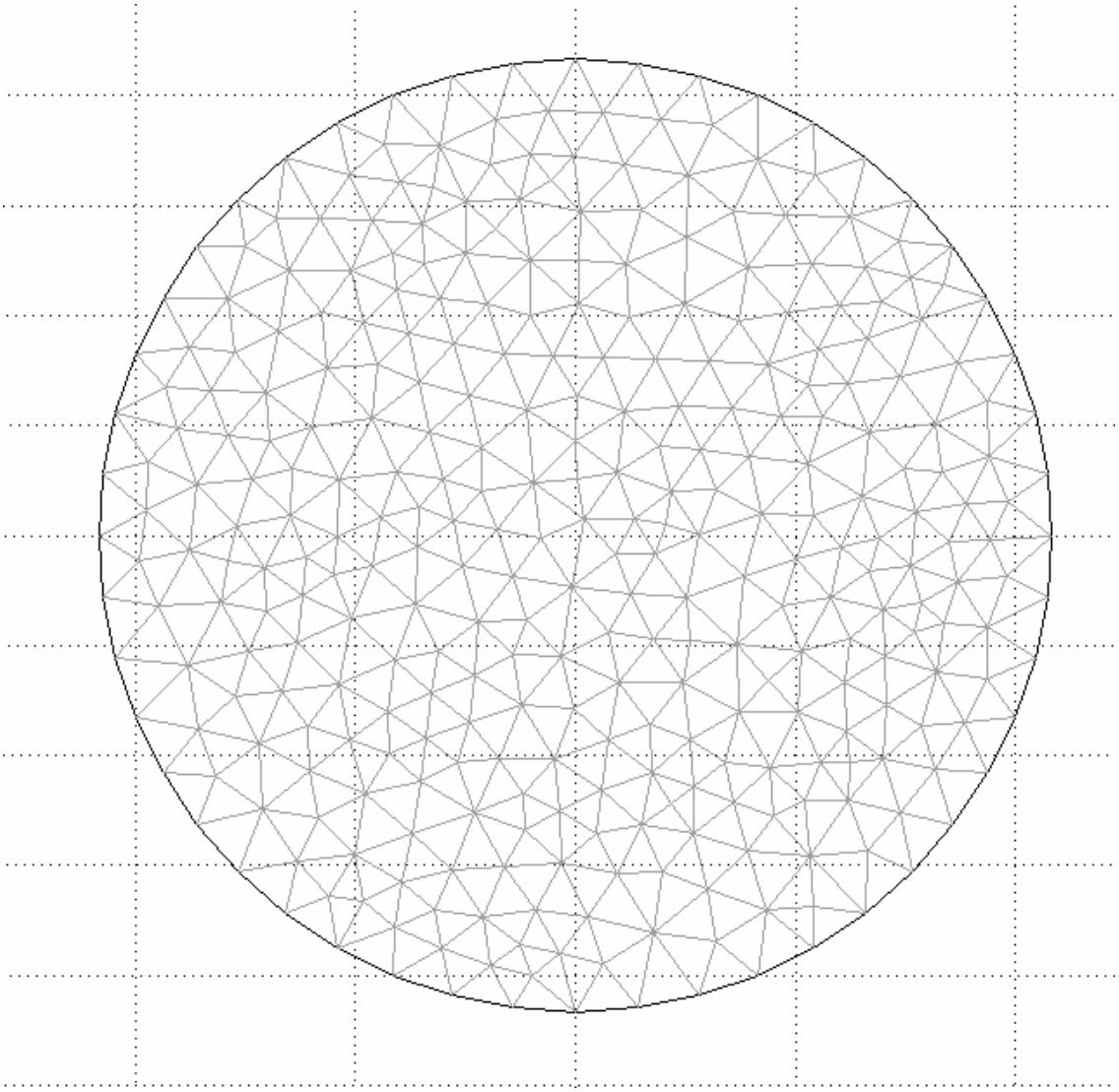

Results (deflection)

Three-dimensional plot for the deflection of the circular geometry

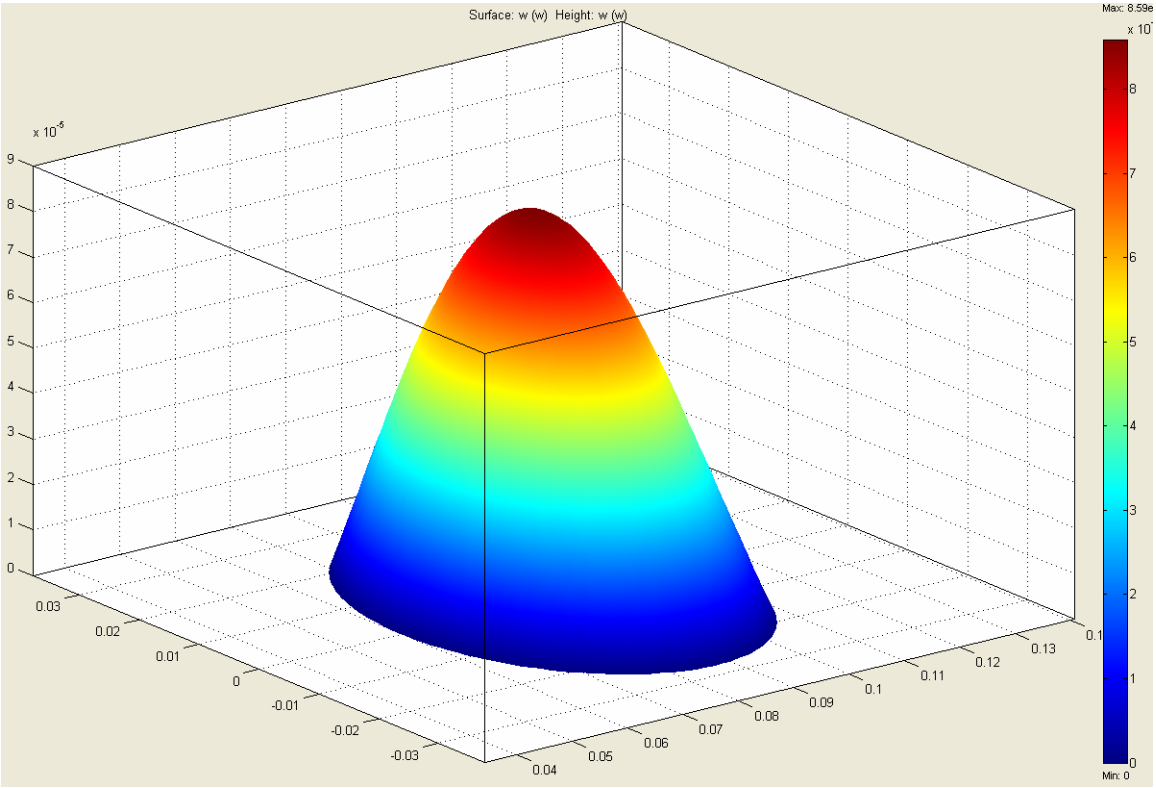

Pressure Equation

$$p(x,y) = -T\nabla^2 w(x,y)$$

Coefficients for the pressure equation

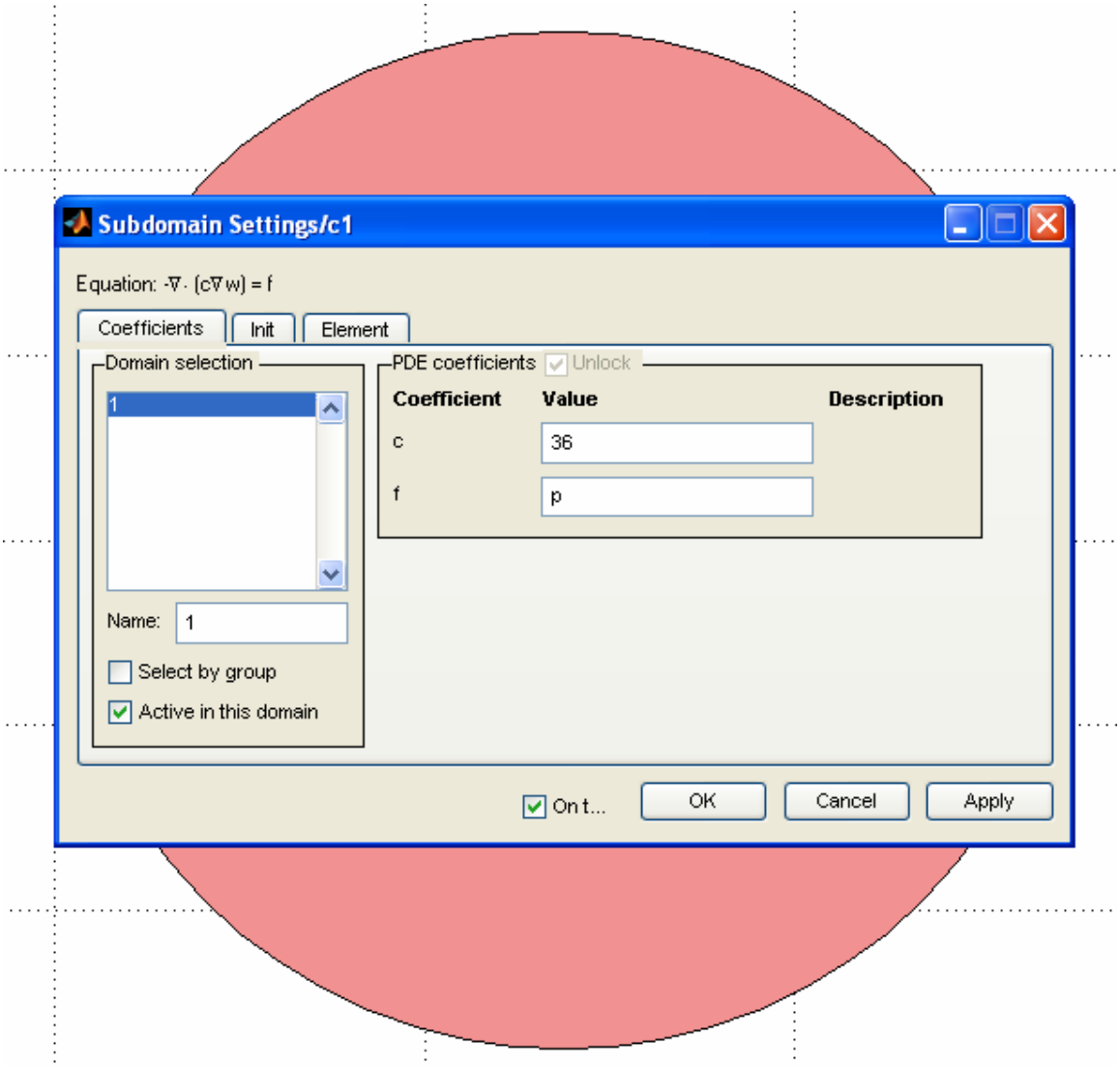

Results (for a known tension and pressure)

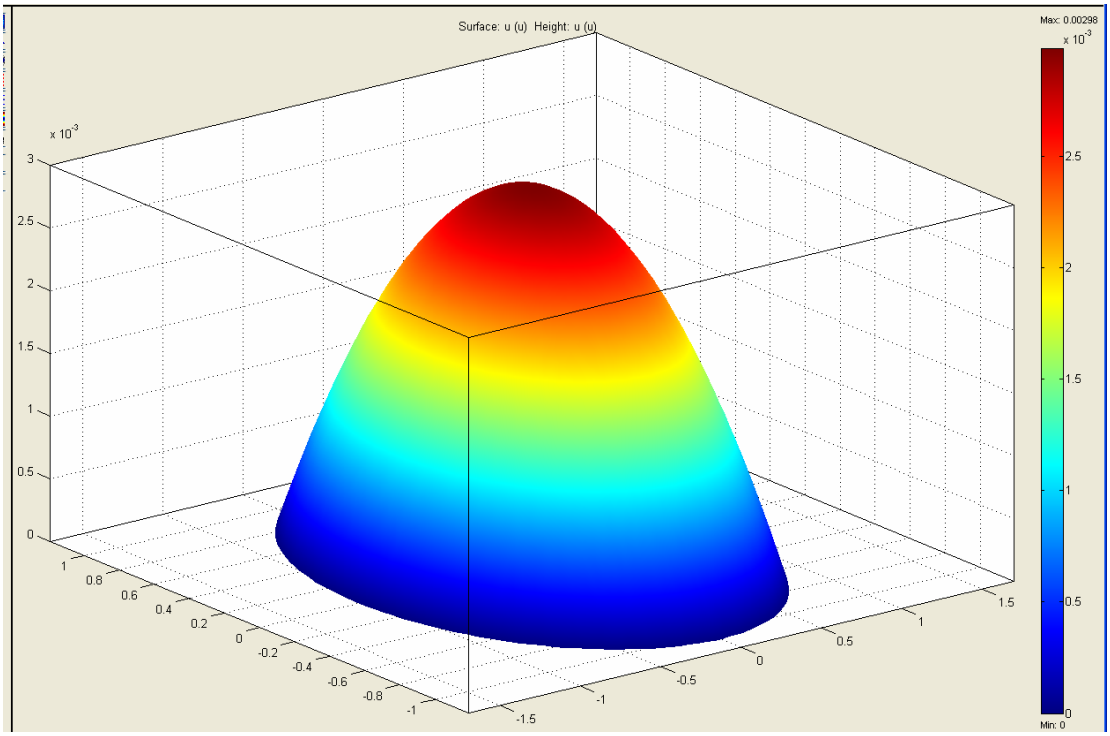

A.2 Matlab Code

```
% FEMLAB Model M-file
% Generated 08-Jul-2005 16:20:51 by FEMLAB 2.3.0.145.

flclear xfem
% FEMLAB Version
clear vrsn;
vrsn.name='FEMLAB 2.3';
vrsn.major=0;
vrsn.build=145;
xfem.version=vrsn;

% Recorded command sequence

% New geometry 1
xfem.fem{1}.sdim={'x','y'};
fem=xfem.fem{1};

% Geometry
clear s c p
R1=rect2(0.19999999999999996,0.24999999999999994,-0.025000000000000022, ...
0.024999999999999981,0);
objs={R1};
names={'R1'};
s.objs=objs;
s.name=names;

objs={};
names={};
c.objs=objs;
c.name=names;

objs={};
names={};
p.objs=objs;
p.name=names;

drawstruct=struct('s',s,'c',c,'p',p);
fem.draw=drawstruct;
fem.geom=geomcsg(fem);
```

```
clear appl

% Application mode 1
appl{1}.mode=flpoisson2d('dim',{'u','u_t'},'sdim',{'x','y'},'submode','std', ...
'tdiff','on');
appl{1}.dim={'u','u_t'};
appl{1}.form='coefficient';
appl{1}.border='off';
appl{1}.name='c1';
appl{1}.var={};
appl{1}.assign={'abscu1x';'abscu1x';'absga1x';'absga1x';'absux';'absux'};
appl{1}.elemdefault='Lag2';
appl{1}.shape={'shlag(2,"u")'};
appl{1}.sshape=2;
appl{1}.equ.c={{{'1'}}};
appl{1}.equ.f={{{'1'}}};
appl{1}.equ.gporder={{4}};
appl{1}.equ.cporder={{2}};
appl{1}.equ.shape={1};
appl{1}.equ.init={{{'0'}}};
appl{1}.equ.usage={1};
appl{1}.equ.ind=1;
appl{1}.bnd.q={{{'0'}}};
appl{1}.bnd.g={{{'0'}}};
appl{1}.bnd.h={{{'1'}}};
appl{1}.bnd.r={{{'0'}}};
appl{1}.bnd.type={'dir'};
appl{1}.bnd.gporder={{0}};
appl{1}.bnd.cporder={{0}};
appl{1}.bnd.shape={0};
appl{1}.bnd.ind=ones(1,4);

fem.appl=appl;

% Initialize mesh
fem.mesh=meshinit(fem,...
        'Out',    {'mesh'},...
        'jiggle', 'mean',...
        'Hcurve', 0.29999999999999999,...
        'Hgrad',  1.3,...
        'Hpnt',   {10,[]});

% Differentiation rules
xfem.rules={};
```

```
% Problem form
fem.outform='coefficient';

% Differentiation simplification
fem.simplify='on';

% Boundary conditions
clear bnd
bnd.q={{{'0'}}};
bnd.g={{{'0'}}};
bnd.h={{{'1'}}};
bnd.r={{{'0'}}};
bnd.type={'dir'};
bnd.gporder={{0}};
bnd.cporder={{0}};
bnd.shape={0};
bnd.ind=ones(1,4);
fem.appl{1}.bnd=bnd;

% PDE coefficients
clear equ
equ.c={{{'(x*hco)^3'}}};
equ.f={{{'6*U*nu*talpha'}}};
equ.gporder={{4}};
equ.cporder={{2}};
equ.shape={1};
equ.init={{{'0'}}};
equ.usage={1};
equ.ind=1;
fem.appl{1}.equ=equ;

% Internal borders
fem.appl{1}.border='off';

% Shape functions
fem.appl{1}.shape={'shlag(2,"u")'};

% Geometry element order
fem.appl{1}.sshape=2;

% Define constants
xfem.const={...
        'U',      0.10000000000000001,...
```

```
        'nu',     1.8e-005,...
        'h0',     4.0000000000000003e-005,...
        'h1',     5.0000000000000002e-005,...
        'k',      0.25,...
        'B',      0.050000000000000003,...
        'H',      0.20000000000000001,...
        'hco',    0.00020000000000000001,...
        'talpha', 0.00020000000000000001};
xfem.fem{1}=fem;

% Multiphysics
xfem=multiphysics(xfem);

% Extend the mesh
xfem.xmesh=meshextend(xfem,'context','local','cplbndeq','on','cplbndsh','on');

% Evaluate initial condition
init=asseminit(xfem,...
        'context','local',...
        'init',   xfem.xmesh.eleminit);

% Solve problem
xfem.sol=femlin(xfem,...
        'jacobian','equ',...
        'out',    {'sol'},...
        'init',   init,...
        'context','local',...
        'sd',     'off',...
        'nullfun','flnullorth',...
        'blocksize',5000,...
        'solcomp',{'u'},...
        'linsolver','matlab',...
        'method', 'eliminate',...
        'uscale', 'auto');

% Save current fem structure for restart purposes
xfem0=xfem;

% Plot solution
postplot(xfem,...
        'geomnum',1,...
        'context','local',...
        'tridata',{'u','cont','internal'},...
        'trifacestyle','interp',...
```

```
        'triedgestyle','none',...
        'trimap', 'jet',...
        'trimaxmin','off',...
        'tribar', 'on',...
        'geom',   'on',...
        'geomcol','bginv',...
        'refine', 3,...
        'contorder',2,...
        'phase',  0,...
        'title',  'Surface: u (u)  ',...
        'renderer','zbuffer',...
        'solnum', 1,...
        'axisvisible','on')

% Plot solution
postplot(xfem,...
        'geomnum',1,...
        'context','local',...
        'tridata',{'u','cont','internal'},...
        'trifacestyle','interp',...
        'triedgestyle','none',...
        'trimap', 'jet',...
        'trimaxmin','off',...
        'tribar', 'on',...
        'triz',   {'u','cont','internal'},...
        'refine', 3,...
        'contorder',2,...
        'phase',  0,...
        'title',  'Surface: u (u)  Height: u (u)  ',...
        'renderer','zbuffer',...
        'solnum', 1,...
        'axisvisible','on')
```

A.3 Excel Data

Table A1: Deflection of the membrane at every millimeter across one centimeter width at the middle of the height of the rectangle. Data 6/22/05 10 to 1 rectangle

	zero	low	high	low diff	high diff	low	high
0	4.341	4.325	4.363	0.016	0.022	3.121951	4.292683
1	3.314	3.265	3.446	0.049	0.132	9.560976	25.7561
2	3.58	3.496	3.672	0.084	0.092	16.39024	17.95122
3	3.607	3.541	3.754	0.066	0.147	12.87805	28.68293
4	3.583	3.529	3.751	0.054	0.168	10.53659	32.78049
5	3.855	3.804	3.873	0.051	0.018	9.95122	3.512195
6	3.713	3.682	3.728	0.031	0.015	6.04878	2.926829
7	4.004	3.976	4.043	0.028	0.039	5.463415	7.609756
8	3.999	3.972	4.025	0.027	0.026	5.268293	5.073171
9	4.177	4.164	4.219	0.013	0.042	2.536585	8.195122
10	4.307	4.296	4.329	0.011	0.022	2.146341	4.292683

Table A2: Tension Data (top is experimental, bottom FEMLAB)

Pressure (kgf/m^2)	volts (volts)	difference (volts)	deflection (meters)	radius (m)	Tension (kgf/m)
0	4.4733	0	0	0.0275	#DIV/0!
1.36	4.085	0.3883	7.57659E-05	0.0275	3.393679
2.719	3.8279	0.6454	0.000125932	0.0275	4.082061
4.079	3.6072	0.8661	0.000168995	0.0275	4.563362
5.438	3.2784	1.1949	0.000233151	0.0275	4.409678
6.798	2.9276	1.5457	0.0003016	0.0275	4.261429
8.157	2.7809	1.6924	0.000330224	0.0275	4.670106
9.517	2.6073	1.866	0.000364098	0.0275	4.941829
10.88	2.3054	2.1679	0.000423005	0.0275	4.862828
12.24	2.1532	2.3201	0.000452702	0.0275	5.111801
13.6	1.9879	2.4854	0.000484956	0.0275	5.302026
From		**Pressure**	**Deflection**		
FEMLAB		**(kgf/m^2)**	**(meters)**		
		0	0.0000758		
		1.36	0.0001259		
		2.719	0.000169		
		4.079	0.000233		
		5.438	0.000302		
		6.798	0.0000303		
		8.157	0.000364		
		9.517	0.000423		
		10.88	0.000452		
		12.24	0.000485		
		13.6			

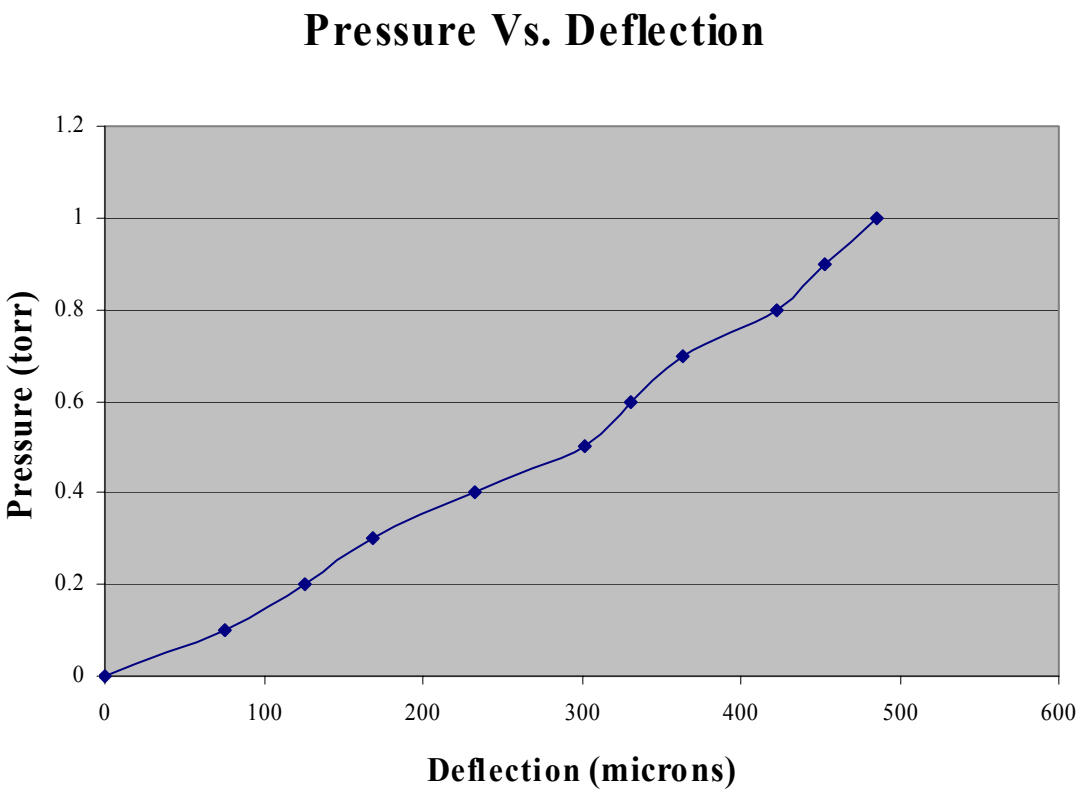

Figure A1: Graph of pressure deflection from Bulge test to determine pretension on membrane.

Table A3: Constant gap (vary the wedge angle, position, velocity)

position	angle (degrees)	gap (microns)	velocity (cm/sec)	direction (left/right)	difference (volts)	deflection (microns)
center	0.11928	114.3	20	left	0.247	48.195122
center	0.11928	114.3	15	right	0.251	48.97561
center	0.11928	114.3	15	left	0.214	41.756098
center	0.11928	114.3	14.5	right	0.235	45.853659
center	0.11928	114.3	12	left	0.177	34.536585
center	0.11928	114.3	12	right	0.199	38.829268
center	0.11928	114.3	10	left	0.155	30.243902
center	0.11928	114.3	10	right	0.17	33.170732
					0	0
R5	0.11928	114.3	20	left	0.241	47.02439
R5	0.11928	114.3	15	right	0.218	42.536585
R5	0.11928	114.3	15	left	0.212	41.365854
R5	0.11928	114.3	14.5	right	0.196	38.243902
R5	0.11928	114.3	12	left	0.191	37.268293
R5	0.11928	114.3	12	right	0.169	32.97561
R5	0.11928	114.3	10	left	0.169	32.97561
R5	0.11928	114.3	10	right	0.134	26.146341
					0	0
R10	0.11928	114.3	20	left	0.187	36.487805
R10	0.11928	114.3	15	right	0.159	31.02439
R10	0.11928	114.3	15	left	0.166	32.390244
R10	0.11928	114.3	14.5	right	0.123	24
R10	0.11928	114.3	12	left	0.143	27.902439
R10	0.11928	114.3	12	right	0.1	19.512195
R10	0.11928	114.3	10	left	0.13	25.365854
R10	0.11928	114.3	10	right	0.073	14.243902
					0	0
L5	0.11928	114.3	20	left	0.228	44.487805
L5	0.11928	114.3	15	right	0.251	48.97561
L5	0.11928	114.3	15	left	0.195	38.04878
L5	0.11928	114.3	14.5	right	0.237	46.243902
L5	0.11928	114.3	12	left	0.177	34.536585
L5	0.11928	114.3	12	right	0.222	43.317073
L5	0.11928	114.3	10	left	0.159	31.02439
L5	0.11928	114.3	10	right	0.198	38.634146
					0	0
L10	0.11928	114.3	20	left	0.183	35.707317

L10	0.11928	114.3	15	right	0.237	46.243902
L10	0.11928	114.3	15	left	0.154	30.04878
L10	0.11928	114.3	14.5	right	0.224	43.707317
L10	0.11928	114.3	12	left	0.126	24.585366
L10	0.11928	114.3	12	right	0.216	42.146341
L10	0.11928	114.3	10	left	0.103	20.097561
L10	0.11928	114.3	10	right	0.204	39.804878
					0	0
center	0.0175	114.3	20	left	0.103	20.097561
center	0.0175	114.3	20	right	0.188	36.682927
center	0.0175	114.3	15	left	0.078	15.219512
center	0.0175	114.3	15	right	0.176	34.341463
center	0.0175	114.3	12	left	0.061	11.902439
center	0.0175	114.3	12	right	0.161	31.414634
center	0.0175	114.3	10	left	0.042	8.195122
center	0.0175	114.3	10	right	0.149	29.073171
					0	0
R5	0.0175	114.3	20	left	0.179	34.926829
R5	0.0175	114.3	20	right	0.136	26.536585
R5	0.0175	114.3	15	left	0.164	32
R5	0.0175	114.3	15	right	0.12	23.414634
R5	0.0175	114.3	12	left	0.149	29.073171
R5	0.0175	114.3	12	right	0.102	19.902439
R5	0.0175	114.3	10	left	0.135	26.341463
R5	0.0175	114.3	10	right	0.083	16.195122
					0	0
R10	0.0175	114.3	20	left	0.035	6.8292683
R10	0.0175	114.3	20	right	0.122	23.804878
R10	0.0175	114.3	15	left	0.022	4.2926829
R10	0.0175	114.3	15	right	0.115	22.439024
R10	0.0175	114.3	12	left	0.007	1.3658537
R10	0.0175	114.3	12	right	0.104	20.292683
R10	0.0175	114.3	10	left	0.004	0.7804878
R10	0.0175	114.3	10	right	0.096	18.731707
					0	0
L5	0.0175	114.3	20	left	0.281	54.829268
L5	0.0175	114.3	20	right	0.144	28.097561
L5	0.0175	114.3	15	left	0.131	25.560976
L5	0.0175	114.3	15	right	0.126	24.585366
L5	0.0175	114.3	12	left	0.254	49.560976
L5	0.0175	114.3	12	right	0.109	21.268293
L5	0.0175	114.3	10	left	0.245	47.804878
L5	0.0175	114.3	10	right	0.087	16.97561

					0	0
L10	0.0175	114.3	20	left	0.226	44.097561
L10	0.0175	114.3	20	right	0.056	10.926829
L10	0.0175	114.3	15	left	0.203	39.609756
L10	0.0175	114.3	15	right	0.046	8.9756098
L10	0.0175	114.3	12	left	0.192	37.463415
L10	0.0175	114.3	12	right	0.031	6.0487805
L10	0.0175	114.3	10	left	0.178	34.731707
L10	0.0175	114.3	10	right	0.023	4.4878049
					0	0
center	0.0238	114.3	20	left	0.074	14.439024
center	0.0238	114.3	20	right	0.006	1.1707317
center	0.0238	114.3	15	left	0.069	13.463415
center	0.0238	114.3	15	right	0.002	0.3902439
center	0.0238	114.3	12	left	0.054	10.536585
center	0.0238	114.3	12	right	0.008	1.5609756
center	0.0238	114.3	10	left	0.045	8.7804878
center	0.0238	114.3	10	right	0.011	2.1463415
					0	0
R5	0.0238	114.3	20	left	0.072	14.04878
R5	0.0238	114.3	20	right	0.018	3.5121951
R5	0.0238	114.3	15	left	0.061	11.902439
R5	0.0238	114.3	15	right	0.012	2.3414634
R5	0.0238	114.3	12	left	0.052	10.146341
R5	0.0238	114.3	12	right	0.006	1.1707317
R5	0.0238	114.3	10	left	0.05	9.7560976
R5	0.0238	114.3	10	right	0.002	0.3902439
					0	0
R10	0.0238	114.3	20	left	0.059	11.512195
R10	0.0238	114.3	20	right	0.052	10.146341
R10	0.0238	114.3	15	left	0.048	9.3658537
R10	0.0238	114.3	15	right	0.037	7.2195122
R10	0.0238	114.3	12	left	0.032	6.2439024
R10	0.0238	114.3	12	right	0.033	6.4390244
R10	0.0238	114.3	10	left	0.037	7.2195122
R10	0.0238	114.3	10	right	0.029	5.6585366
					0	0
L5	0.0238	114.3	20	left	0.115	22.439024
L5	0.0238	114.3	20	right	0.061	11.902439
L5	0.0238	114.3	15	left	0.076	14.829268
L5	0.0238	114.3	15	right	0.049	9.5609756
L5	0.0238	114.3	12	left	0.055	10.731707
L5	0.0238	114.3	12	right	0.054	10.536585

L5	0.0238	114.3	10	left	0.049	9.5609756
L5	0.0238	114.3	10	right	0.049	9.5609756
					0	0
L10	0.0238	114.3	20	left	0.021	4.097561
L10	0.0238	114.3	20	right	0.052	10.146341
L10	0.0238	114.3	15	left	0.012	2.3414634
L10	0.0238	114.3	15	right	0.044	8.5853659
L10	0.0238	114.3	12	left	0	0
L10	0.0238	114.3	12	right	0.044	8.5853659
L10	0.0238	114.3	10	left	0.004	0.7804878
L10	0.0238	114.3	10	right	0.042	8.195122

Table A4: Constant wedge angle (vary the gap, position, velocity)

position	angle (degrees)	gap (microns)	velocity (cm/sec)	direction (left/right)	difference (volts)	deflection (microns)
center	0.0238	63.5	20	left	0.094	18.341463
center	0.0238	63.5	20	right	0.065	12.682927
center	0.0238	63.5	15	left	0.067	13.073171
center	0.0238	63.5	15	right	0.061	11.902439
center	0.0238	63.5	12	left	0.06	11.707317
center	0.0238	63.5	12	right	0.054	10.536585
center	0.0238	63.5	10	left	0.057	11.121951
center	0.0238	63.5	10	right	0.05	9.7560976
					0	0
R5	0.0238	63.5	20	left	0.078	15.219512
R5	0.0238	63.5	20	right	0.053	10.341463
R5	0.0238	63.5	15	left	0.071	13.853659
R5	0.0238	63.5	15	right	0.049	9.5609756
R5	0.0238	63.5	12	left	0.061	11.902439
R5	0.0238	63.5	12	right	0.044	8.5853659
R5	0.0238	63.5	10	left	0.056	10.926829
R5	0.0238	63.5	10	right	0.032	6.2439024
					0	0
R10	0.0238	63.5	20	left	0.136	26.536585
R10	0.0238	63.5	20	right	0.08	15.609756
R10	0.0238	63.5	15	left	0.121	23.609756
R10	0.0238	63.5	15	right	0.077	15.02439
R10	0.0238	63.5	12	left	0.107	20.878049
R10	0.0238	63.5	12	right	0.072	14.04878
R10	0.0238	63.5	10	left	0.103	20.097561
R10	0.0238	63.5	10	right	0.068	13.268293
					0	0
L5	0.0238	63.5	20	left	0.1	19.512195
L5	0.0238	63.5	20	right	0.07	13.658537
L5	0.0238	63.5	15	left	0.08	15.609756
L5	0.0238	63.5	15	right	0.069	13.463415
L5	0.0238	63.5	12	left	0.071	13.853659
L5	0.0238	63.5	12	right	0.077	15.02439
L5	0.0238	63.5	10	left	0.063	12.292683
L5	0.0238	63.5	10	right	0.071	13.853659
					0	0
L10	0.0238	63.5	20	left	0.094	18.341463
L10	0.0238	63.5	20	right	0.121	23.609756

L10	0.0238	63.5	15	left	0.04	7.804878
L10	0.0238	63.5	15	right	0.117	22.829268
L10	0.0238	63.5	12	left	0.033	6.4390244
L10	0.0238	63.5	12	right	0.111	21.658537
L10	0.0238	63.5	10	left	0.031	6.0487805
L10	0.0238	63.5	10	right	0.106	20.682927
					0	0
center	0.0238	88.9	20	left	0.13	25.365854
center	0.0238	88.9	20	right	0.079	15.414634
center	0.0238	88.9	15	left	0.124	24.195122
center	0.0238	88.9	15	right	0.079	15.414634
center	0.0238	88.9	12	left	0.118	23.02439
center	0.0238	88.9	12	right	0.075	14.634146
center	0.0238	88.9	10	left	0.106	20.682927
center	0.0238	88.9	10	right	0.072	14.04878
					0	0
R5	0.0238	88.9	20	left	0.105	20.487805
R5	0.0238	88.9	20	right	0.031	6.0487805
R5	0.0238	88.9	15	left	0.061	11.902439
R5	0.0238	88.9	15	right	0.01	1.9512195
R5	0.0238	88.9	12	left	0.054	10.536585
R5	0.0238	88.9	12	right	0.004	0.7804878
R5	0.0238	88.9	10	left	0.048	9.3658537
R5	0.0238	88.9	10	right	0.003	0.5853659
					0	0
R10	0.0238	88.9	20	left	0.053	10.341463
R10	0.0238	88.9	20	right	0.058	11.317073
R10	0.0238	88.9	15	left	0.034	6.6341463
R10	0.0238	88.9	15	right	0.055	10.731707
R10	0.0238	88.9	12	left	0.028	5.4634146
R10	0.0238	88.9	12	right	0.052	10.146341
R10	0.0238	88.9	10	left	0.023	4.4878049
R10	0.0238	88.9	10	right	0.048	9.3658537
					0	0
L5	0.0238	88.9	20	left	0.032	6.2439024
L5	0.0238	88.9	20	right	0.065	12.682927
L5	0.0238	88.9	15	left	0.004	0.7804878
L5	0.0238	88.9	15	right	0.062	12.097561
L5	0.0238	88.9	12	left	0.012	2.3414634
L5	0.0238	88.9	12	right	0.06	11.707317
L5	0.0238	88.9	10	left	0.021	4.097561
L5	0.0238	88.9	10	right	0.057	11.121951
					0	0

L10	0.0238	88.9	20	left	0.102	19.902439
L10	0.0238	88.9	20	right	0.001	0.195122
L10	0.0238	88.9	15	left	0.095	18.536585
L10	0.0238	88.9	15	right	0.004	0.7804878
L10	0.0238	88.9	12	left	0.084	16.390244
L10	0.0238	88.9	12	right	0.011	2.1463415
L10	0.0238	88.9	10	left	0.074	14.439024
L10	0.0238	88.9	10	right	0.017	3.3170732

Appendix B

B.1 Tension Equation Derivation

The in-plane tension in a thin membrane is a significant factor in the aeroelastic mechanics. The in-plane tension can be determined by experiments that apply a uniform differential pressure across the membrane and measure the resulting out-of-plane deflection. The tension is then determined from an analysis of membrane mechanics. This appendix is a description of the pertinent membrane mechanics mathematical models. The derivation of the linear model follows closely that given by Den Hartog [12].

The underlying assumptions of membrane mechanics are:

1. The membrane is made of an elastic material.

2. The membrane is sufficiently thin so that the flexural stiffness is negligible.

The membrane is initially flat, and then inflated by air pressure from the bottom. An equation for a thin weightless membrane with an initial tension, T, inflated from the bottom side by an excess air pressure, p, is derived. The air pressure is assumed to be small enough and the initial tension large enough that the inflation strain is negligible when compared with the initial strain, and that consequently T remains constant during the inflation process.

The membrane used for the membrane Equilibrium equation is shown in Figure B1.

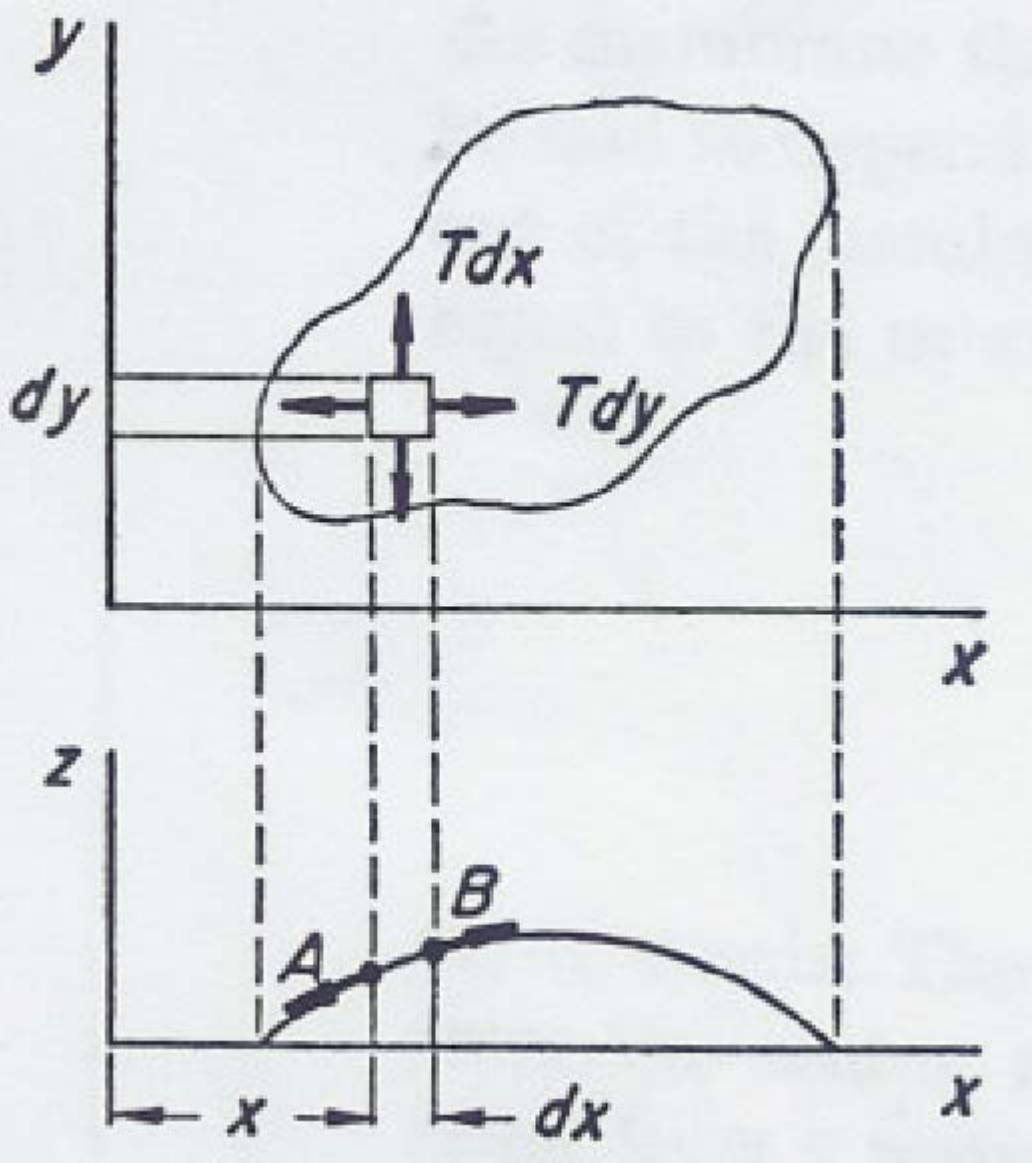

Figure B1: Initially flat membrane under tension T, and air pressure p, from the bottom assumes the shape z with small slopes, satisfying equation 11. [Den Hartog]

The membrane is originally lying flat in the x y plane, with the air pressure p, blowing it up in the z direction. Due to the small pressure, the deflection of the membrane in the z direction, w, will also be small. The equation for the inflated membrane will have the form of z = f(x,y). The slopes of this shape, $\frac{\partial z}{\partial x}$ and $\frac{\partial z}{\partial y}$, will also be relatively small.

For a small element on the membrane, dx dy, there will be two forces acting on it in the x direction (T dy) and two in the y direction (T dx). There will also be the pressure force due to the in-plane membrane tension p, dxdy, which acts perpendicular to the surface in the z-direction. Theses force are then resolved into their components, which are just the forces multiples by the sine, cosine or tangent of the slope. Since the angles are small the following relation ships can be used:

$$\cos\varepsilon = 1 - \tfrac{1}{2}\varepsilon^2 + \ldots \qquad \text{(Equation B1)}$$

$$\sin\varepsilon = \varepsilon - \tfrac{1}{6}\varepsilon^3 + \ldots \qquad \text{(Equation B2)}$$

From these relationships it can be stated that the cosine of the slope equals unity and that the sine (or tangent) of the slope is equal to the slope itself. This holds true for small magnitudes up to the first order, neglecting quantities of the second or higher orders.

The z equilibrium gives rise to a useful equation. The z component of T dy at point A (figure B1) is T dy $\frac{\partial z}{\partial x}$ downward. The z component on at point B would be the same (upward) if the slope $\frac{\partial w}{\partial x}$ were the same, but generally this is not the case. That component can be written as:

$$\mathrm{T}\ dy\ (\frac{\partial w}{\partial x}+\frac{\partial}{\partial x}\ \frac{\partial w}{\partial x}dx\ ) = \mathrm{T}\ \frac{\partial w}{\partial x}dy\ + \mathrm{T}\ \frac{\partial^2 w}{\partial x^2}dxdy \qquad \text{(Equation B3)}$$

The net sum upward of the membrane tensions at A and B together is:

$$\mathrm{T}\ \frac{\partial^2 w}{\partial x^2}dxdy \qquad \text{(Equation B4)}$$

Which is proportional to, $\frac{\partial^2 w}{\partial x^2}$, the curvature for small slopes. The net upward force resulting from the dx and dy faces is:

$$\frac{\partial^2 w}{\partial x^2}+\ \frac{\partial^2 w}{\partial y^2}\ = -\frac{p}{T} \qquad \text{(Equation B5)}$$

This states that the sum of the curvatures in two perpendicular directions is constant for all points of the membrane.

Calculating the shape of a membrane for a given cross section by means of integrating equation B5 can be difficult. For certain geometries, physical intuition can aid in the solution process. Therefore a relationship from the membrane analogy is implemented.

For a circular section, due to symmetry of the height w of the membrane does not depend on two numbers x and y but rather on a single quantity, r, only. Cutting a concentric circle out of the membrane and setting the downward pull on the periphery $2\pi r$ equal to the upward push of the air pressure on $p\pi r^2$ yields:

$$-T\frac{dw}{dr}2\pi r = p\pi r^2 \qquad \text{(Equation B6)}$$

$$-\frac{dw}{dr} = \frac{p}{2T}r \qquad \text{(Equation B7)}$$

This indicates that the slope of the membrane is proportional to the distance r from the center.

The shape of the membrane can be found by integrating:

$$w = -\int \frac{pr}{2T} dr = -\frac{pr}{4T} + const \qquad \text{(Equation B8)}$$

The constant follows the fact that at the periphery r = R the height z must be zero, so that:

$$w = \frac{p}{4T}(R^2 - r^2) \qquad \text{(Equation B9)}$$

B.2 Reynolds Number Calculation

$$\mathrm{Re} = \frac{\rho V D}{\mu}$$

Where D is Characteristic length, V is the velocity, μ is the dynamic viscosity, and ρ is the density. For air at room temperature the flowing properties were used;

D = 50 microns to 115 microns

μ = 1.8205e-5 N.s/m²

ρ = 1.2047 kg/m³

V = 0.2 m/s and 0.1 m/s

For a gap of 50 micron the Reynolds number equation as follows:

$$\mathrm{Re} = \frac{(1.2047\ \mathrm{kg/m^3})(.2\mathrm{m/s})(0.00005\mathrm{m})}{1.8205\text{e-}5\ \mathrm{N.s/m^2}} = 0.6617$$

$$\mathrm{Re} = \frac{(1.2047\ \mathrm{kg/m^3})(.1\mathrm{m/s})(.00005\mathrm{m})}{1.8205\text{e-}5\ \mathrm{N.s/m^2}} = 0.3308$$

This yields a Reynolds number range from 0.3308 to 0.6617 for a gap of 50 microns

For the larger gap of 115 micron we get the following:

$$\mathrm{Re} = \frac{(1.2047\ \mathrm{kg/m^3})(.2\mathrm{m/s})(0.000115\mathrm{m})}{1.8205\text{e-}5\ \mathrm{N.s/m^2}} = 1.522$$

$$\mathrm{Re} = \frac{(1.2047\ \mathrm{kg/m^3})(.1\mathrm{m/s})(.000115\mathrm{m})}{1.8205\text{e-}5\ \mathrm{N.s/m^2}} = 0.761$$

This yields a Reynolds number range from 0.761 to 1.522 for a gap of 115 microns

For helium at room temperature the following properties were used;

D = 50 microns to 115 microns

μ = 1.860e-5 N.s/m²

ρ = 0.1785 kg/m³

V = 0.2 m/s and 0.1 m/s

For a gap of 50 micron the Reynolds number equation is as follows:

$$\mathrm{Re} = \frac{(0.1785\ \mathrm{kg/m^3})(.2\mathrm{m/s})(0.00005\mathrm{m})}{1.860\text{e-}5\ \mathrm{N.s/m^2}} = 0.09596$$

$$\mathrm{Re} = \frac{(0.1785\ \mathrm{kg/m^3})(.1\mathrm{m/s})(0.00005\mathrm{m})}{1.860\text{e-}5\ \mathrm{N.s/m^2}} = 0.04798$$

This yields a Reynolds number range from 0.04798 to 0.09596 for a gap of 50 microns

For the larger gap of 115 micron we get the following:

$$\mathrm{Re} = \frac{(0.1785\ \mathrm{kg/m^3})(.2\mathrm{m/s})(0.000115\mathrm{m})}{1.860\text{e-}5\ \mathrm{N.s/m^2}} = 0.2207$$

$$\mathrm{Re} = \frac{(0.1785\ \mathrm{kg/m^3})(.1\mathrm{m/s})(0.000115\mathrm{m})}{1.860\text{e-}5\ \mathrm{N.s/m^2}} = 0.1104$$

This yields a Reynolds number range from 0.1104 to 0.2207 for a gap of 115 microns

B.3 Knudsen Number Calculation

$$K_n = \frac{\lambda}{\mathrm{L}}$$

Where λ is the mean free path of air, and L is the characteristic dimension.

Air at 1 atm 298K

Maxwell calculated the mean free path of air with the help of the coefficient of viscosity estimated by Stokes. The value was 0.000062 mm.

Therefore

λ = 0.062 microns

L = 50 microns – 115microns

$$K_n = \frac{(0.062 \text{ microns})}{50 \text{ microns}}$$

Making Knudsen number for air = range from **0.00124 to 0.000539** for gaps ranging from 50 to 115 microns.

For a small gap of 5 microns, Knudsen number becomes **0.0124**

Helium at 1 atm, 298K

Helium has an atomic diameter (σ) of $3.74*10^{-10}\,m$

$$R = .0000821\frac{m^3 * atm}{\text{K*mol}}$$

$$T = 298K$$

$$P = 1\,atm$$

$$N_0 = 6.023*10^{23}\,\frac{molecules}{mol}$$

$$\sigma = 3.74*10^{-10}\,m$$

Applying the ideal gas law:

$$PV = NRT$$

Therefore:

$$\frac{N}{V} = \frac{PN_0}{RT} = \frac{1\,atm*(6.023*10^{23})\frac{molecules}{mol}}{0.0000821\frac{m^3 * atm}{K * mol}*298K} = 2.46*10^{25}\,\frac{molecules}{mol}$$

$$\lambda = \frac{1}{\sqrt{2}*\pi*(\frac{N}{V})*\sigma^2} = \frac{1}{\sqrt{2}\pi*(2.46*10^{25}\,\frac{molecules}{mol})*(3.74*10^{-10}\,m)^2}$$

$$\lambda = 6.54*10^{-8}\,m\ = 0.0654 \text{ microns}$$

$$K_n = \frac{(0.0654 \text{ microns})}{50 \text{ microns}} = 0.001308$$

Making the Knudsen number for helium at 760 torr (1 atm) range from **0.00138 to 0.000568** for gaps ranging from 50 to 115 microns.

For a small gap of 5 microns, Knudsen number becomes **0.01308**

Helium at a vacuum of 700 torr (0.9211 atm)

$$\frac{N}{V}=\frac{PN_0}{RT}=\frac{0.9211\,atm*(6.023*10^{23})\frac{molecules}{mol}}{0.0000821\frac{m^3*atm}{K*mol}*298K}=2.26*10^{25}\,\frac{molecules}{mol}$$

$$\lambda=\frac{1}{\sqrt{2}*\pi*(\frac{N}{V})*\sigma^2}=\frac{1}{\sqrt{2}\pi*(2.26*10^{25}\,\frac{molecules}{mol})*(3.74*10^{-10}m)^2}$$

$\lambda=6.53*10^{-8}m$ = 0.0653 microns

$$K_n=\frac{(0.0653\text{ microns})}{50\text{ microns}}=0.001306$$

Making the Knudsen number for helium at 700 torr (0.9211 atm) range from **0.00136 to 0.000567** for gaps ranging from 50 to 115 microns.

For a small gap of 5 microns, the Knudsen number becomes **0.01306**

B.4 MathCAD Calculations

Constants

$\mathbf{U} := .02$

$\eta := 1.8 \cdot 10^{-5}$

$\mathbf{x1} := 0$

$\mathbf{x2} := .009999$

$\mathbf{x3} := .004999$

$\mathbf{h0} := .000152$

$\mathbf{h1} := .000229$

$\mathbf{T} := 4.5$

.

(Where b is the wedge angle in radians)

$\mathbf{b} := 0.0077$

Given

(Reynolds equation in 1-D expanded out using the product rule)

$$3 \cdot (\mathbf{h0} + \mathbf{b} \cdot \mathbf{x})^2 \cdot \frac{\mathbf{d}}{\mathbf{dx}} \mathbf{P}(\mathbf{x}) \cdot \mathbf{b} + (\mathbf{h0} + \mathbf{b} \cdot \mathbf{x})^3 \cdot \frac{\mathbf{d}^2}{\mathbf{dx}^2} \mathbf{P}(\mathbf{x}) = 6 \cdot \mathbf{U} \cdot \eta \cdot \mathbf{b}$$

$\mathbf{P}(0) = 0$

$\mathbf{P}(\mathbf{x2}) = 0$

$\mathbf{P} := \mathbf{Odesolve}(\mathbf{x}, 100)$

(Height of deflected membrane from granite block surface)

$\mathbf{he} := \mathbf{h0} + \mathbf{b} \cdot \mathbf{x3}$

$\mathbf{he} = 1.905 \times 10^{-4}$

$\mathbf{P}(\mathbf{x3}) = 0.328$

Given

(Membrane mechanics equation)

$$\left(\frac{\mathbf{d}^2}{\mathbf{dx}^2} \mathbf{w}(\mathbf{x}) \right) = \frac{-\mathbf{P}(\mathbf{x})}{\mathbf{T}}$$

$\mathbf{w}(\mathbf{x1}) = (0)$

$\mathbf{w}(\mathbf{x2}) = (0)$

(Boundary conditions)

$\mathbf{w} := \mathbf{Odesolve}(\mathbf{x}, 100)$

$\mathbf{w}(\mathbf{x3}) = 1.838 \times 10^{-6}$

$\mathbf{he2} := (\mathbf{h0} + \mathbf{b} \cdot \mathbf{x3}) + \mathbf{w}(\mathbf{x3})$

$\mathbf{he2} = 1.923 \times 10^{-4}$

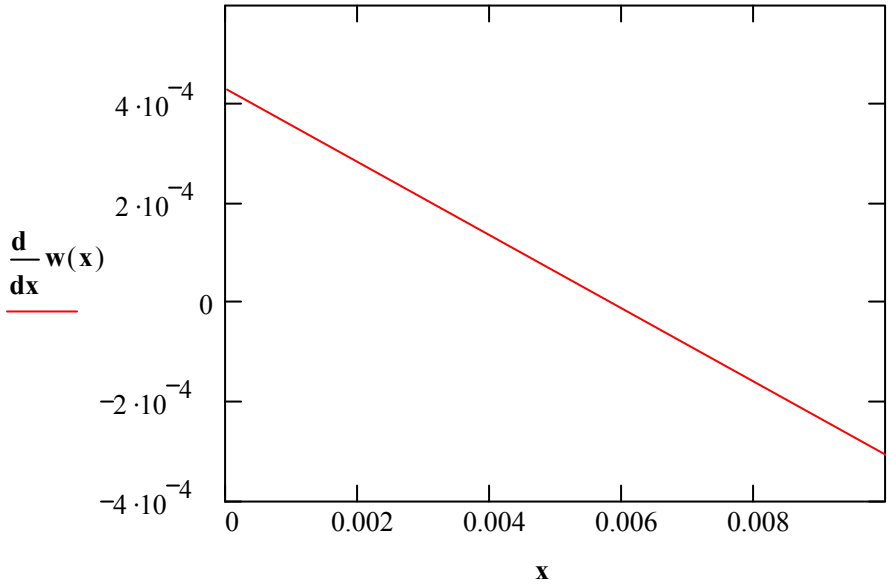

Figure B1

(The mean value was obtained from the graph for the derivative of w(x) and plugged back into the Reynolds equation) (Shown in the eq. below as 0.0008)

Given

$$3 \cdot (\mathbf{h0} + \mathbf{b} \cdot \mathbf{x} + \mathbf{w}(\mathbf{x}))^2 \cdot \frac{d}{dx}\mathbf{P2}(\mathbf{x}) \cdot (\mathbf{b} + .0018) + (\mathbf{h0} + \mathbf{b} \cdot \mathbf{x} + \mathbf{w}(\mathbf{x}))^3 \cdot \frac{d^2}{dx^2}\mathbf{P2}(\mathbf{x}) = 6 \cdot \mathbf{U} \cdot \eta \cdot \mathbf{b}$$

$\mathbf{P2}(0) = 0$

$\mathbf{P2}(\mathbf{x2}) = 0$

(Boundary conditions)

$\mathbf{P2} := \mathbf{Odesolve}(\mathbf{x}, 100)$

$\mathbf{P2}(\mathbf{x3}) = 0.446$

Given

$$\left(\frac{d^2}{dx^2}\mathbf{w2}(\mathbf{x})\right) = \frac{-\mathbf{P2}(\mathbf{x})}{\mathbf{T}}$$

$\mathbf{w2}(\mathbf{x1}) = (0)$

$\mathbf{w2}(\mathbf{x2}) = (0)$

(Boundary conditions)

$\mathbf{w2} := \mathbf{Odesolve}(\mathbf{x}, 100)$

$\mathbf{w2}(\mathbf{x3}) = 8.704 \times 10^{-6}$

$\mathbf{he3} := (\mathbf{h0} + \mathbf{b} \cdot \mathbf{x3}) + \mathbf{w2}(\mathbf{x3})$

$\mathbf{he3} = 1.992 \times 10^{-4}$

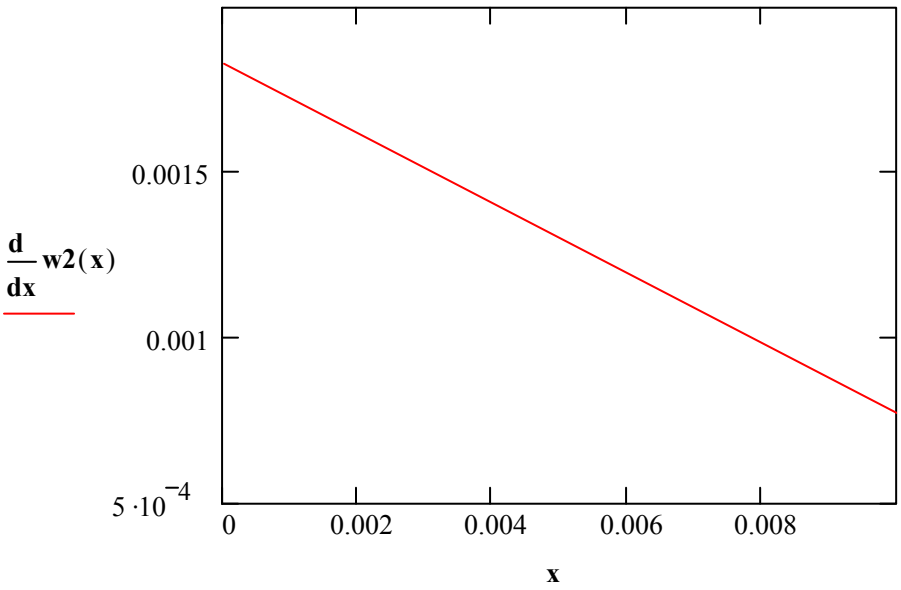

Figure B2

Given

$$3 \cdot (\mathbf{h0} + \mathbf{b} \cdot \mathbf{x} + \mathbf{w2}(\mathbf{x}))^2 \cdot \frac{d}{dx} \mathbf{P3}(\mathbf{x}) \cdot (\mathbf{b} - .0018) + (\mathbf{h0} + \mathbf{b} \cdot \mathbf{x} + \mathbf{w2}(\mathbf{x}))^3 \cdot \frac{d^2}{dx^2} \mathbf{P3}(\mathbf{x}) = 6 \cdot \mathbf{U} \cdot \boldsymbol{\eta} \cdot \mathbf{b}$$

$\mathbf{P3}(0) = 0$

$\mathbf{P3}(\mathbf{x2}) = 0$

(Boundary conditions)

$\mathbf{P3} := \mathbf{Odesolve}(\mathbf{x}, 100)$

$\mathbf{P3}(\mathbf{x3}) = 0.637$

Given

$$\left(\frac{d^2}{dx^2} \mathbf{w3}(\mathbf{x}) \right) = \frac{-\mathbf{P3}(\mathbf{x})}{\mathbf{T}}$$

$\mathbf{w3(x1)} = (0)$

$\mathbf{w3(x2)} = (0)$

(Boundary conditions)

$\mathbf{w3} := \mathbf{Odesolve}(\mathbf{x}, 100)$

$\mathbf{w3(x3)} = 2.018 \times 10^{-5}$

$\mathbf{he4} := (\mathbf{h0} + \mathbf{b} \cdot \mathbf{x3}) + \mathbf{w3(x3)}$

$\mathbf{he4} = 2.107 \times 10^{-4}$

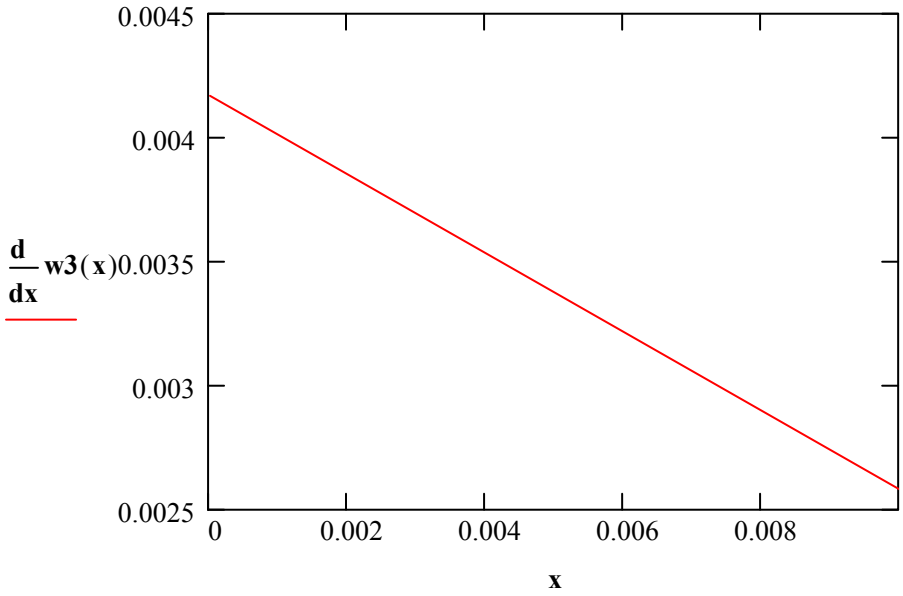

Figure B3

Given

$$3 \cdot (\mathbf{h0} + \mathbf{b} \cdot \mathbf{x} + \mathbf{w3(x)})^2 \cdot \frac{\mathbf{d}}{\mathbf{dx}} \mathbf{P4(x)} \cdot (\mathbf{b} - 0) + (\mathbf{h0} + \mathbf{b} \cdot \mathbf{x} + \mathbf{w3(x)})^3 \cdot \frac{\mathbf{d}^2}{\mathbf{dx}^2} \mathbf{P4(x)} = 6 \cdot \mathbf{U} \cdot \boldsymbol{\eta} \cdot \mathbf{b}$$

$\mathbf{P4}(0) = 0$

$\mathbf{P4(x2)} = 0$

(Boundary conditions)

$\mathbf{P4} := \mathbf{Odesolve}(\mathbf{x}, 100)$

$\mathbf{P4(x3)} = 3.888$

Given

$$\left(\frac{\mathbf{d}^2}{\mathbf{dx}^2} \mathbf{w4(x)} \right) = \frac{-\mathbf{P3(x)}}{\mathbf{T}}$$

$\mathbf{w4}(\mathbf{x1}) = (0)$

$\mathbf{w4}(\mathbf{x2}) = (0)$

(Boundary conditions)

$\mathbf{w4} := \mathbf{Odesolve}(\mathbf{x}, 100)$

$\mathbf{w4}(\mathbf{x3}) = 2.018 \times 10^{-5}$

$\mathbf{he5} := (\mathbf{h0} + \mathbf{b} \cdot \mathbf{x3}) + \mathbf{w4}(\mathbf{x3})$

$\mathbf{w4}(\mathbf{x1}) = 0$

$\mathbf{he5} = 2.107 \times 10^{-4}$

$\mathbf{w4}(.001) = 4.164 \times 10^{-6}$

$\mathbf{w4}(.002) = 8.296 \times 10^{-6}$

$\mathbf{w4}(.003) = 1.236 \times 10^{-5}$

$\mathbf{w4}(.004) = 1.634 \times 10^{-5}$

$\mathbf{w4}(.005) = 2.018 \times 10^{-5}$

$\mathbf{w4}(.00995) = 3.626 \times 10^{-5}$

$\mathbf{w4}(.006) = 2.387 \times 10^{-5}$

$\mathbf{w4}(.00996) = 3.629 \times 10^{-5}$

$\mathbf{w4}(.007) = 2.737 \times 10^{-5}$

$\mathbf{w4}(.009961992) = 3.629 \times 10^{-5}$

$\mathbf{w4}(.008) = 3.064 \times 10^{-5}$

$\mathbf{w4}(.009) = 3.366 \times 10^{-5}$

$\mathbf{w4}(.0099) = 3.613 \times 10^{-5}$

References

1. Boresi, K. Chong, Elasticity in Engineering Mechanics, Elsevier, New York, N.Y., 1987, pg. 364.

2. Cameron, A., Basic Lubrication Theory. Ellis Horwood limited, Coll House, Westergate, Chichester, England. 1976.

3. Cerrina, F., Handbook of Microlithography, Micromachining, and Microfabrication. Chapter 3 X-Ray Lithography. Edited by P. Rai-Choudhury January 1997.

4. Clark, R., Cox, D., Curtiss, H.C.J., Edwards, J.W., Hall, K.C., Peters, D.A., Scanlan, R.H., Simiu, E., Sisto, F., Strganac, T.W., Dowell, E.H. (Ed.). A Modern Course in Aeroelasticity. 4th rev. and enlarged ed., 2004, XXVII.

5. Elliot, D., Microlithography: Process Technology for IC Fabrication, McGraw-Hill, New York N.Y., 1986.

6. Farhat, C., Lesoinne, M., Chen, P., Nonlinear Transient Aeroelastic Simulations Department of Aerospace Engineering Sciences, University of Colorado, Boulder CO

7. Pan, J. Kubby, E. Peeters, A.T. Tran and S. Mukherjee Affilation: *XEROX,* Squeeze Film Damping Effect on the Dynamic response of a MEMS Torsion Mirror *Xerox Wilson Research Center, U.S.A.*Pages:474 - 479

8. Fung, Y.C., An Introduction to the Theory of Aeroelasticity. Dover Publications May 2002.

9. Gill, J., Application of Bulge Testing Techniques in Determining the Mechanical Properties of Thin Films. MS Thesis, University of Vermont, 1998.

10. Hamilton, D., Y-Stage Design for X-ray Lithography, Master's Thesis, University of Vermont, 1999, pg. 41.

11. Holzl, S., Development and Construction of a Device to Measure Aeroelastic Distortions in Thin Films for Proximity (X-ray) Lithography. Semester Thesis, University of Vermont, 2004

12. Hartog, D., Advanced Strength of Materials. New York: McGraw-Hill, c1952, pg 10-15.

13. Huston, D., Mask Mechanics – Aeroelastic and Adaptive Shape Control, University of Vermont, Burlington VT

14. Huston, D., Sauter, W., Mask Stretching for Next Generation Lithography Masks IEEE Transactions on Semiconductor Manufacturing, Vol. 14, No. 3, August 2001.

15. Huston, D., Mask Aeroelasticity Summary Report. Submitted to JMAR Systems a division of JMAR inc., December 2005.

16. Huston, D., Plumpton, J. O., Esser, B., Hoelzl, S., Wang, X., Sullivan, G., Membrane mask aeroelastic and thermoelastic control. SPIE proceedings Vol. 5374, May 2004, pg. 780.

17. Juang, Jer-Nan, Denis Kholodar, Earl H. Dowell, System identification of a vortex lattice aerodynamic model [microform]. Hampton, Va.: National Aeronautics and Space Administration, Langley Research Center; Hanover, MD: Available from NASA Center for AeroSpace Information (CASI), 2001.

18. Laudon, M., Laird, D., Engelstad, R., Cerrina, F., Mechanical Response of X-Ray Masks. Japan Journal of Applied Physics, Vol. 32, pg. 5928-5932, 1993.

19. Levinson, Harry J., Principles of lithography. Bellingham, Wash., USA: SPIE Press, c2001.

20. Mizusawa, N., Uda, K., Ohta, H., Watanabe, Y., Technology and performance of the Canon XRA-1000 production x-ray stepper. Journal of Vacuum Science Technology B, vol. 18(6), Nov/Dec 2000, pg 2955-2960.

21. Mizusawa, N., Uda, K., Ohta, H., Watanabe, Y., Pieczulewski, C., X-Ray Lithography a Reality for 100nm Production and Beyond. Future Fab. International, Vol. 5 1997.

22. Peckerar, M., Maldonaldo, J., X-Ray Lithography-An Overview. Proceedings of the IEEE, Volume 81, No. 9, September 1993.

23. Plumpton, J.O., Active Membrane Masks for Improved Overlay Performance in Proximity Lithography, Masters Thesis, University of Vermont, 2004

24. Raymond L. Bisplinghoff, Holt Ashley [and] Robert L. Halfman, Aeroelasticity. Cambridge, Mass., Addison-Wesley Pub. Co. 1955.

25. Sauter, W., Thin Film Mechanics: Bulging and Stretching, PhD Thesis, University of Vermont, 2001.

26. Slocum, Alexander H., Precision machine design. Dearborn, Michigan: Society of Manufacturing Engineers, c1992.

27. Timoshenko, S., Theory of Elasticity, McGraw-Hill, New York, N.Y., 1951

28. Ugural, A.C., Stresses in plates and shells. New York: McGraw-Hill, c1981. xv, 317 p. : ill. ; 24 cm.

29. Wan, K., Liu, K., Engineering "Mechanics of Adhesion of Bio-capsule and Bio-Membrane to a Planar Substrate. Mechanical & Aerospace Engineering & Engineering Mechanics, University of Missouri- Rolla, MO, Tissue Engineering Laboratory, Nanyang Technological University, Singapore

30. Wells, G.M., Reilly, M., Moore, F., Cerrina, F., X-ray Mask Fabrication Process. SPIE proceedings, Volume 2512, pg 167-171, 1995.

31. http://www.ece.umd.edu/~nima/ebeam.pdf May 2005

32. http://www.jmar.com/2004/prod_cpltech.shtml May 2005